DEVELOPMENT OF SMALL SIZE
UNCOOLED INFRARED MICROBOLOMETER PIXEL

A THESIS SUBMITTED TO
THE GRADUATE SCHOOL OF NATURAL AND APPLIED SCIENCES
OF
MIDDLE EAST TECHNICAL UNIVERSITY

BY

BARAN UTKU TEKİN

IN PARTIAL FULFILLMENT OF THE REQUIREMENTS
FOR
THE DEGREE OF MASTER OF SCIENCE
IN
MICRO AND NANOTECHNOLOGY

SEPTEMBER 2021

Approval of the thesis:

**DEVELOPMENT OF SMALL SIZE
UNCOOLED INFRARED MICROBOLOMETER PIXEL**

submitted by **BARAN UTKU TEKİN** in partial fulfillment of the requirements for the degree of **Master of Science** in **Micro and Nanotechnology, Middle East Technical University** by,

Prof. Dr. Halil Kalıpçılar
Dean, Graduate School of **Natural and Applied Sciences**   _____

Prof. Dr. Almıla Güvenç Yazıcıoğlu
Head of the Department, **Micro and Nanotechnology, METU** _____

Prof. Dr. Tayfun Akın
Supervisor, **Electrical and Electronics Engineering, METU** _____

Prof. Dr. Raşit Turan
Co-Supervisor, **Physics, METU**   _____

Examining Committee Members:

Prof. Dr. Haluk Külah
Electrical and Electronics Engineering, METU   _____

Prof. Dr. Tayfun Akın
Electrical and Electronics Engineering, METU   _____

Prof. Dr. Hakan Altan
Physics, METU   _____

Assoc. Prof. Dr. Kıvanç Azgın
Mechanical Engineering, METU   _____

Assoc. Prof. Dr. Mahmud Yusuf Tanrıkulu
Electrical-Electronics Engineering, Adana Alparslan Türkeş
Science and Technology University   _____

Date: 09.09.2021

I hereby declare that all information in this document has been obtained and presented in accordance with academic rules and ethical conduct. I also declare that, as required by these rules and conduct, I have fully cited and referenced all material and results that are not original to this work.

Name, Last name : Baran Utku Tekin

Signature :

ABSTRACT

DEVELOPMENT OF SMALL SIZE
UNCOOLED INFRARED MICROBOLOMETER PIXEL

Tekin, Baran Utku
Master of Science, Micro and Nanotechnology
Supervisor: Prof. Dr. Tayfun Akın
Co-Supervisor: Prof. Dr. Raşit Turan

September 2021, 106 pages

This thesis reports the development of 12 µm pixel pitch single layer microbolometer structures for use in the 8-12 µm wavelength regions, following recent trends in the last decade in microbolometers. Various pixel structures are designed, simulated, fabricated, and characterized to obtain acceptable detector performance in these small pixels. The pixel structures are improved by reducing the pixel thermal conductance and by using planar type electrode structures where the active material is selected as VWO_x (Vanadium-Tungsten Oxide). Predictive modeling with electro-thermal simulations has aided in attaining the best possible pixel structures. Besides that, absorptance is optimized using the cascaded transmission line (CTL) simulation method to improve the pixel absorption between 8-12 µm spectral region show that more than 85% level.

Designed detector pixels are fabricated using a CMOS compatible process flow. Each fabrication step is optimized considering a possible array fabrication on CMOS wafers. Then, pixels are characterized electrically, thermally, and optically. These

characterizations include temperature coefficient of resistance (TCR), noise, thermal conductance, absorption, responsivity, and thermal time constant measurements. The TCR of the active material, VWO_x, is measured around -4 %/K with an optimum resistance value. The thermal conductance values of pixels are measured as low as 20 nW/K. Additionally, the corner frequency is measured 0.85 kHz at 10 µA bias current. Finally, a responsivity value of 37 kV/W at 473 µV is measured for the best-performed fabricated pixel with a low thermal time constant of less than 2 ms, suitable for applications that require high frame rates.

Fabrication of 640x480 format FPAs is conducted in the framework of this thesis with the optimized detector structure. Among measured FPAs, the responsivity and operability are measured as high as 10 mV/K and >99%, respectively. Using these measurement results, the lowest NETD value of a 640x480 FPA measured minimum is 200 mK. The success of the developed detector structures is verified through the images obtained from the detectors that are monolithically built on the CMOS readout circuit. It should be noted that this thesis reports the first successfully fabricated 640x480 FPA array using a 12 µm pixel pitch single layer microbolometer in Turkey. The development in this small size FPA production may open a path to different applications to be developed and used in Turkey in the future.

Keywords: Uncooled Infrared Detectors, Microbolometer Pixels, Surface Micromachining, Micro-Electro-Mechanical Systems (MEMS), Thermal Performance, Thermal Conductance, and Isolation, post-CMOS Processing, Thermal-Electrical-Optical-Mechanical Simulations

ÖZ

MİNYATÜR SOĞUTMASIZ KIZILÖTESİ MİKROBOLOMETRE PİKSELİ GELİŞTİRİLMESİ

Tekin, Baran Utku
Yüksek Lisans, Mikro ve Nanoteknoloji
Tez Yöneticisi: Prof. Dr. Tayfun Akın
Ortak Tez Yöneticisi: Prof. Dr. Raşit Turan

Eylül 2021, 106 sayfa

Bu tez raporunda, son on yılda mikrobolometre camiasındaki trendleri takip ederek, 8-12 µm dalga boyu bölgesinde kullanım için 12 µm piksel genişliğine sahip tek katmanlı mikrobolometre yapılarının gelişimi gösterilmiştir. Bu küçük piksellerde kabul edilebilir dedektör performansı elde etmek için çeşitli piksel yapıları tasarlanmış, simülasyonu yapılmış, üretilmiş ve bu piksellerin karakterizasyonu yapılmıştır. Bu piksel yapıları, piksel termal iletkenliği azaltılarak ve aktif malzemenin VWO_x (Vanadyum-Tungsten Oksit) olarak seçildiği düzlemsel tip elektrot yapıları kullanılarak iyileştirilmiştir. Elektriksel ve termal simülasyonlarla tahmine dayalı modelleme, mümkün olan en iyi piksel yapılarının elde edilmesine yardımcı olmuştur. Bunun yanı sıra, 8-12 µm spektral bölge arasındaki piksel absorpsiyonunu iyileştirmek için kademeli iletim hattı (CTL) simülasyon yöntemi kullanılarak emilim yüzdesinin optimize edilmesi sağlanmış ve bu optimizasyonlar ile emilim yüzdesinin % 85'in üzerinde bir seviyede olduğu gösterilmiştir.

Tasarlanan dedektör pikselleri, CMOS üretim uyumluluğu göz önünde bulundurularak üretilmiştir. Her üretim adımı, CMOS pul yapısı ile olası bir dizi üretimi göz önünde bulundurularak optimize edilmiştir. Daha sonra pikseller elektriksel, termal ve optik olarak karakterize edilmiş ve bu karakterizasyonlar, sıcaklık direnci katsayısı (TCR), gürültü, termal iletkenlik, absorpsiyon, tepki ve termal zaman sabiti ölçümlerini içerir. VWO_x aktif malzemesinin TCR'i, optimum direnç değeri üzerinden -4 %/K civarlarında ve piksellerin termal iletkenlik değerleri en düşük 20 nW/K değerine kadar ölçülmüştür. Ek olarak, gürültüsü köşe frekansı, 10 µA akımında 0.85 kHz ölçülmüştür. Çeşitli piksel yapılarından en iyi performans sergileyen pixel yapısı için 473 µV gerilimi altında piksel tepkiselliği ~37 kV/W ölçülmüş ve yine bu tarımın 2 ms'den fazla olmayan zaman sabiti yüksek hareket içeren görüntülerde iyi bir performans sağlayacaktır.

Bu tez kapsamında optimizasyonu yapılmış dedektör yapısı ile 640x480 formatındaki FPA'ların üretimi gerçekleştirilmiştir. Ölçülen FPA'lar arasında, tepkiselliği ve çalışabilirliği sırasıyla 10 mV/K'e kadar yüksek ve >%99 olarak ölçülmüştür. Bu ölçüm sonuçlarını kullanarak, 640x480 FPA'nın en düşük NETD değeri 200 mK olarak ölçülmüş. Geliştirilen dedektör yapılarının başarısı, CMOS okuma devresi üzerine dedektörlerden elde edilen görüntülerle doğrulanmaktadır. Bu tezin, Türkiye'de 12 µm piksel aralıklı tek katmanlı mikrobolometre yapısı kullanılarak başarıyla üretilmiş ve görüntü alınmış ilk 640x480 FPA dizisini rapor ettiği belirtilmelidir. Bu küçük boyutlu FPA üretimindeki gelişme, gelecekte Türkiye'de geliştirilecek ve kullanılacak farklı uygulamaların yolunu açabilir.

Anahtar Kelimeler: Soğutmasız Kızılötesi Dedektörleri, Mikrobolometreler, Yüzey Mikro İşleme, Mikro-Elektro-Mekanik Sistemler (MEMS), Isıl Performans, Isıl İletkenlik ve Yalıtkanlık, CMOS sonrası üretim, Termal-Elektriksel-Optik-Mekanik Simulasyon

To my Family,

To ALL the people livin' life in PEACE,

ACKNOWLEDGMENTS

TABLE OF CONTENTS

LIST OF TABLES

LIST OF FIGURES

xviii

CHAPTER 1

INTRODUCTION

Infrared (IR) radiation is a form of electromagnetic radiation covering the frequency range between microwave and visible light in the electromagnetic spectrum. A device that senses IR radiation is called an IR detector. These detectors have been widely used in many areas like in medical applications, surveillance, military use, and rapid growth in many commercial applications. Because the human eye has limited capability, which only sees a visible portion of the whole electromagnetic spectrum, the IR detectors are more critical in these application areas. However, in these widely used areas of IR detectors, the systems requirements also increase day-by-day. So, developing infrared-sensitive detectors with good specs becomes important.

Converting absorbed radiation into an electrical signal, which can be explained by using different phenomena, is the primary function of the detectors. The IR detector parts can be divided into photon detectors and thermal detectors that can be seen in **Table 1.1**. In photon detectors, incoming radiation is absorbed into the specified materials by interacting with electrons. These interactions can be either bounded with free electrons in the material or bounded to impurity inside the materials. So, when the material absorbs an incoming photon, it causes quantum transitions between different energy states, resulting in an electrical signal [1], and produces parameter changes (like current, voltage, etc.) manipulated by external circuits. This photon detector depends on the absorbed photons, and they have some advantages like a fast response, good signal-to-noise ratio, and wavelength-dependent, which are mainly used in military, astronomical, and spectroscopic applications [2]–[5]. On the other hand, thermal detectors measure temperature changes caused by changes in the material's properties when illuminated by IR radiation. These detectors are better in

many ways. They are compact, provide less power consumption, and do not need to be operated at high temperatures. Furthermore, these systems are cheaper imaging systems with a wider variety of military, industrial inspection, and civilian consumer applications like automotive, chemical industry, and environmental studies [6], [7]. They are promising because they have these beneficial qualities. So, during the last several years, the need for uncooled IR detectors has grown substantially [8]. Thus, the primary goal of thermal infrared imaging research is to develop smaller detector pixels while retaining high sensitivity. This thesis aims to present the creation of a single-layer microbolometer pixel with a 12 µm pixel pitch. The structures and models for 12 µm pixel pitch utilized in this study are appropriate for smaller, multilayer microbolometers and are compatible with post-CMOS manufacturing, enabling FPA applications.

Table 1.1: IR detector types with commonly used materials [9].

Thermal Detectors		Photon Detectors	
Bolometers	Vanadium Oxide a-Si SiGe	Intrinsic, PV	MCT Si, Ge InGaAs, InSb
Pyroelectric	LiTa PbZT	Intrinsic, PC	MCT PbS, PbSe
Thermopiles	Bi/Sb	Photo-emissive	PtSi
Micro Cantilever	Bimetals	QWIP	GaAs/AlGaAs

1.1   Infrared Radiation

Infrared (IR) radiation is electromagnetic radiation that the wavelength ranges classified between visible radiation (λ=380-780 nm) and microwave radiation

(λ=1 mm-1 m) which is separated into sub-portion of VIS, SWIR, MWIR, and LWIR. **Figure 1.1** visualizes the electromagnetic spectrum with subregions [10].
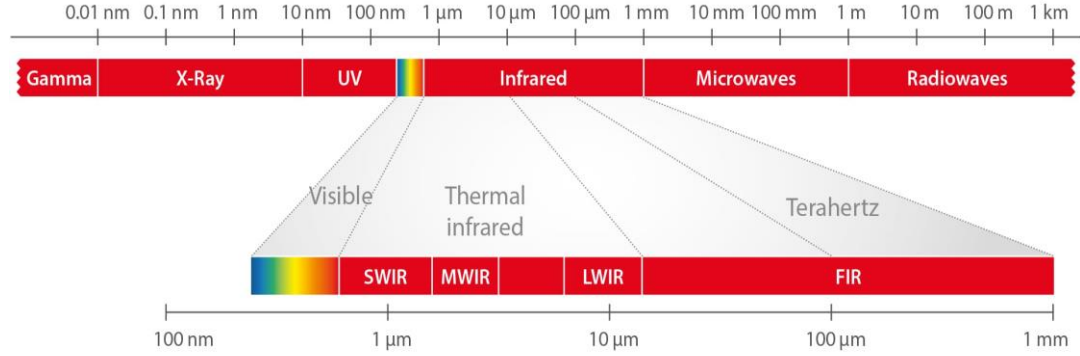
Figure 1.1: Electromagnetic spectrum with sub-regions [10].

The absorptance of a material is proportional to the incoming radiation, whereas its emissivity is proportional to the radiation emitted by a blackbody. These two factors are inextricably linked since equilibrium exists for an item at a constant temperature. A blackbody is an ideal reference body with uniform absorptance and emissivity. It describes the spectral radiance of the electromagnetic radiation emitted by a perfect blackbody as a function of its temperature (T) and the wavelength (λ) of the emitted radiation that can be seen in **Figure 1.2**. According to Planck's radiation law, everything with a surface temperature greater than 0 K emits infrared radiation. It can be described as,

$$M(\lambda, T) = \frac{2\pi h c_0^2}{\lambda^5} \left[\exp\left(\frac{hc_0}{\lambda k_B T}\right) - 1 \right]^{-1} \qquad (1.1)$$

where h is the Planck's constant, c_0 is the velocity of light in vacuum, k_B is Boltzmann's constant. The temperature of the item determines the strength and spectrum richness of the emitted radiation. As the temperature of the item increases, the peak of the radiated radiation changes to shorter wavelengths.
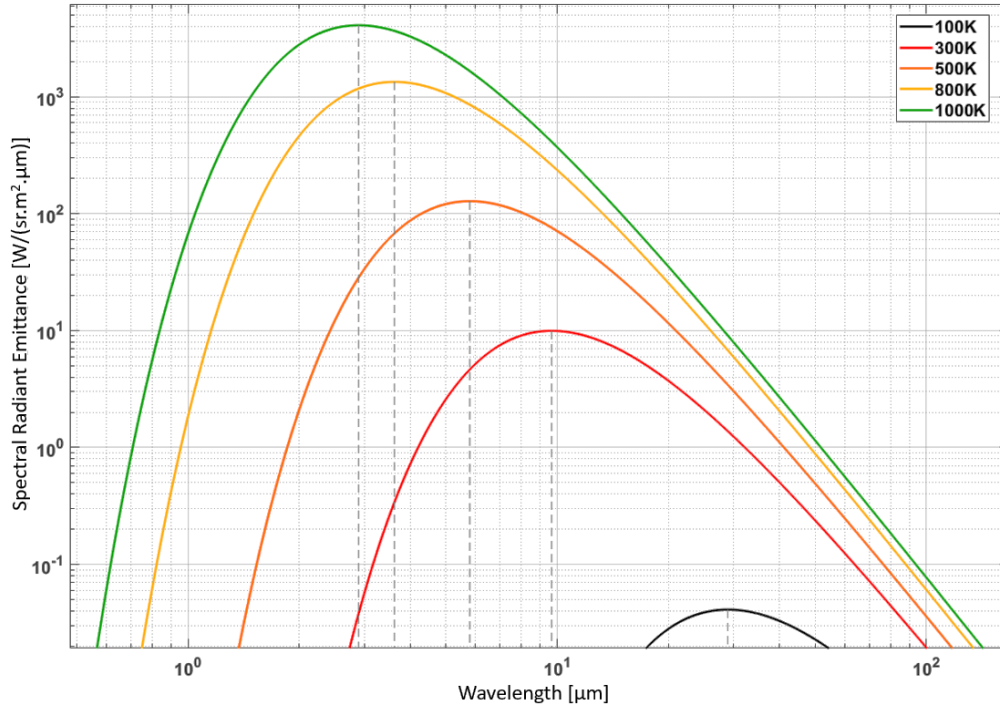
Figure 1.2: Spectral radiance of a typical blackbody for various temperature values.

The maximum exitance of an object at a given temperature can be found [11] by determining the position of the corresponding peak with

$$\lambda_{max}T = 2.8975 * 10^{-3} \text{ (m.K)} \tag{1.2}$$

In addition to infrared radiation-emitting, the atmosphere is not transparent for all infrared wavelengths emitted by distant objects must usually travel a certain distance through the air before being detected by infrared detectors. As seen in **Figure 1.3**, due to the dispersion and absorption of air molecules (H_2O, CO_2), the energy that can be measured diminishes with increasing distances. As seen in the figure, the atmospheric window is only effective for infrared radiation between 3-5 µm and 8-14 µm.
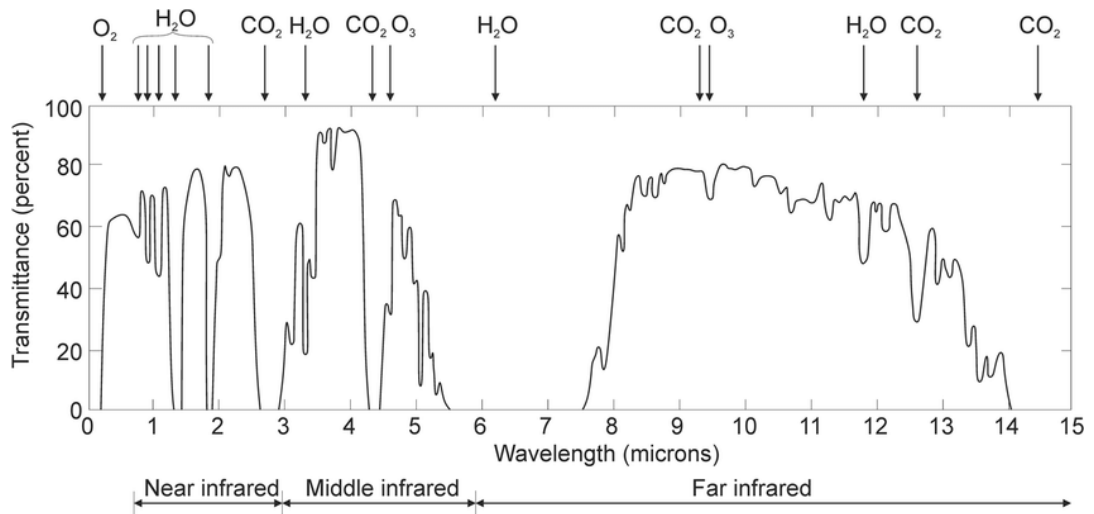
Figure 1.3: Transmission window of the earth's atmosphere [12].

With all this information, in order to detect an object at room temperature around 300 K, where located in a spectral band at 10 µm, 8-14 µm transfer window can be the best choice. If the object's temperature increases, it is difficult to detect in this range because of the IR radiation in the atmosphere.

1.2   Thermal Infrared Detectors

Thermal detectors are based on an element's absorption of electromagnetic radiation, which results in a change in its temperature. Thermal detectors have properties that are affected by changes in temperature. These properties are assessed electrically and serve as a measure of the amount of energy taken in by the detector. A thermal detector is composed of a thermally insulated absorber to produce a significant temperature change in response to incoming radiation [13]. Several ways to detect this temperature difference physically exist. The followings are a quick overview of the most common kinds of detecting devices as thermal infrared detectors.

1.2.1   Thermopile (Thermo-Electric) Detectors

The thermocouples were discovered in 1821 by German physicist Thomas J. Seebeck [14]. Suppose two materials, like two semiconductors or two metals, are connected at the hot point as a junction. In that case, the temperature differences, ΔT, occur between the hot junction and the cold point. This phenomenon representation can be seen in **Figure 1.4**. A critical element in getting a high output voltage from a thermopile is thermal isolation, which maximizes the temperature differential between the hot and cold junctions for a given absorbed power. To accomplish this thermal isolation between hot and cold junctions, thermocouples are often mounted on top of dielectric diaphragms that have had the silicon removed to enhance the thermal resistance.
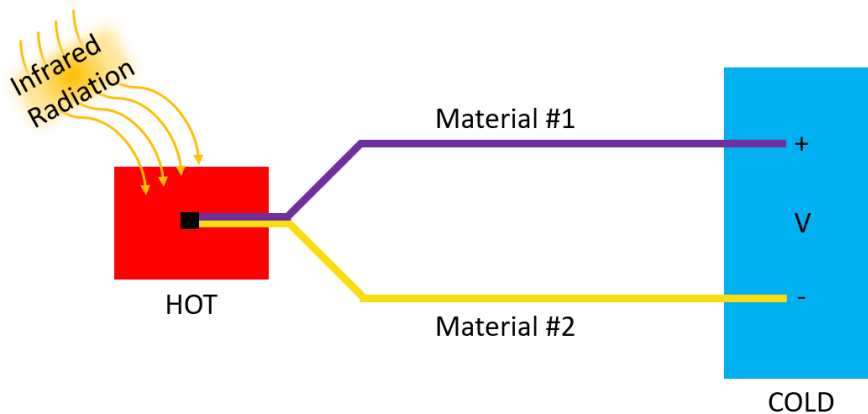
Figure 1.4: The basic representation of the thermoelectric detector.

The induced open-circuit voltage can be expressed as

$$\Delta V = \alpha_s \Delta T \qquad (1.3)$$

$$V_{induced} = (\alpha_{material\ \#1} - \alpha_{material\ \#2})(T_{hot} - T_{cold}) \qquad (1.4)$$

where $V_{induced}$ is the induced voltage as an output in the thermocouple, α is the Seeback coefficient, and T is the temperature of the hot and cold areas. As seen in Equation (1.4), differences in the Seeback coefficient should become more effective. As a material selection, semiconductors are a great candidate because of their high Seeback coefficient. For example, semiconductors like Ge, InAs, and Bi_2Te_3 have -548, -180, and 190 µV/K, respectively, as Seeback coefficients. Seeback coefficient of the semiconductor depends on the variation of the Fermi Level of the semiconductor with respect to temperature; therefore, for semiconductor thermopiles, the magnitude and sign of the Seeback coefficient can be adjusted by adjusting the doping type and doping level [15]. Apart from these materials, metals like Au, Ag, and V have 1.94, 1.51, and -5.28, respectively [16].

1.2.2 Pyroelectric Detectors

Pyroelectric detectors are devices that monitor the temperature change induced by infrared radiation by using pyroelectric materials. Pyroelectric materials are those that alter their polarization in response to temperature changes. Pyroelectric detectors can only operate in the alternating current mode, as free charges cancel out the obtained polarization in the direct current mode. As seen in the **Figure 1.5**, the current flowing into or out of a pyroelectric detector made out of two electrodes in between, which is a pyroelectric material, is given by [17]

$$I = Ap\frac{dT}{dt} \tag{1.5}$$

where A is the area of the electrodes, p is the pyroelectric coefficient, and dT/dt is the rate of temperature change.
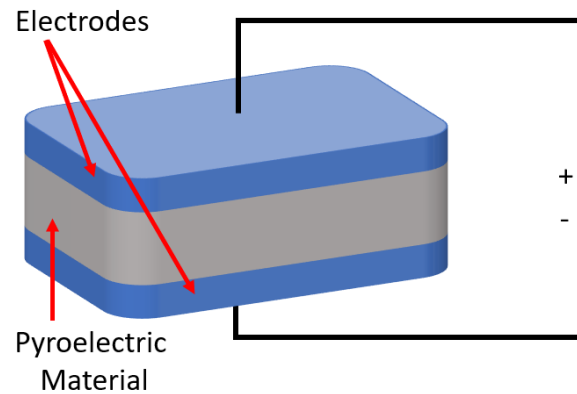
Figure 1.5: The basic representation of pyroelectric detector.

Some parameters determine the performance of the pyroelectric sensor. The characteristics of the detector are materially influenced by the propagation of the heat flux. In electrical characteristics of the detectors are highly structure/geometry dependent. It particularly depends on the location of the detector films in relation to other elements [18].

1.2.3   Microbolometer

A microbolometer is simply a temperature-sensitive diode or resistive membrane that is hanging in the air. The suspended component known as the microbolometer pixel body is attached by long thin support arms which are attached to the substrate, as seen in **Figure 1.6**. This modern suspended microbolometer pixel structure was developed initially by Honeywell, Inc [15]. The body is partly insulated from the substrate. The idea is to read the change in diode or resistance of the active temperature-sensitive material proportionate to the amount of incoming infrared radiation absorbed and keep it in the pixel body. Due to IC and MEMS technology advancements, microbolometers can be built on top of CMOS integrated circuits (ICs).
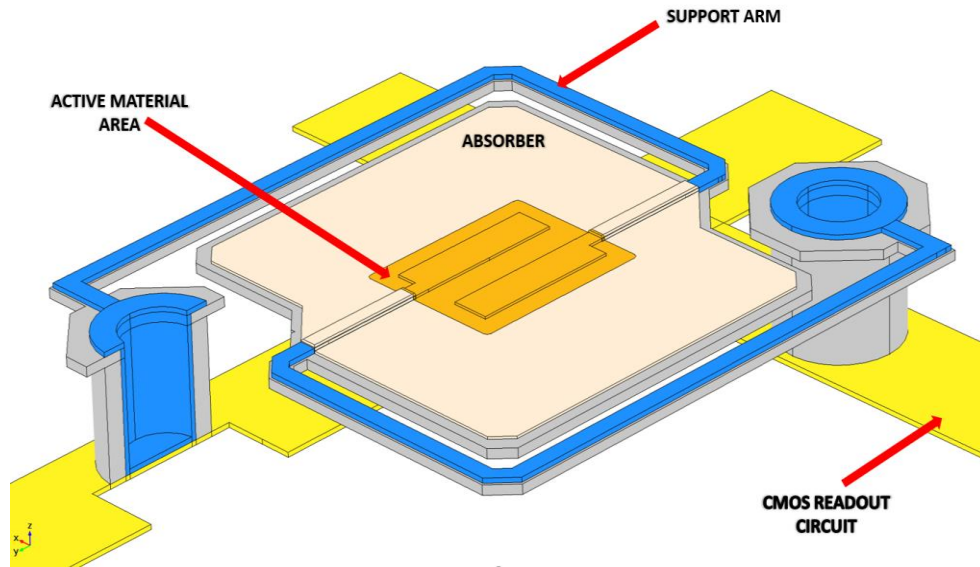
Figure 1.6: A general graphical representation of resistive microbolometer pixel.

The design can be changed with the detection mechanism. The diode-type bolometers are generally fabricated with a bulk micromachining technique. However, resistive type is mostly fabricated with surface micromachining technique on the ROIC.

1.2.3.1   Diode Type Microbolometer

The diode-type microbolometers have low sensitivity, low fill factors, and high time constants than monolithically fabricated counterparts. They may, however, be directly incorporated onto CMOS substrates, significantly reducing the cost and complexity of the manufacturing process [19]–[22]. These detectors are manufactured entirely using conventional etching methods and do not need any extra processes. They are often evaluated for low-cost applications where picture quality is less critical because of its low fill factor, low effective TCR. As an example of these types of detectors, **Figure 1.7** shows the SEM images of the diode type detectors. Since these detectors cannot be implemented in a standard CMOS process,

reducing their costs to the limits that ultra-low-cost applications require would be difficult. For ultra-low-cost applications, the best approach would be to implement the detector arrays together with their readout circuitry fully in standard CMOS, with some simple post-CMOS micromachining steps [15].
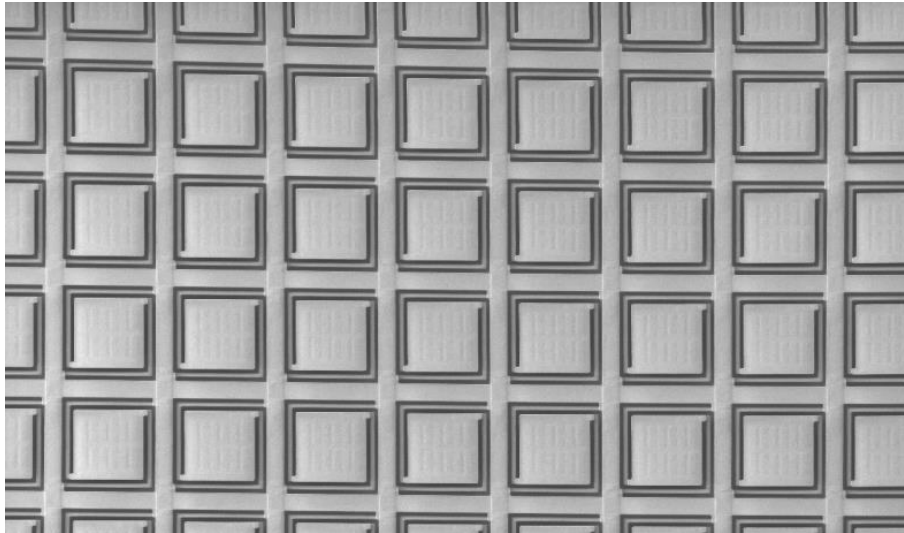
(a)
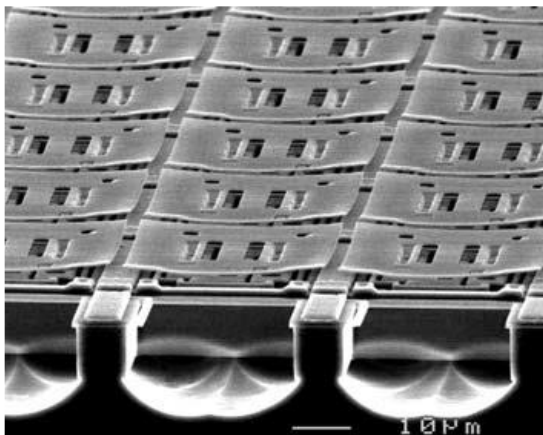
(c)
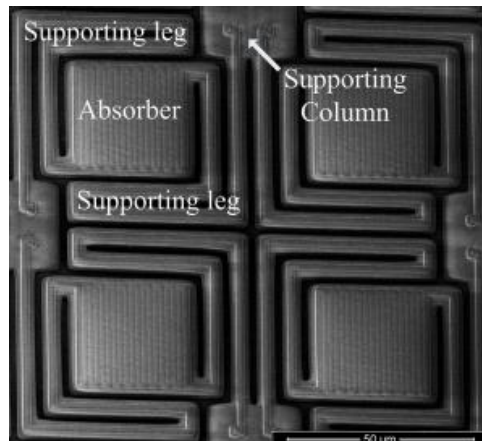
(d)

Figure 1.7: SEM images of the diode-type microbolometers (a) previously fabricated at METU [23], (b) fabricated by Mitsubishi [24], and (c) fabricated by Liaoning IC Technology Key Laboratory [21].

1.2.3.2   Resistive Type Microbolometer

The resistive type of bolometer has higher performance than the previously mentioned diode type counterparts. They use the temperature coefficient of resistance (TCR) of the active material used in the detectors as the sensing mechanism. When the heat is absorbed from the body and the temperature increases, the resistance value of the structure will end up decreasing in the resistor structure. This case uses a semiconductor material in the resistive material. If the material is selected as a metal, the resistance will increase because of the natural properties of the materials [25]. Since Honeywell, Inc. put effort into the first resistive type of microbolometer development. Then, many organizations flourished in the field. Raytheon, BAE, DRS, Indigo, and NEC are a few company's that being in the field with the usage of VOx as an active resistive material [26]–[30]. Another important material is amorphous silicon (a-Si), which LYNRED and L-3 use to build microbolometers with very high resistive characteristics [27], [31], [32]. Yttrium Barium Copper Oxide (YBCO) has also been used by Canada Defence Research and Development and P. Butler, Çelik-Butler [33], [34] and researched at METU [35], [36]. Also, poly-SiGe is studied by LYNRED and Leonardo DRS [37]–[39].

(a)   (b)
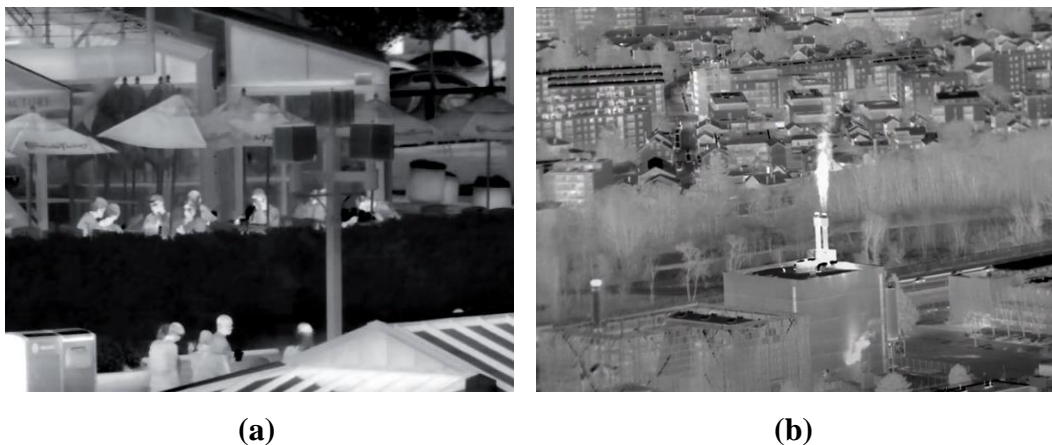
Figure 1.8: Infrared images obtained by (a) Leonardo DRS [40] and (b) LYNRED [41].

Figure 1.8 shows infrared images taken from studies of various companies. They fabricate a small size pixel. The recent trend in the resistive microbolometer market is to reduce the pixel size to increase the FPA format, as expected, and to move designs towards multi-level structures to increase the fill factor. **Figure 1.8.(a)** fabricated as 10 µm [40] and **Figure 1.8.(b)** fabricated as 12 µm [41] pixel pitch. Also, SEM images of some detectors are shown in **Figure 1.9**.

(a)

(b)

(c)

(d)
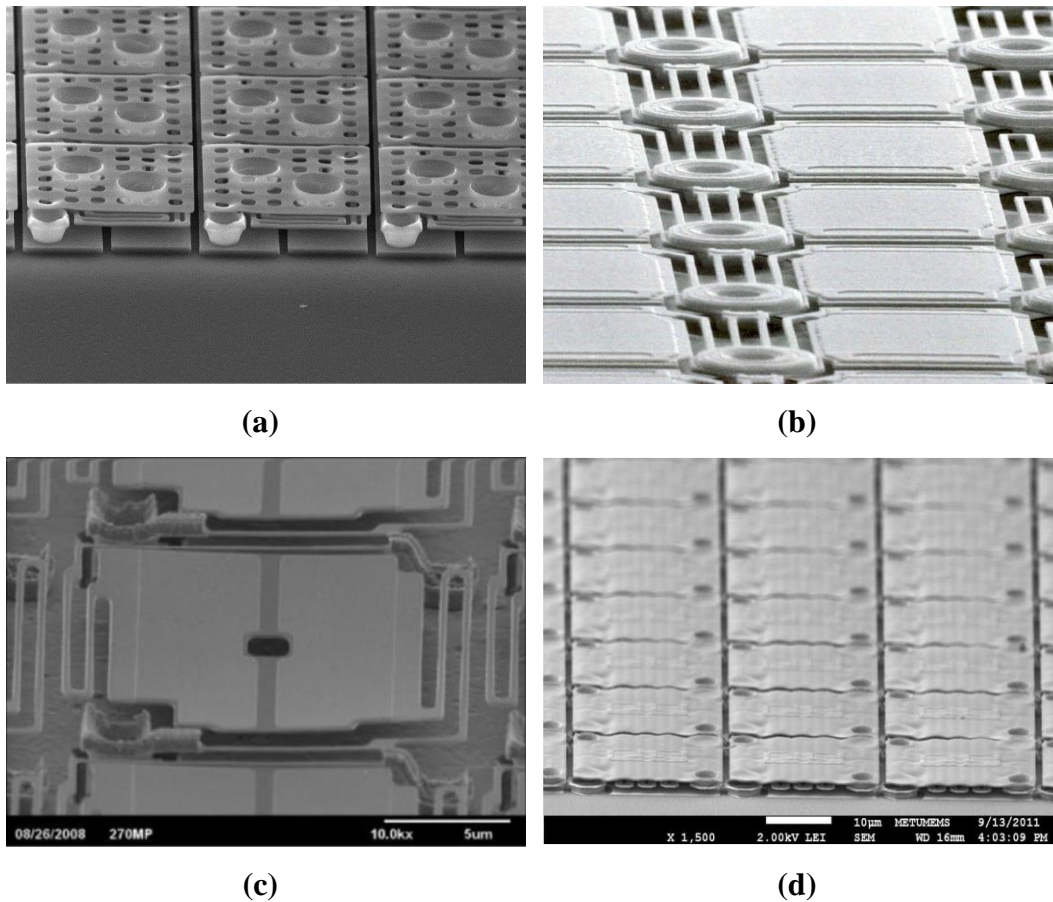
Figure 1.9: SEM images of microbolometer FPA's that fabricated by (a) VOx umbrella design microbolometer from DRS [42], (b) VOx bolometer from BAE [43], (c) a-Si/a-SiGe microbolometer from L-3 Communications [27], and (d) YBCO microbolometer from METU [35].

1.3   The Figures of Merit for Microbolometers

The performance criteria for the focal plane microbolometer detectors and arrays are covered in this section.

1.3.1   Temperature Coefficient of Resistance (TCR)

The temperature coefficient of resistance (TCR), denoted as α, related to the resistive type microbolometer, is one of the most critical parameters. The temperature rises after absorbing incoming radiation. Part of the heat is conducted to the substrate. Some are re-radiated, which is generally ignored, and some of them give rise to increase temperature. The greater the heat is absorbed, and less heat is conducted to the substrate cause a temperature rise in the pixel body. This high-temperature change significantly affects the resistance value related to TCR, which is given as:

$$\alpha = \frac{1}{R}\frac{dR}{dT} \tag{1.6}$$

where R is the detector resistance, and T is the temperature. There are mainly two types of material that are used as an active region in microbolometers. As IR active materials, metals have a positive TCR, and semiconductors have negative TCR values [25]. If the material has negative TCR, resistance values get lower as the temperature rises.

For semiconductors, electrical conductivity (σ) depends on free carrier mobility (μ), which weakly depends on the function of temperature, and carrier concentration, a strong function of temperature [44]. Moreover, TCR is also related to the material's activation energy (E_a), shown in Equation (1.8) called Arrhenius Equation.

$$\alpha = -\frac{E_a}{k_B T^2} \tag{1.7}$$

and

13

$$R(T) = R_0 e^{E_a/k_B T} \tag{1.8}$$

where k_B is Boltzmann constant, and T is temperature. Equation (1.7) gives the other version of the TCR, where it changes with varying temperatures. However, there is a trade-off between resistance and noise parameters [45]. In order to get a high response in the pixels, high TCR and optimized resistance are required. If the optimized resistance is high, it brings high thermometer noise, negatively affecting the system's performance.

1.3.2   Thermal Conductance (G_{th})

In order to isolate the system from the substrate, thermal conductance has a significant role in microbolometer performance. The lower thermal conductance gives better isolation for the pixels, which keeps the heat on the pixel body. This isolation results in a better performance for microbolometer pixels. Thermal conductance can be categorized into three parts which are arms, conductional heat loss, and gas convection.

$$G_{th} = G_{th,arms} + G_{th,radiative} + G_{th,gas} \tag{1.9}$$

while pixels operate under vacuum conditions, convectional heat loss and gas conductional loss can be ignored. The thermal conductance by supporting arms and radiation-based conduction is dominated. So, the two support arms' feedback into thermal conductance can be explained by the heat flow equation [25].

$$G_{th,arms} = 2 \sum_{k}^{n} \sigma_k \frac{A_k}{l} \tag{1.10}$$

where σ_k is the thermal conductivity of the kth material, A_k is the cross-sectional area, and l is the length of the support arms.

$$G_{th,radiative} = 4\eta k_B A_D T^3 \qquad (1.11)$$

where η is the absorptance of the body, k_B is the Stefan-Boltzman constant, A_D is the active absorber area of the pixel body, and T is the temperature. Therefore, if it is considered that radiative conductance is much smaller than thermal conductance of the support arms, the only dominant factor is $G_{th,arms}$. So, it can only be taken into considerations.

1.3.3   Thermal Time Constant (τ)

The thermal time constant is a parameter of the pixel's response time to heat up (or cooldown). It will show how quickly a pixel will change its temperature.

$$\tau = {C_{th}}/{G_{th}} \qquad (1.12)$$

where C_{th} is the heat capacity of the main dominant layers, and G_{th} is thermal conductance. The heat capacity is mainly determined by the heat capacity of the suspended body. The reason for that the contribution of the support arms is relatively small than pixel body.

For the applications that require a high frame rate, this parameter becomes too important. If a high frame rate requires, a low thermal time constant is the must. The frame rate of the IR microbolometers is generally determined as [46]:

$$f_{frame-rate} = \frac{1}{3\tau} \qquad (1.13)$$

The frame rate can be tailored by adjusting the response time for desired applications.

1.3.4   Responsivity ($\Re$)

Responsivity can be summarized as a ratio of an output signal of the detector with respect to incident IR radiation. The output signal can be expressed as a voltage or current responsivity.

$$\Re_V = \frac{output\ voltage\ change}{incident\ IR\ power} = \frac{\Delta V}{\Delta P}\ [V/W] \tag{1.14}$$

$$\Re_I = \frac{output\ current\ change}{incident\ IR\ power} = \frac{\Delta I}{\Delta P}\ [A/W] \tag{1.15}$$

where V is voltage, I is current, and P is incident IR power. When a detector is biased with current, the output voltage change (ΔV) can be expressed as

$$\Delta V = I_d \Delta R = I_d \alpha R_d \Delta T \tag{1.16}$$

where I_d is biased current, α is active material's TCR, R_d is detector resistance, and ΔT is the temperature change of the bolometer. This temperature change as

$$\Delta T = \frac{\eta \beta A_D P_0}{G_{th}\sqrt{1 + (\omega\tau)^2}} \tag{1.17}$$

where η is the absorption of the detector, β is the fill factor of the detector pixel, A_D is the area of the detector pixel, P_0 is the power of the incident IR radiation, G_{th} is thermal conductance of the detector pixel, ω is the modulation frequency of the incident IR radiation, and τ is the thermal time constant. By aggregating the Equation (1.17) and Equation (1.16) into Equation (1.14), the result shows the voltage responsivity ($\Re_V$) of the detector, which can be shown as

$$\Re_V = \frac{\Delta V}{P_0 A_D} = \frac{\eta I_d \beta \alpha R_d}{G_{th}\sqrt{1 + (\omega\tau)^2}} \tag{1.18}$$

1.3.5 Noise

There is various type of noise conditions that contributes total noise of the microbolometers. This cumulative accumulation in noises degrades the bolometer performance. Apart from generated noise from readout integrated circuit (ROIC), microbolometer noise is much more dominant. Because of the natural working principle of the microbolometers, which is the conversion of radiative heat into electrical energy, electrical and thermal noises are present. The noise magnitude generally depends on the noise bandwidth which is taken equal to the pulse duration onto the pixel. The bandwidth is given as:

$$\beta = {}^{1}/_{2\Delta t} \qquad (1.19)$$

where Δt represents pulse duration. In particular, Johnson noise, 1/f noise, temperature fluctuation noise, and background noise are the four dominant noise types.

1.3.5.1 Johnson Noise

This noise type is mainly the reason for voltage fluctuations across the microbolometer. At a temperature T, the materials may create johnson noise due to the charger carriers' unwanted behaviors that move arbitrarily. This noise type can be considered as a "white noise". In a given bandwidth, Johnson noise (V_j) is represented as:

$$V_j^{2} = 4k_B T R_B \beta \qquad (1.20)$$

where k_B is Boltzmann constant, T is the bolometer temperature, R_B is the bolometer resistance, and β is bandwidth corresponding to integration time.

1.3.5.2   1/f noise

1/f noise generally occurs in thin films. Depending on the usage of conductors or semiconductors, this noise may result from imperfections in the resistor structure and electrical contacts. The fluctuation in the resistance is the cause of changes in the electrical conductivity of the material. This change mainly depends on the free carrier density and its mobility [46]. Also, there are possible reasons for 1/f noise like [13]:

- generation-recombination mechanisms in semiconductors
- migration of impurities
- local temperature fluctuations (mainly in thin layers) and etc.

This noise type is really important in the microbolometer performance. The system's design, like deposited material, deposition techniques, and contact types, affects the noise behavior.

1.3.5.3   Temperature Fluctuation Noise

Thermal noise rises from random energy exchange between microbolometer and substrate. This noise is also called phonon noise. Temperature fluctuation ΔT can be expressed as

$$\Delta T^2 = \frac{k_B T^2}{C_{th}} \tag{1.21}$$

where k_B is Boltzmann constant, C_{th} is specific heat capacity, and T is temperature. The temperature change in both substrates is considerably significant with respect to pixel body, and pixel also creates a temperature variation between them even with minor changes. So, these changes cause a fluctuations noise.

$$V_{TF}^2 = \frac{4k_B T G_{th} \Re^2}{\eta} \tag{1.22}$$

where k_B is Boltzmann constant, T is Temperature, G_{th} is thermal conductance, $\Re$ is responsivity, η is absorptance. This noise type is considered small if it is compared with Johnson and 1/f noise. Also, background fluctuation noise is considerably small, which heat exchange by means of radiation only. That is why background fluctuation noise can be ignored while other noises are more dominant. The total noise affects the bolometer performance obtained by adding these dominant noise conditions together.

$$V_{TOTAL}^2 = V_{Johnson}^2 + V_{1/f}^2 + V_{temperature\ fluctuation}^2 \qquad (1.23)$$

As seen in **Figure 1.10**, Johnson noise does not affect by applied bias. However, other noise types are affected by the bias. Generally, under bias voltage, the RMS of the temperature fluctuation is independent. Additionally, more voltage response can be achieved if more bias is applied, which positively affects the voltage responsivity. However, at the same time, background fluctuation noise and thermal fluctuation noise also increase.
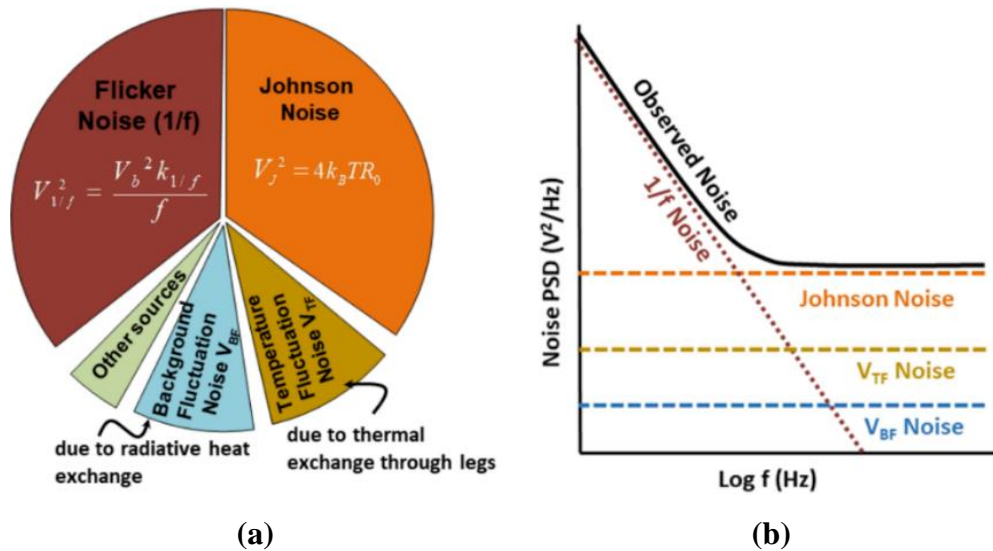
Figure 1.10: (a) Contribution of all major noise sources and (b) the observed noise as the sum of all the major noise components [47].

1.3.6   Noise Equivalent Power (NEP)

Noise equivalent power shows the relation between absorbed power and pixel noise. It represents the radiant flux that produces a signal equal to total RMS pixel noise. It is one of the parameters to compare the detectors' performances. It is shown as

$$NEP = \frac{i_n}{\Re_i} \ or \ \frac{v_n}{\Re_v} \tag{1.24}$$

where current noise i_n and responsivity $\Re_i$ (or voltage noise v_n and responsivity $\Re_v$).

1.3.7   Noise Equivalent Temperature Differences (NETD)

NETD is the most important parameter for IR imaging systems. In a very simple way, NETD gives very generic information about microbolometer performance. This parameter shows the differences in the temperatures of the scene. It is given as

$$NETD = \frac{4(F_\#^2+1)V_{TOTAL}}{\tau_0 A_D \Re (\Delta P/\Delta T)_{\lambda_1-\lambda_2}} \tag{1.25}$$

where $F_\#$ is the focal ratio of the optics, V_{TOTAL} is the total noise voltage, τ_0 is the transmittance of the optics, A_D active detector area, $\Re$ is responsivity, and $(\Delta P/\Delta T)_{\lambda_1-\lambda_2}$ is the change by changing the temperature of the power per unit area emitted by the black body at temperature T. It measured within the spectral bandwidth between 8 µm and 14 µm at 295 K, the value of $(\Delta P/\Delta T)_{8-14}$ is 2.62 x 10^{-4} W/cm^2 deg K. For microbolometers, low NETD value shows good performance.

1.4   Research Objectives and Thesis Organization

The aim of this research is to develop thermally improved single-level resistive microbolometers with 12 pixels size that employ a planar type resistor structure. The designed detectors are fabricated using surface micromachining technology. They are compatible with post-CMOS processes to reserve the capability to integrate them with ROIC monolithically. The main items of research objectives can be listed as follows:

1. Design and optimization of a suitable resistor structure and a single-level resistive microbolometer detector:
   The design of the pixel and the development of a viable fabrication flow are equally important, and they should be addressed accordingly. A reasonable resistance value and TCR should be obtained with a high-performance active material using a resistor structure that does not impede the other performance parameters such as absorption and thermal time constant. The resistor structure should also occupy a small area to demonstrate its applicability to smaller pixels. Thermal conductance of the pixel plays a pivotal role in the overall performance, and it should be the primary concern for any design work.

2. Modeling of the detector to improve performance:
   The pixel design should be optimized, and performance should be predicted through proper modeling of the detector structure. Thermal modeling of the detector is crucial in terms of performance based on thermal conductance, and modeling of absorption characteristics is vital to obtain high performance. The performance predictions and mechanical stability should be affirmed via reliable simulations.

3. Development of a viable fabrication flow:
   The individual properties of all layers in the detector and their integration should be taken into account in developing an optimized fabrication flow while maintaining compatibility with post-CMOS processing.

4. Tests of fabricated pixels:

    The proposed detectors should be tested after proper fabrication, and performance parameters should be extracted to demonstrate the applicability of the detector and resistor structure.

The content of the thesis is given below:

Chapter 2 discusses and elaborates on the design of the surface micromachined microbolometer pixels and the resistor structures, along with the simulations and theoretical modeling that are used to optimize the detector parameters.

Chapter 3 summarizes the determination of the fabrication process flow. It starts with the design of the process flow. Then, the individual optimization for each process step is explained in detail.

Chapter 4 gives the test results obtained after the fabrication of the pixels and FPA. Performance parameters of the pixels are given in this chapter.

Chapter 5 summarizes the research carried out within the context and scope of this work, concludes the thesis, and proposes future work that can be done to improve the results further.

CHAPTER 2

DESIGN OF THE MICROBOLOMETER PIXEL

This chapter focuses on resistor designs, thermal and optical performance of surface micromachined -12 µm pitch- microbolometer pixels, and calculations of theoretical models required to improve the detector performance. While performing electro-thermal, mechanical simulations are done with COMSOL Multiphysics, and absorption simulations are done with MATLAB software.

2.1   Resistor Structure

Planar resistors are the most common, simple, and easy way of manufacturing microbolometer resistors. **Figure 2.1** and **Figure 2.2** show the 3-D side view of planar-type resistors. The active material (VWO_x) is deposited laterally in the layer between the metal electrodes, forming a resistance there. Bu, the geometry is limited because of the limited area.
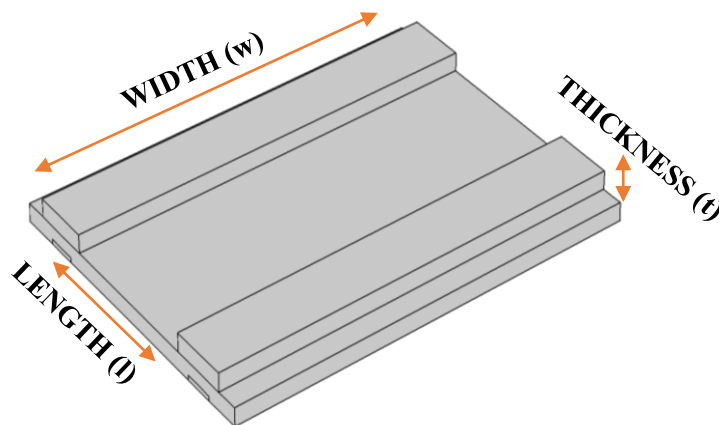
Figure 2.1: Side view of the standard type planar electrodes.
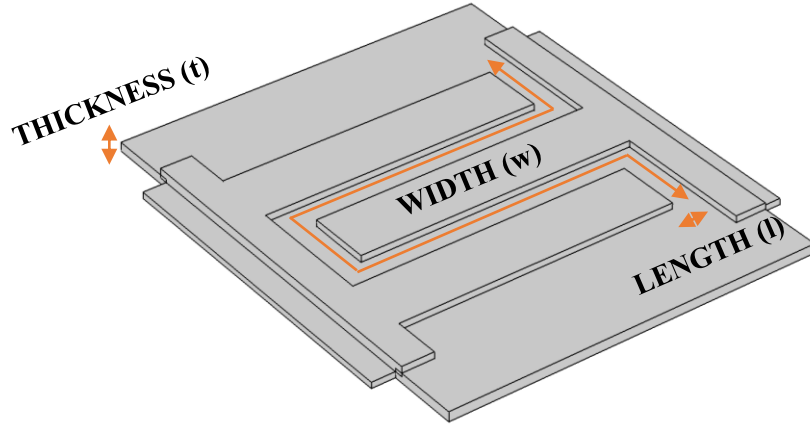
Figure 2.2: Side view of the finger type planar electrodes.

Before simulating the pixel structures, it plays a critical role in the electrode structures as the first stage of simulations. It should be determined that the range of the pixel resistance. The evaluations are to be made on the values determined here. The determination of the electrode structures to be placed on the pixels. In the simulations, resistance calculations on the electrode and active material combinations are calculated as:

$$R = \rho \frac{l}{wt} \tag{2.1}$$

where "ρ" is the resistivity of the active material, "l" is the length between electrodes, "w" is the width of the electrodes, and "t" is the thickness of the active materials. As previously mentioned, "l" determines the electric flow of the active material. Minimize the number of fingers is used to minimize the reflectivity on the surface caused by electrode metal and reduced absorption by active material. By using low resistivity active material, manipulating l/w ratio helps to achieve desired resistance.
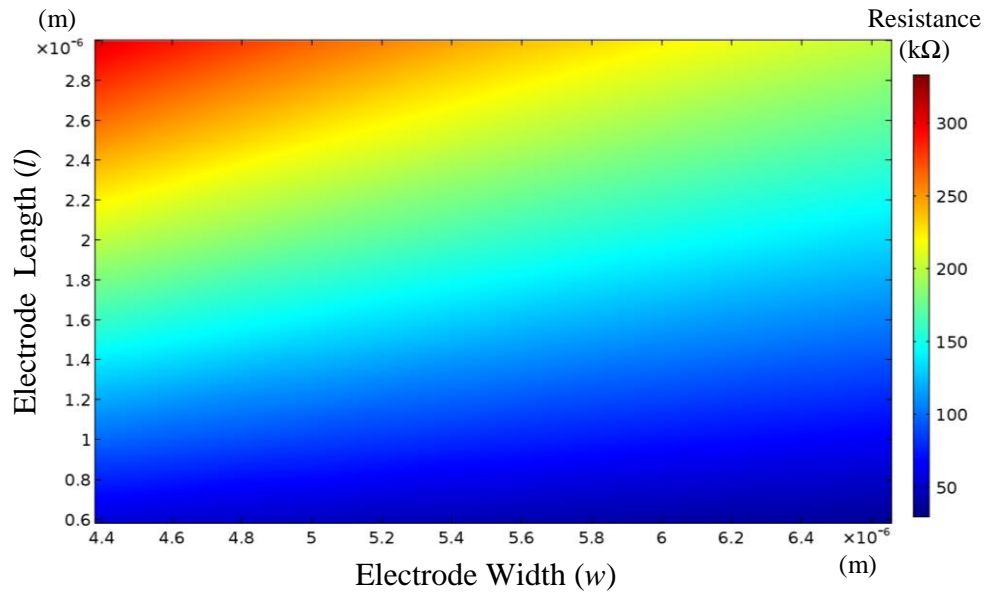
(a)
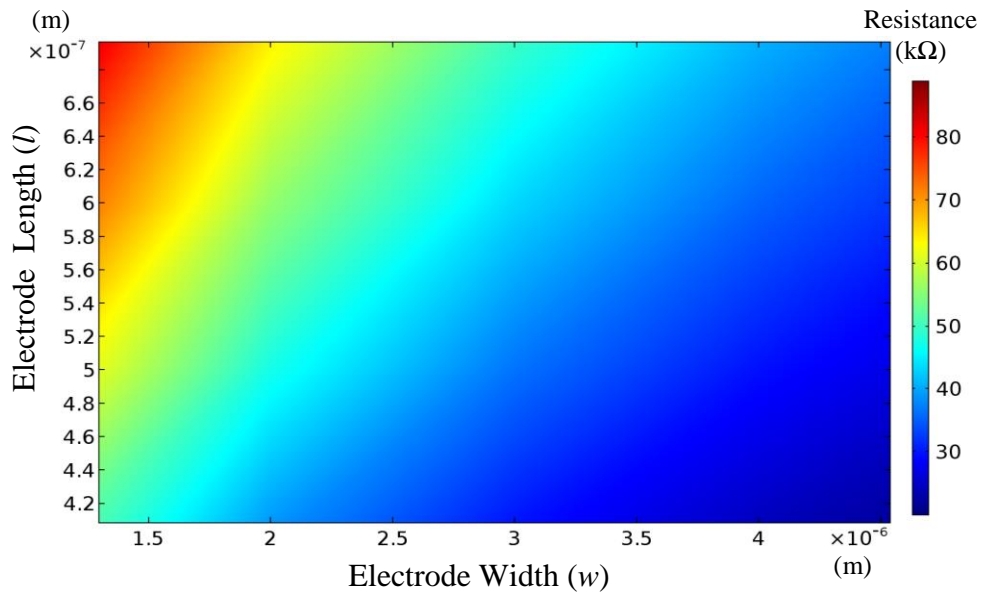
(b)

Figure 2.3: Changing the resistance (Ω) value of the "electrode structure" in terms of electrode width (w) and electrode length (l) with constant active material resistivity (ρ) and thickness (t) (a) standart type and (b) finger type planar electrode structure, where electrode structures are taken as reference in **Figure 2.1** and **Figure 2.2**.

The resistance evaluation with a constant active material thickness (~240 nm) is given in **Figure 2.3** by using Equation (2.1). While calculating the resistance values, the resistivity of the VWO_x is taken as 9 Ω.cm [48], which can be optimized with W doping rate. Using these resistance color graphs, the trend in the desired resistance values is determined roughly between 50-120 kΩ in order to get the best possible performance considering the self-heating effect [49].

(a)   (b)
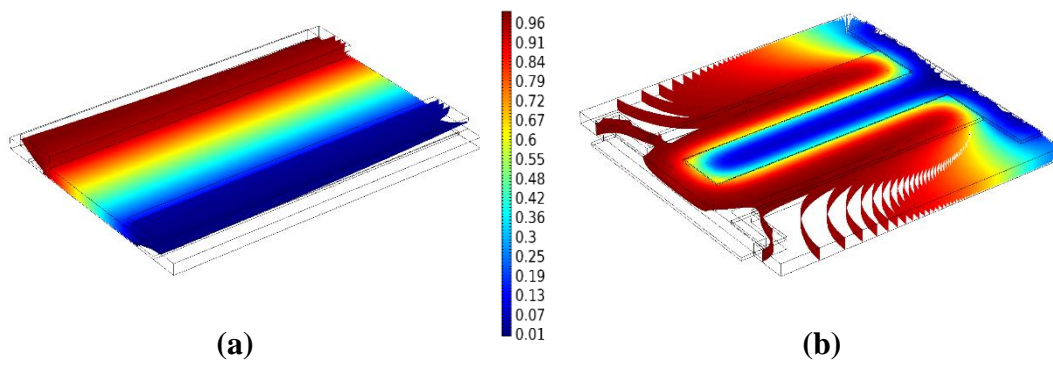
Figure 2.4: Side view of the normalized potential differences between electrodes (a) standard type and (b) finger type planar electrodes.

The normalized potential difference between electrodes, where the electric current presents, is shown in **Figure 2.4**. The figures show that the parallel structures (**Figure 2.4** (a)) have a more linear flow between electrodes. However, finger structure (**Figure 2.4** (b)), which has three fingers present in our case, has not equal flow between the electrodes. The current flows into the center electrode by the surrounding electrode structure. Also, the bases of the electrode structures contribute to the flow, which may create a resistance variation and noise.

2.2 Design of the Pixel Structures

The pixel pitch of an infrared detector has a substantial impact on all of its performance characteristics. A larger detector size allows for greater space for the resistor, thermal isolation arms, active region and looser design constraints, and simpler fabricating of the pixels. On the other hand, smaller pixels allow the imaging system designer to build arrays with bigger sizes, which is a significant benefit, particularly when it comes to picture quality. Alternatively, when considering an array of the same format, a smaller pixel size results in a smaller total array size, allowing for the use of shorter focal length lenses, reducing the overall system size, and improving mobility. Thus, smaller pixel sizes are possible and are usually targeted towards the final product's quality and affordability. Designing the 12 µm pixels opens a window into the production of CMOS wafers.

2.2.1 Absorption Simulations of the Pixel Structure

In Section 1.1, electromagnetic radiation is divided into three categories based on their wavelengths: infrared, visible, and ultraviolet. Electromagnetic laws may be applied to infrared detectors since infrared radiation and light are representations of the same phenomenon. For microbolometer detectors, the Cascaded Transmission Lines (CTL) method may be represented using structures with many layers stacked on top of each other, which can be represented as a transmission line. This method was previously studied in METU-MEMS Center [35], [36], [50]. As observed from the input, like seen in **Figure 2.5**, the layer model represents all layers as parallel transmission lines. A microbolometer contains an absorber layer, structural layers, interconnect metal, active material, cavity, and reflector metal in the model. In order to achieve maximum absorption, all power must be dissipated on the absorber, which may be accomplished by setting the total characteristic impedance of all other layers to a near-open circuit value. Although such a thing is theoretically feasible due to the materials' characteristics, very high absorption rates are still reachable.
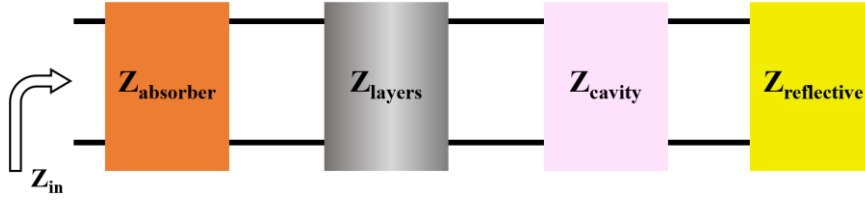
Figure 2.5: Representative view of CTL model inputs of the microbolometer.

Adjusting the layer characteristics and thicknesses to get maximum absorption is achievable. However, this can be possible only if the microbolometer's structure is uniform throughout the pixel geometry, which is practically impossible. Examples include electrodes used to make electrical contact with active material, which function as reflector materials and change the equivalent impedance at those places. To get overall absorption can be calculated by dividing the microbolometer structure into areas with various layer combinations, as shown in **Figure 2.6**. Because the given structure's, which is the general structure of the pixel, has three different regions with different layer stacks, the total absorption calculations can be calculated with

$$Abs_{total} = Abs_1 \frac{A_1}{A_{total}} + Abs_2 \frac{A_2}{A_{total}} + Abs_3 \frac{A_3}{A_{total}} \qquad (2.2)$$

where Abs_{total} is the total absorption of the pixel body, Abs_x is the absorption of the specified area, A_x is the area of the specified region, and A_{total} is the total area of the pixel body (12 µm pixel pitch) that light pink area of the pixel that given in **Figure 2.6**.
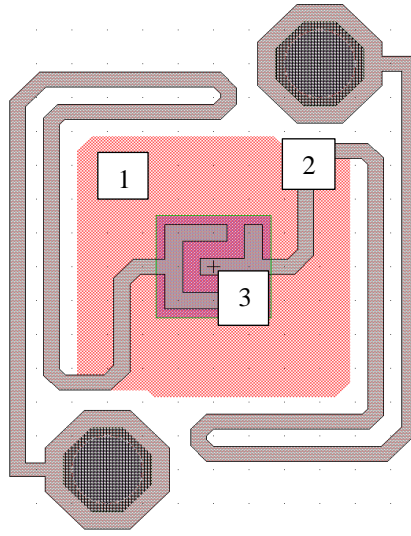
Figure 2.6: Different regions on 12 µm pixel pitch microbolometer structure.

Region #	Layer Stack	Area [µm²]
1	Absorber – Si_3N_4 – Cavity – Au	40.8
2	Absorber – Si_3N_4 – NiCr	5.2
3	Absorber – Si_3N_4 – Top Metal on Active Material	9.8

This model is previously studied in METU MEMS Center [36], [50], [51]. Layer stacks for each region's absorption calculations are done. Overall absorption is calculated with Equation (2.2). However, before taking the layer's thickness, how does each layer thicknesses affects the absorption value. However, among these layers, the NiCr absorber layer's thickness is taken as 5nm with 377 $\Omega/\square$ surface resistance. [52]–[54]'s studies show that these values show the best performance. Also, coating a relatively thin layer as an absorber helps not to increase the thermal mass of the pixel. **Figure 2.7** shows how these layers contribute the achieve max absorption for the layer stacks. From this simulation, structural material's and cavity thickness are taken as 200 nm and 2.5 µm, respectively, because maximum absorption is achieved around these values. Around these values, the absorption characteristic of the pixel body is achieved around a maximum of 98 %.

Table 2.1: Optical constants used in simulations.

	Refractive Index	*Extinction Coefficient*
Structural Layer	1	1.3
Absorber	1	0.5
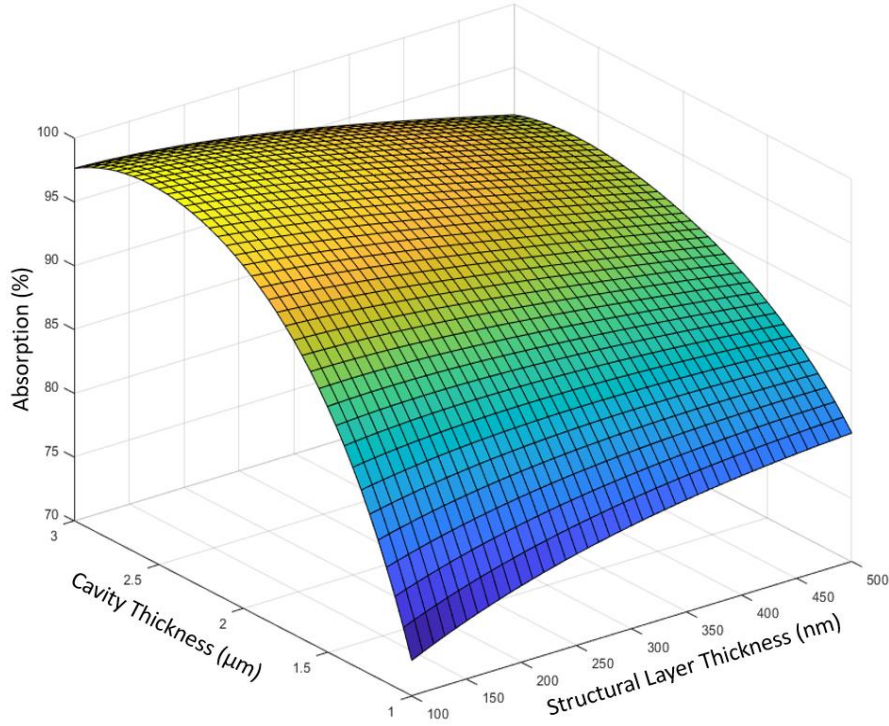
Figure 2.7: Variations in absorption (%) with structural layer and sacrificial cavity layer thickness change.

The plot displays the entire detector's absorption properties as well as various sections. The Region 2 absorption coefficient is the lowest of all, and it has a significant impact on the weighted average. Region 1 and Region 3's effective surface area would increase the absorption coefficient. To enhance LWIR absorption, adjust the process parameters to produce a peak around the wavelength of 10 μm. In this area, the detector's absorption efficiency is almost 95%. This value is relatively high and comparable for the high-end microbolometer community.
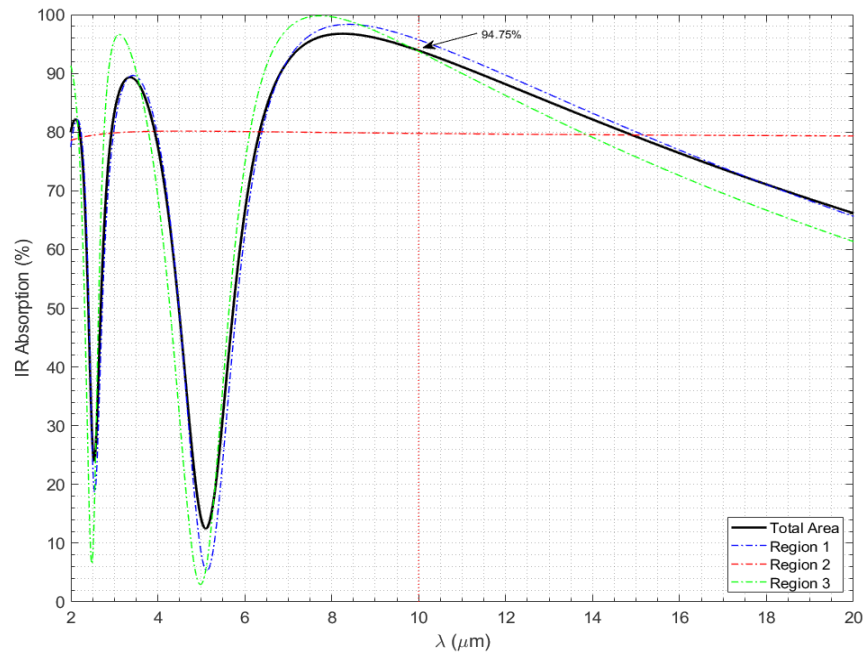
Figure 2.8: Absorption characteristic of the different regions for the detector pixel that illustrates in **Figure 2.6**.

2.2.2 Electro-Thermal Simulations of the Pixel Structure

A critical component of maximizing the detector's thermal isolation is optimizing the geometry. The thermal conductance denotes the degree of the thermal isolation between the detector and the substrate, as explained in Section 1.3.2. For the highest thermal isolation, this quantity should be as low as achievable. This may be done by providing support arms that are long and thin. However, as the length extends and thickness diminishes, the support arms become weak, making the support arms impossible to hold the detector's active area without buckling. Also, when the support arms grow longer, the detector's fill factor drops. The optimizations should be made between these parameters, and the most suitable positions should be determined to find the sweet spot for the best performance. Therefore, it is one of the objectives of this thesis to minimize the thermal conductance to a level that was considered acceptable with minimal compromising from the fill factor of the detector area.
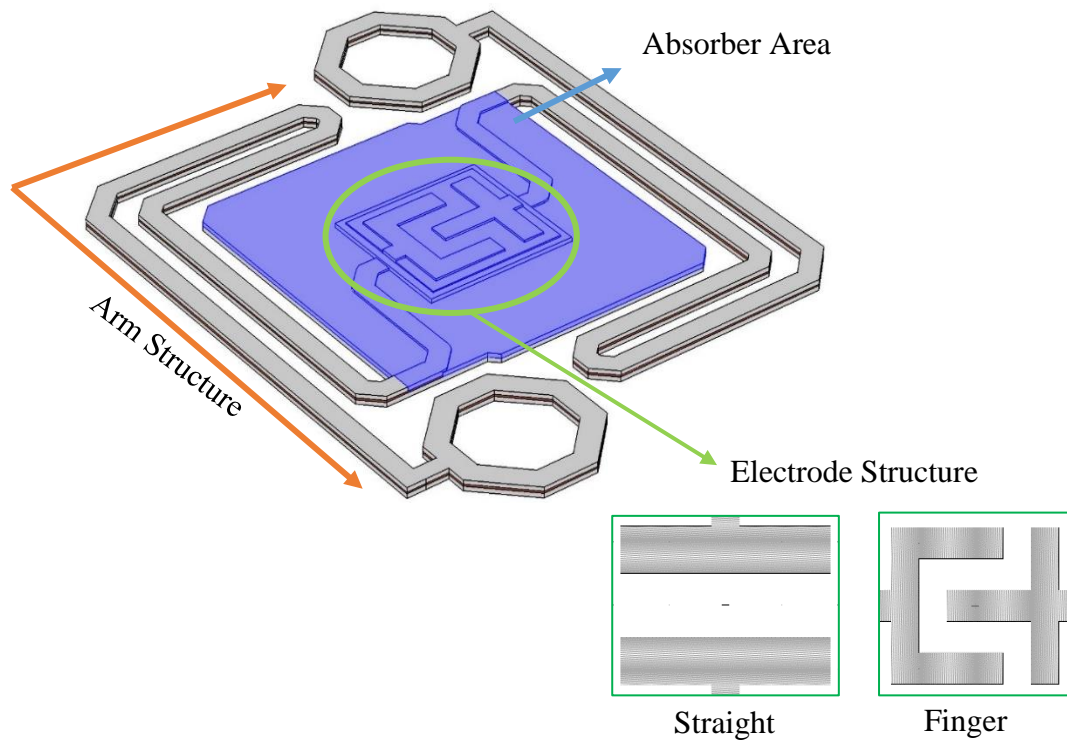
Figure 2.9: Side view of 3-D representation of the microbolometer structure.

While ensuring the thermal conductance is minimal, this must be considered that the thermal time constant is also affected by these parameter changes, which may not be critically reflected in the time constant. The reason for that when thermal conductance decreased by increasing the arm length, the heat capacity of the body also diminished.

After determining the electrode structures to be placed on the pixels, thermal conductance, G_{th}, which is one of the critical performance parameters in the design procedure of a microbolometer pixel, is emphasized. The thermal conductance of the support arms, $G_{th,arms}$, is the most dominant component of the total thermal conductance of the pixel, as discussed in Chapter 1.3.2. By considering these parameters, the purpose of the support arm design phase is to keep the thermal time as low as possible and reducing the thermal conductance value as much as possible.

In addition to the performance parameters, fabrication limitations is also taken into account, as mentioned earlier. The width of the arm metal and nitride layers, the arm spacing, and the width of the pixel anchor points' apertures are designed with certain limitations by the METU-MEMS Facility's fabrication capabilities. For this reason, the pixels are designed within the scope of these simulations are categorized into several different types according to the overall support arm lengths and widths.
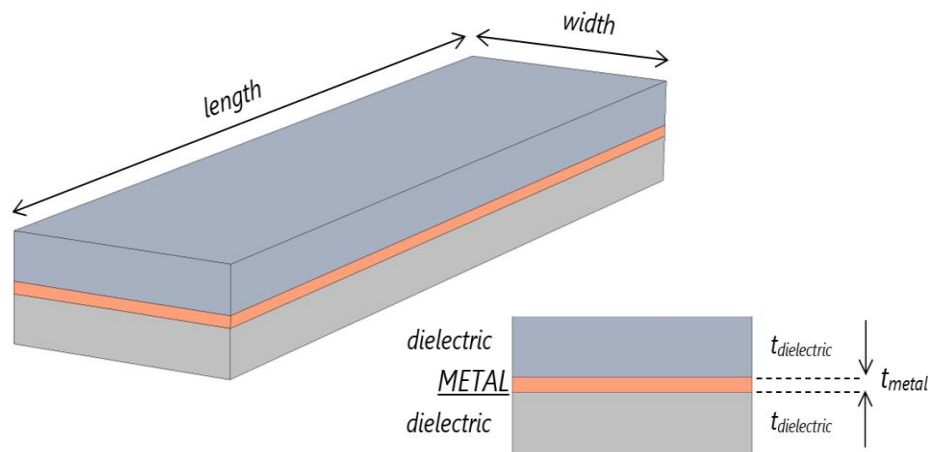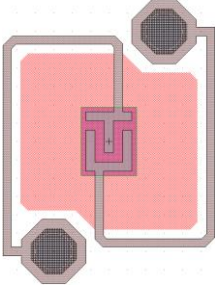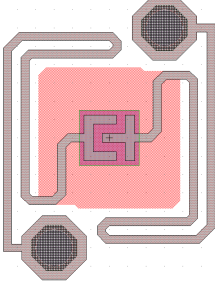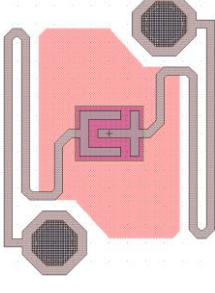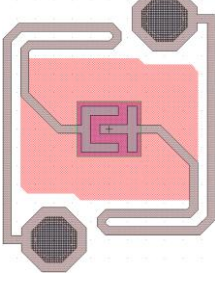
Figure 2.10: Representation of microbolometer arm structure's.

The thickness of the support arms also determines the thickness of the body structures of the pixels. Because, by considering the fabrication stages, pixel support arms and pixel body structures are created in the same fabrication steps. Therefore, this situation has been taken into account in the simulations and while creating the design structures. While the thermal mass increases with the thickening of the pixel body, the pixel time constant will also increase. In addition to these conditions, the percentage of pixel infrared absorption, pixel bending, and twisting, which will be discussed in the following sections, is affected. Even if the responsiveness of thin pixels varies by design, bending the pixels after removing the sacrifice layer can cause decreases in the absorption percentage and thermal short circuit due to contact with the surrounding pixels. These situations can cause considerable losses in the responsiveness of the pixels. All conditions are considered while making pixel simulations.

Table 2.2: General pixel geometries for 12 µm pixel pitch microbolometer.

2D view of General Pixel Geometries	Arm Width [µm]	Arm Length [µm]	Absorber Area [µm²]	Fill Factor [%]	Electrode Structure	Pixel Thickness [nm]
	0.45	17.5	84.4	58	Straight or Finger	Structural Nitride: 90/90
	0.50		83.0			
	0.45	31.0	58.3	40	Straight or Finger	
	0.50		55.8			
	0.45	23.2	76.1	52	Straight or Finger	Arm/ Electrode Metal: 50
	0.50		74.3			
	0.45	22.9	71.7	49	Straight or Finger	
	0.50		69.6			

The given four structures in **Table 2.2** show the 12 µm microbolometer structures'. These designs are general system geometries for comparing how arm length and arm width affect pixel absorber area with constants like spacing. These designs have sub-stages changing electrode structure, arm width, spacing. These four designs give a comprehensive perspective to observe which designs work more efficiently than others.

At first, pixels' thermal time constants are simulated. In order to do this, pixels' only exposed to IR radiation until thermal stabilization occurs. The exposure power on the absorber area is taken as 440 W/m^2 which is converted from 100 nW for energy applied on the pixel absorber area [46]. The temperature difference (ΔT) between the pixel at room temperature (at 25 °C) and the pixel at a stabilized temperature under IR radiation help to find the thermal time constant.

$$\Delta T = \Delta T_0 \exp(-{t}/{\tau}) \tag{2.3}$$

where ΔT is a temperature difference, T_0 is the initial Temperature (at room temperature, 25 °C) before IR exposure, t is time, and τ is the thermal time constant. The selected design structures' thermal time constants with determining main graphical designs have less than 3 ms that seen in **Figure 2.11**. The shorter time constant value gives fast responses. The pixels thermal time constant is low than most of the commercial and academic works. Different design structures with geometrical parameters can be found in **Table 2.4**.
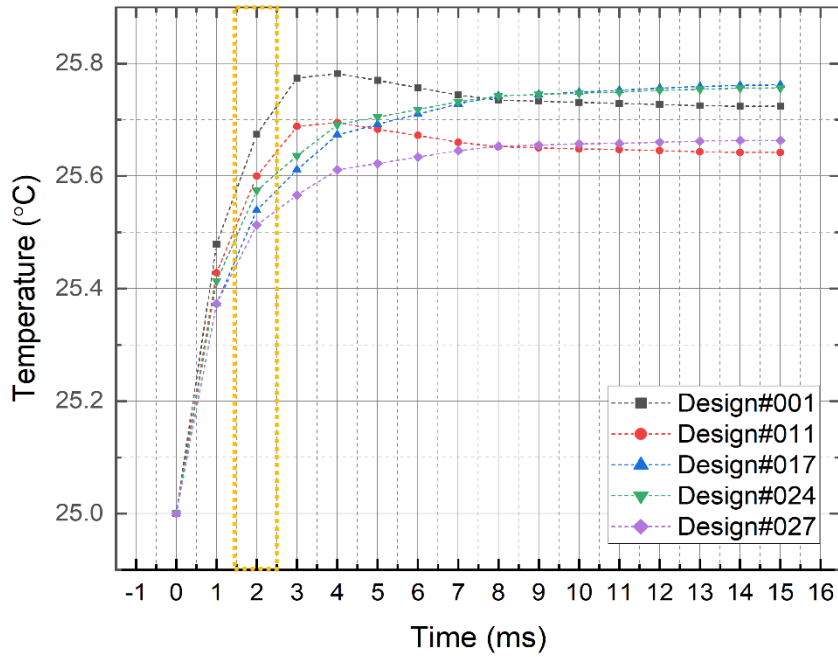
Figure 2.11: The effect of IR radiation under 15 ms exposure and different pixel designs' responses with time constant window.

By taking one of the pixel structures from **Table 2.2**, electro-thermal simulations are done with and without IR radiation, as seen in **Figure 2.12**. The pixels are referred to as an active pixel with IR radiation given onto the pixel. The reference pixel has no IR absorption; otherwise, there is no IR radiation present on this pixel. The pixel is heated by an applied electrical bias that is also called Joule heating. Both pixels faced the same parameters except that one of them is exposed to IR radiation. This radiation leads to an increase in temperature. The resistance and current change are observed because of the heat generated from the current passing over the active material and absorbed incoming IR radiation. So, this excessive temperature cause to decrease in resistance because of the negative TCR value. While performing the simulations, some parameters are taken as constant, like activation energy of the active material and absorption coefficient of the pixel body.
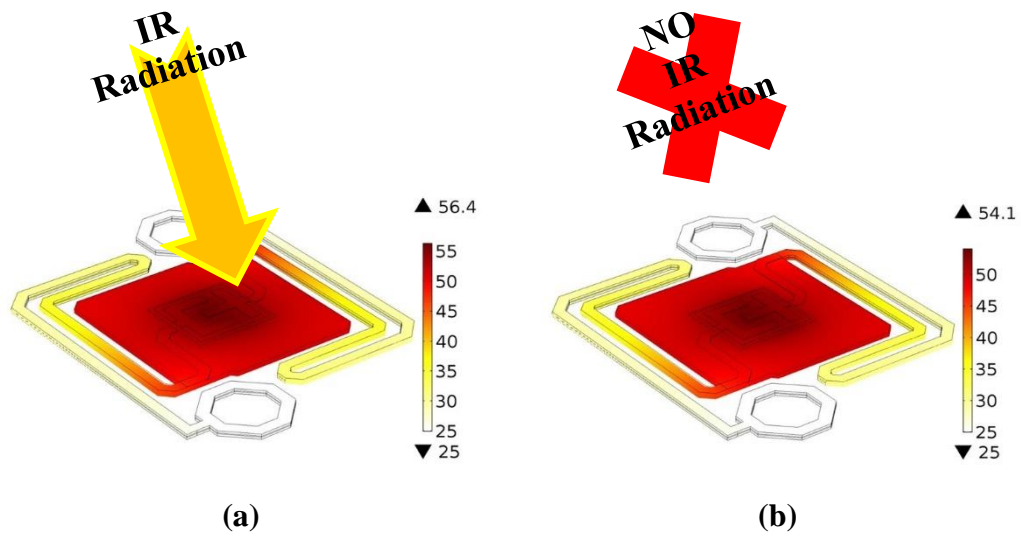
Figure 2.12: The effect of IR radiation under an applied bias on the pixels (a) with IR radiation and (b) without IR radiation differences.

The pixels are biased with voltage supply (1 V) to the reference pixel (without infrared radiation), and the active pixel (under IR radiation of 440 W/m2) is simulated. The electrical bias applied around 50 µs. The calculation is embedded into the simulation by changing the active material's TCR value. The correlation between the resistance change and the temperature is explained in Chapter 1.3.1. The active material's activation energy (E_a) is taken as a constant 0.25 eV. With these parameters, the resistance change or current change (**Figure 2.13**) is simulated, and these change in parameters helps to find the current (A/V) or voltage (V/W) responsivity.

The active pixels' current and resistance changes under applied voltage bias that bias voltage is given 1 V to the systems that is shown in the **Figure 2.13**. As mentioned before, all simulated pixels have the same 180 nm total Si_3N_4 structural layer and 50 nm NiCr arm/electrode metal thicknesses.
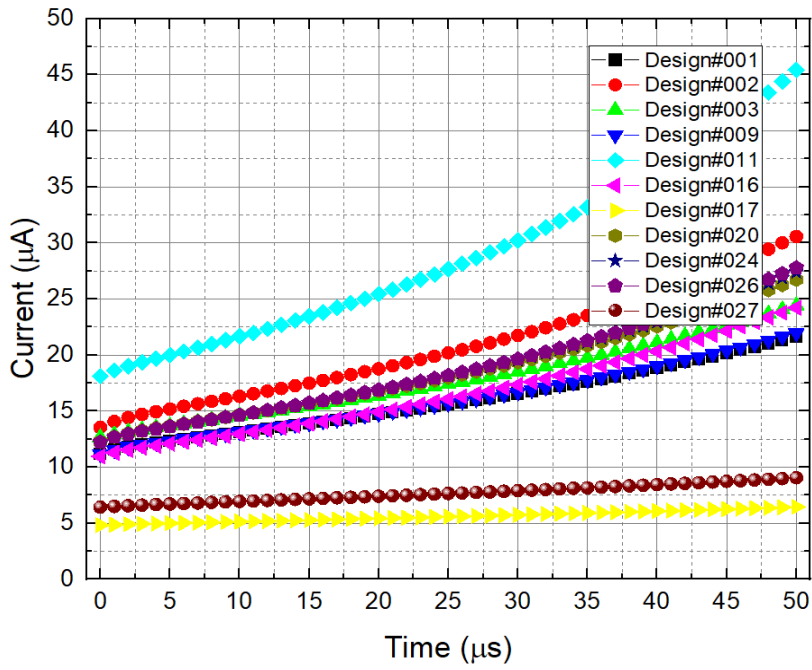
(a)
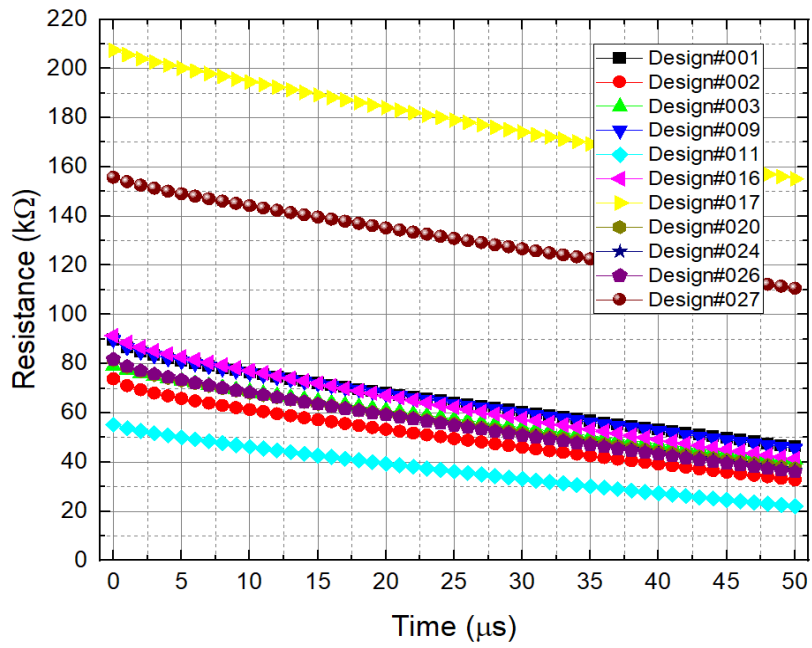
(b)

Figure 2.13: (a) Current values and (b) resistance values change of the active pixels under voltage bias (Bias voltage = 1V) with 440 W/m^2 absorbed IR power.

In simulations, the materials' properties given in Table 2.3, the electro-thermal and mechanical simulations are performed.

Table 2.3: Material properties used in the simulations [49], [55]–[57].

Material	Thermal Conductivity (W/m.K)	Thermal Capacitance (J/kg.K)	Young Modulus (GPa)	Poisson's Ratio	Thermal Expansion Coefficient (1/K)
Si_3N_4	2	700	300	0.27	2.3×10^{-6}
Active Material	5	500	80	0.42	2.6×10^{-6}
NiCr	11.3	450	22	0.3	14.2×10^{-6}

An in-depth review of pixel Design#27 is explained as an example, active and reference pixel's current and resistance difference change is given in **Figure 2.14**. With Equation (1.15, the current difference between active and reference pixel (ΔI) with respect to incoming IR power (440 W/m^2) gives a current responsivity. Some design's pixel responsivity can be found in **Table 2.4**.

(a)   (b)
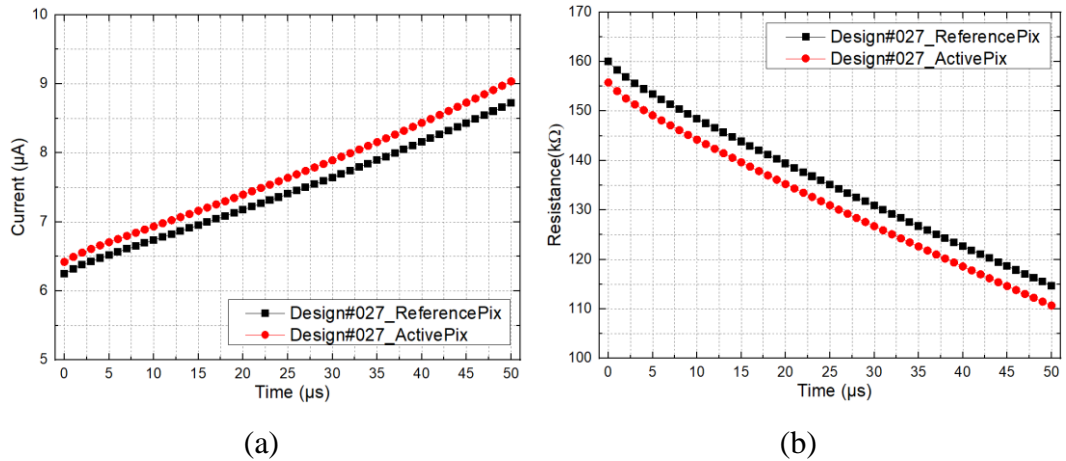
Figure 2.14: Differences between active and reference pixels (a) current values and (b) resistance values change over time.

The difference in the current or resistance of the pixel is the reason for the pixel's temperature difference. This difference causes by the absorbed IR power change to the thermal energy dissipated into the microbolometer pixel body. This converged energy causes a temperature rise. This temperature change causes a resistance drop and, eventually, an increase in current (because of the constant voltage bias).

Absorption in the larger pixel body is more than small pixel body. This absorption fill creates a more temperature rise in the pixel. All pixels have 12 µm pixel pitch. However, as seen in **Table 2.2**, pixels have a limited area to fit in pixel body and arm structures. Even heat creation in the body is more in the bigger pixel body. Heat dissipates from the body to anchor points easily because of shorter arms. So, the G_{th} becomes more critical than other parameters, which also affects the thermal time constant. Also, the mechanical stability of the pixels is considered with performance.

Table 2.4: Comparison of different pixel structures with different geometrical parameters.

Design #	Electrode Type	Electrode Width [µm]	Electrode Length [µm]	Arm Width [µm]	Arm/Body Separation [µm]	Electrode Design #	Thermal Conductance [nW/K]	Pixel Time Constant [ms]	Responsivity {{{A/V]
001	Finger	5	0.5	0.45	0.5	v1		1.9	26.5
002	Finger	6	0.5	0.45	0.5	v2		2	39.6
003	Finger	7.9	0.5	0.45	0.5	v3	45.88	1.5	28.0
004	Straight	3.75	1	0.45	0.5	v4		1.9	-
005	Finger	5	0.5	0.45	0.5	v1		1.9	-

006	Finger	5	0.5	0.45	0.5	v1			-
007	Finger	5	0.5	0.45	0.5	v1			-
008	Finger	5	0.5	0.45	0.5	v1			-
009	Finger	5	0.5	0.5	0.5	v5		2	13.2
010	Straight	3.75	1	0.5	0.5	v6	52.02	1	
011	Straight	7	0.5	0.5	0.5	v7		1	53.3
012	Finger	5	0.5	0.4	0.45	v1	41.61		-
013	Straight	3.25	1	0.4	0.45	v8		-	-
014	Finger	5	0.5	0.45	0.5	v1	45.88		-
015	Finger	5	0.5	0.5	0.5	v1	52.02		-
016	Finger	5	0.5	0.45	0.5	v1	25.84	1.5	48.4
017	Straight	3.25	1	0.45	0.5	v8			-
018	Finger	5	0.5	0.5	0.5	v1	28.71	1.8	-
019	Straight	3.25	1	0.5	0.5	v8			-
020	Finger	6	0.5	0.45	0.5	v2	34.56	~1.5	38.2
021	Straight	3.25	1	0.45	0.5	v8			-
022	Finger	6	0.5	0.5	0.5	v2	38.4		-
023	Straight	3.25	1	0.5	0.5	v8			-
024	Finger	5.5	0.5	0.45	0.5	v9	39.07	1.5	45.5
025	Straight	3.5	1	0.45	0.5	v10			-
026	Finger	5.5	0.5	0.5	0.5	v11			41.3
027	Straight	3.75	1	0.5	0.5	v6			10.0
028	Straight	4.5	1	0.5	0.5	v12	38.95	1.6-2.0	8.6
029	Straight	4.5	0.6	0.5	0.5	v12			-
030	Straight	3.75	0.6	0.5	0.5	v13			-

How the geometrical differences affected the time constant and responsivity of the pixels are shown in **Table 2.4**. These simulated structures are fabricated, and their performance is evaluated in the following chapters.

2.2.3   Mechanical Simulations of the Pixel

The mechanical simulation for design #18 is also done in COMSOL Multiphysics simulation. The reason for picking this design is that it has the longest support arms, and it is probably the most displacement observed because of the buckling effect. The parameters of the detector's materials are shown in **Table 2.3**. The initial mechanical simulation includes measuring the displacement of the pixel in the x, y, and z axes in response to a 1000g acceleration in -z- axes while the substrate remains stationary. This number is selected as a reference because it approximates the acceleration imparted to a detector fall. As seen in **Figure 2.15**, acceleration does not create a significant displacement in the pixel structure. The pixels can tolerate the external stresses due to the quick movements.
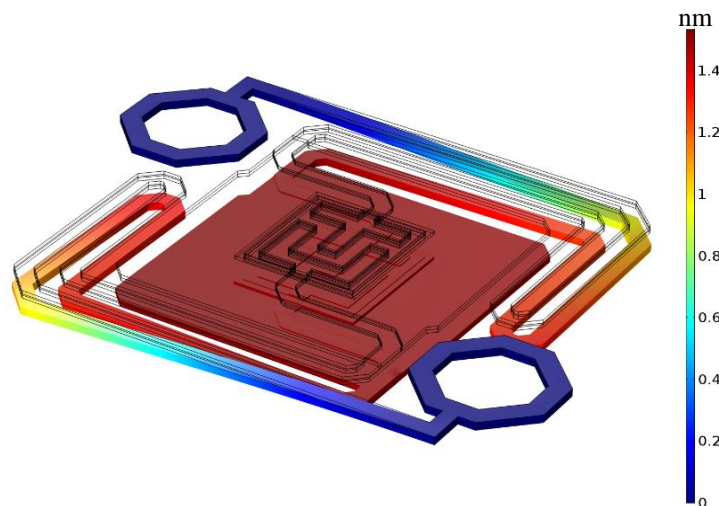
Figure 2.15: Magnitude of displacement for design #18 under 1000g applied in -z direction (the display is exaggerated).

The other type of simulation is performed for how different stress values affect the pixels [58]. Because of the process variations, the stress level on the arms may be changed. The simulation results are seen in **Figure 2.16** shows how pixel design #18 could tolerate the buckling effect on the arms. The stress on the structural layers'

differences between top and bottom nitride affects the buckling in the arm level. If the distortion on the arm structure becomes too much, this may create thermal shorts on the arm structure. The thermally short arms lead to a drop in the thermal conductance, which eventually affects the final performance of the pixel.

(a)

(b)
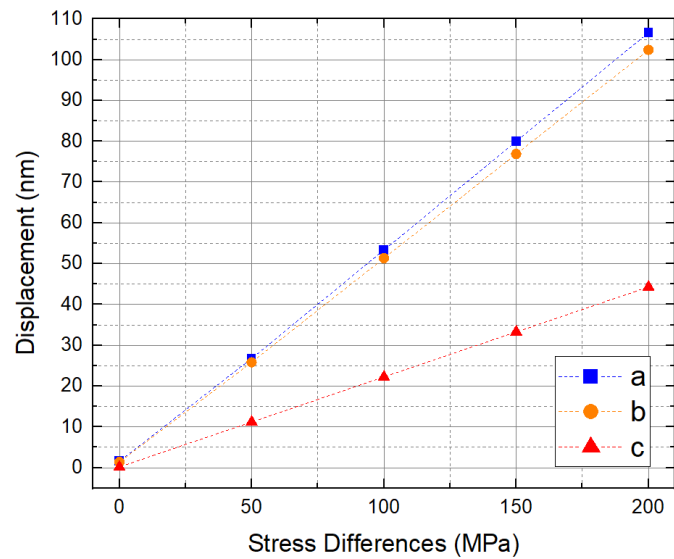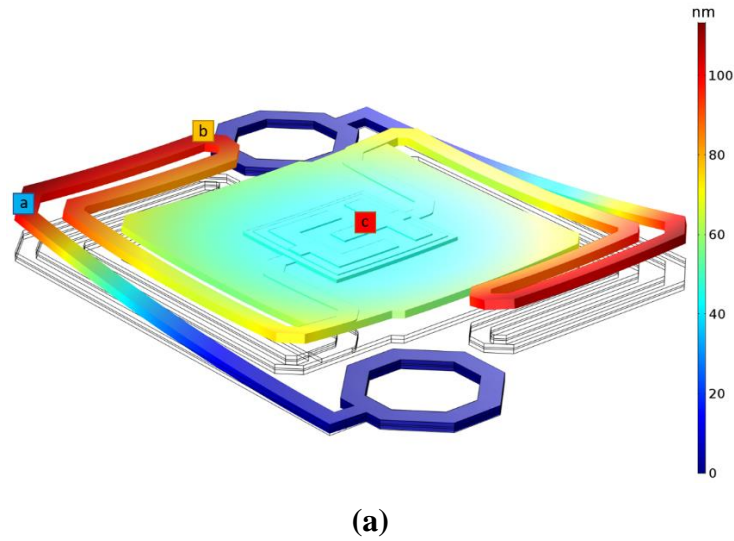
Figure 2.16: Different stress levels affect the structural layer on design #18 (a) displacement of the pixel with stress level between top and bottom is 250 Mpa (b) displacement of the different areas with stress differences between the top and bottom structural layer (the display is exaggerated).

43

This simulation aims to investigate how pixel not only stress differences affect the pixel arms and body but also pixels' behavior after the release process. As seen in the figure, the pixel body does not deflect as much as arm structures. The simulated displacement is calculated ~120-130 nm, which is less than the spacing between the structures. So, these arm deflections can be tolerated at that level. However, if these stress levels are created more than anticipated, thermally short arms will drop the thermal conductance, resulting in the pixel's performance drawback.

2.3   Conclusion

This section analyzes the design criteria and improvement process for the microbolometer pixels as well as the simulation results. The resistor structure is optimized with planar type resistor by considering using the VWOx as an active material with high TCR and considerable low noise level. Using this kind of resistive structure reduces the fabrication steps and achieves performance stability by using geometry. Besides the electrical performance, the mechanical performance of the pixels is considered. The support arms and pixel body are designed with the performance as well as the mechanical stability and strength of the pixels in perspective. The absorption simulations illustrate the impact of the thickness of the structural and sacrificial layers on the absorption characteristics of the pixel. In the end, thermal conductance and thermal time constant reduce as low as ~25.8 nW/K and ~1 ms, respectively.

CHAPTER 3

**FABRICATION PROCESSES OPTIMIZATION OF SINGLE-LAYER
MICROBOLOMETER PIXELS**

This chapter covers the optimization of the microfabrication processes of the single-layer microbolometer pixels designed into the coverage of this thesis. The designed resistive type of the microbolometer detectors' optimization is done considering CMOS compatible surface micromachining techniques. These optimizations have been applied to the CMOS readout circuit. The chapters can be summarized as Section 3.1 explains how the fabrication process is designed by giving 2-D and 3-D models of the complete fabrication steps. Section 3.2 indicates the optimization of the process steps. In the end, Section 3.3 summarizes the chapter.

3.1 Design Considerations of the Microfabrication Processes

In order to achieve desired high-performance microbolometer and getting as close as the simulation results, a well-designed fabrication process is critical. It should be considered designing the process flow in conventional MEMS microfabrication, but at the same time, fabrication facilities capabilities should be considered both design the pixels and process flows. By considering the facility's capabilities, minimum feature size, reproducibility, and uniformity on fabricated wafers after every run are critical parameters. If these conditions are not met, it will be inevitable to fail most processes/runs in the future. Even if the structures can be explained as simply as possible, many factors should not be ignored during fabrication processes.

- All process steps must be compatible with conventional CMOS fabrication process steps. Because in the long term of fabrication of these pixels, integration on CMOS wafer is the main goal to fabricate detector pixel array.

- The mirror layer serves not only to reflect the incoming radiation to the pixel body but also to serves as a metal routing to test pads that help get electrical contact for electrical testing. That is why this layer should have high electrical conductivity and high reflectivity. Along with this, if these steps are integrated into CMOS fabrication, this metal will protect/cover anchors and be carried as intermediate metal between CMOS routings and microbolometer pixels' arm/electrodes. Also, it should be resistive to releasing processes of the pixels.

- The choice of the sacrificial layer's material is crucial. It can be removed easily after the fabrication process is completed, and the removing procedure should not affect the pixel structure. Also, the thickness of the sacrificial layer must be controllable. The thickness will affect the absorption of the pixel, as mentioned previously in the simulation part. The optimum absorption values can be achieved with the thickness control of the sacrificial layer.

- The structural layer is used as support arms and pixel body. The reason for that this layer must have high mechanical stability and be stress-free to avoid buckling. Also, this layer must have a low thermal conductivity for good thermal isolation of the pixel body.

- The interconnect metal is used in arm routings and electrode structures at the same level. For desired/good pixel performance, this layer must have high electrical conductivity and low thermal conductivity.

- The active material must be optimized with a low noise level and high TCR values. Apart from these values, the resistance values can be optimized and controllable in order to compensate for the other process differences in the pixel resistance.

- The absorber metal thickness should be controllable to get desired surface resistance of the metal. Otherwise, absorption might get distorted, or peak values might be shifted.

- The surface topography during the processes should maintain a minimum.

A rough fabrication flow is developed by considering these fabrication process steps for 12 µm single-layer microbolometer pixels. Before CMOS integration, as mentioned earlier, optimization processes start on a silicon wafer. In order to mimic the surface of the CMOS structure, Silicon Nitride is coated on the silicon wafer. The fabrication steps are given in **Figure 3.1** with 3-D and 2-D perspectives to create a visual simplicity in mind.
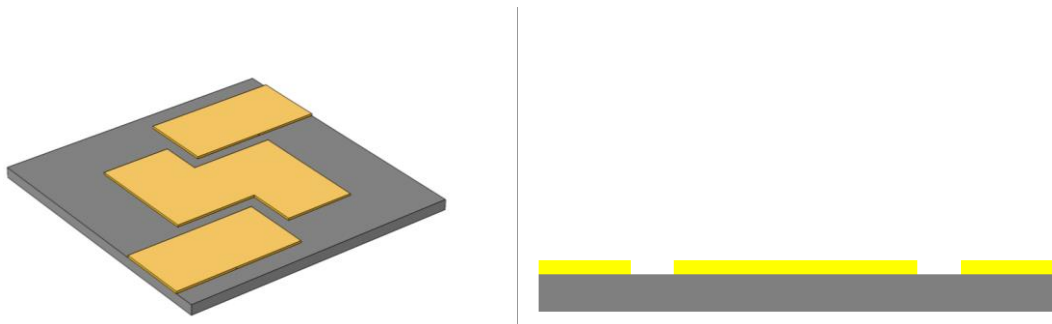
a) Deposition and patterning of the anchor points, routing, and mirror layer on top of the substrate.
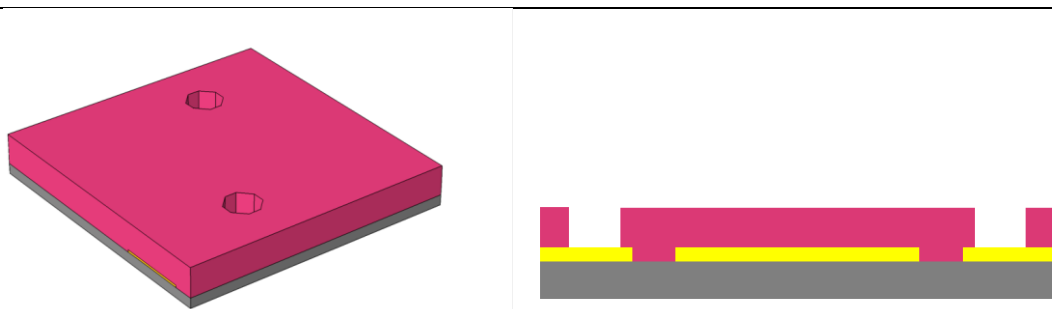
b) Deposition and patterning of the sacrificial layer.
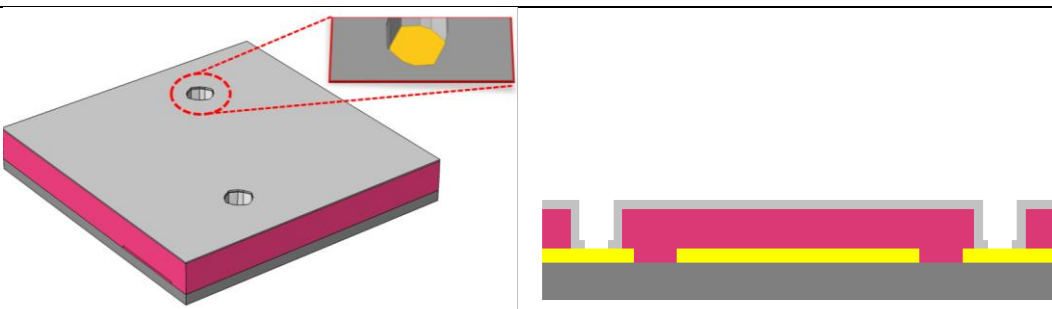
c) Deposition and patterning of the first isolation layer for arms and body.
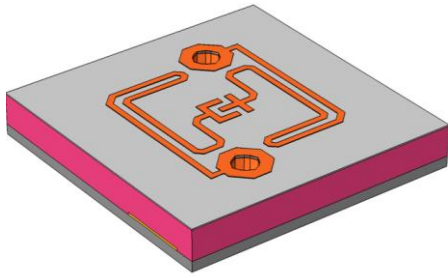
d) Deposition and patterning of the metal layer for arms and electrodes.
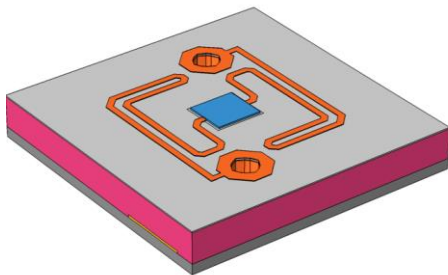
e) Deposition the active material with top electrode metal and pattern these layers together.
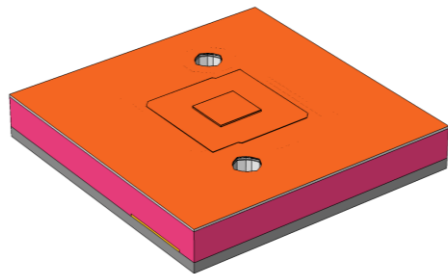
f) Deposition absorber layer with the second isolation layer.
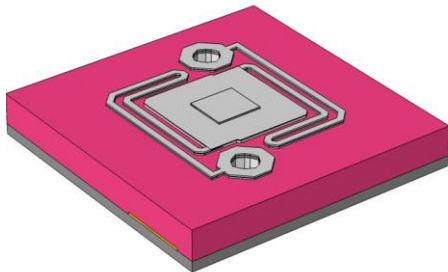
g) Deposition the third isolation layer and patterning the pixel structure.
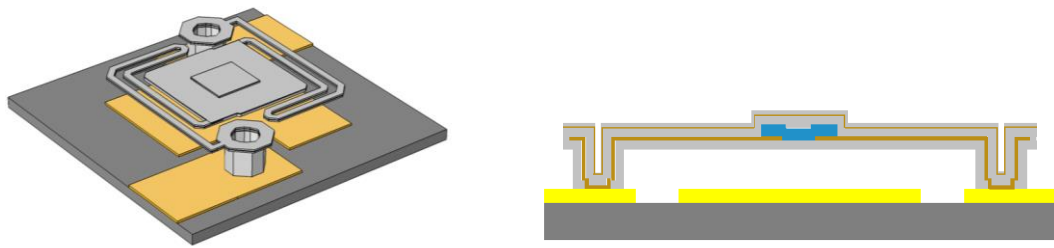
h) Releasing the pixel with removing the sacrificial layer.

Figure 3.1: Detailed representation of process flow with 3-D and 2-D perspectives.

The next chapter covers the optimization of these steps by choosing proper materials and simulated geometries.

3.2 Optimization of the Process Steps

The design of the microbolometer process steps is followed by the optimization of fabrication steps with newly designed mask sets. The masks and processes is done at METU MEMS Center. There are roughly nine different masking layers. The designed set contains lithography optimization structures, single pixels, and array structures for absorption measurements that can be seen in **Figure 3.2**. In the die layout, center squares have pixel arrays with different pixel designs, and they are used to get absorption measurements. The electrical measurements of the pixels are taken from the test pads located on all four sides of the die.
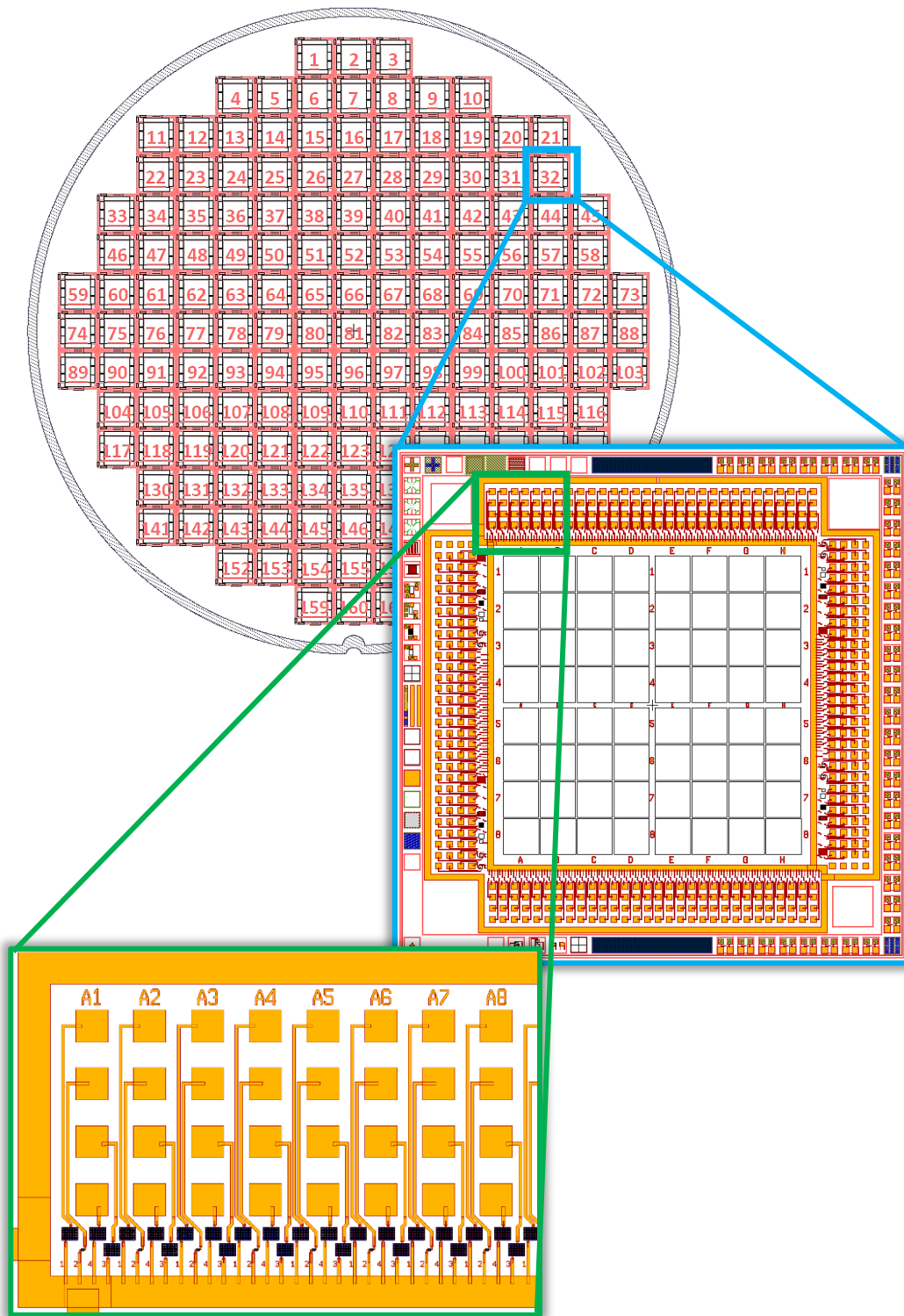
Figure 3.2: The layout of the die containing pixels, pixel arrays, test structures, and general die distribution on the test wafer.

3.2.1   Substrate Preparation

Many lithography steps are performed sequentially in microfabrication processes. At each step, different patterns of pixel geometry are created on the wafer surface. These patterns need to be properly and precisely aligned with respect to each other in each lithography step. Otherwise, the patterns will be disconnected from each other, and the pixel structure will deteriorate as the microfabrication process progresses. At each lithography step, the pattern is aligned with these alignment marks. In this way, the alignment of the patterns with respect to each other is achieved.
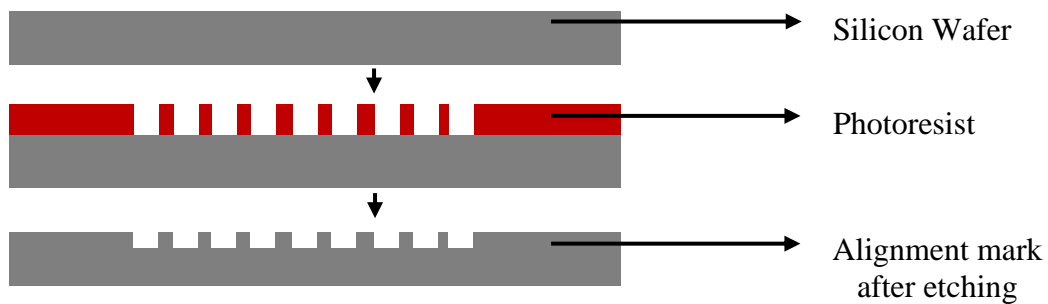
Figure 3.3: 2-D perspective of marker process on the silicon wafer.

The creation of alignment marks is shown schematically in **Figure 3.3**. These patterns result from the etching of the silicon substrate. Patterning is done with SPR220-3 photoresist, which can be seen in **Figure 3.4**. Etched performed with RIE plasma dry etching technique that Fluorine-containing gases are used. This part is intentionally buried on the silicon substrate because the following processes will not affect these structures. After these processes, in order to mimic the CMOS surface, the passivation nitride layer is coated.
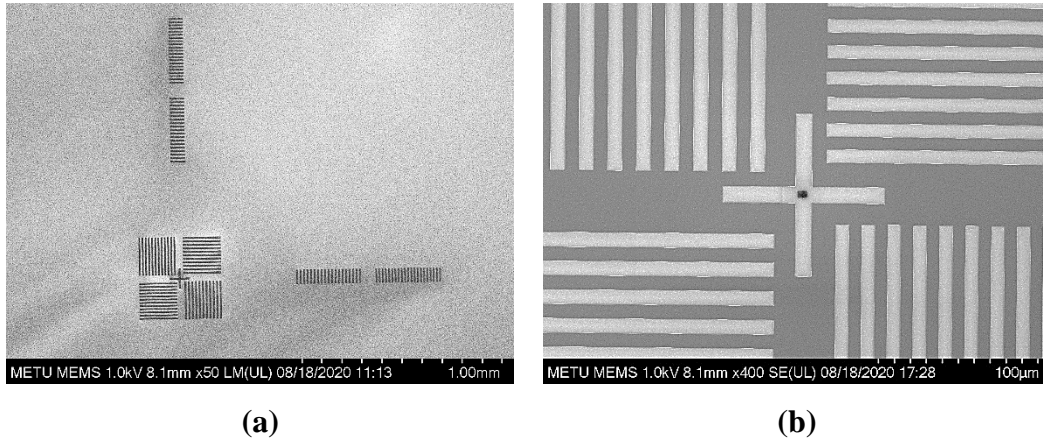
Figure 3.4: SEM images of the alignment mark after (a) lithography and (b) etch.

3.2.2 Mirror Layer and Pad Structures

The mirror layer is used as a reflective structure. Incident IR passes through the pixel body, which absorbs a significant amount of the light and is reflected from the mirror layer, and the reflected IR radiation is absorbed again at the pixel body. This layer and pixel body correlated with each other and creates a cavity that multiple reflections and absorption happen in between these layers. So, the mirror layer helps to increase the absorption of the incoming IR radiation. That is why this layer should be highly reflective.

Substrate	Photoresist	Mirror	Nitride
Metal	Active Material		Polyimide
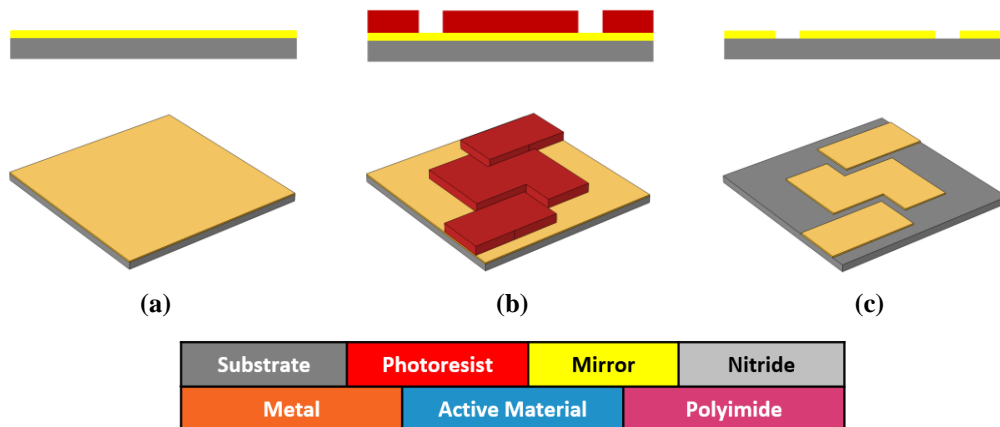
Figure 3.5: 2-D and 3-D perspective of mirror layer structure formation after (a) deposition, (b) lithography, and (c) etch.

Apart from the reflectivity of the mirror layer, high conductivity and not effected by process steps are the other concerns. There are a couple of alternatives for this layer, like titanium, aluminum, nickel-chromium, and gold. Unlike gold, other materials will be affected by process steps. Such as nickel-chromium and titanium, which are used in the interconnection between anchors and arms, might get affected if the interconnect arm metal needs to be stripped multiple times. Also, they will be affected during pixel release, which will be mentioned in **Section 3.2.8**. Otherwise, the gold layer is a very stable and highly conductive metal studied before at METU MEMS CENTER [49], [59]. It will not be affected by etching gases during the release of the pixels, and high reflectivity helps transmit electrical data from pixel anchors to test pads. Nevertheless, even if gold has good specs, it has poor adhesion with the passivated substrate. To overcome this situation, TiW alloy is used between gold and substrate. From this point, TiW/Au stack is mentioned as a mirror layer.

| (a) | (b) | (c) |
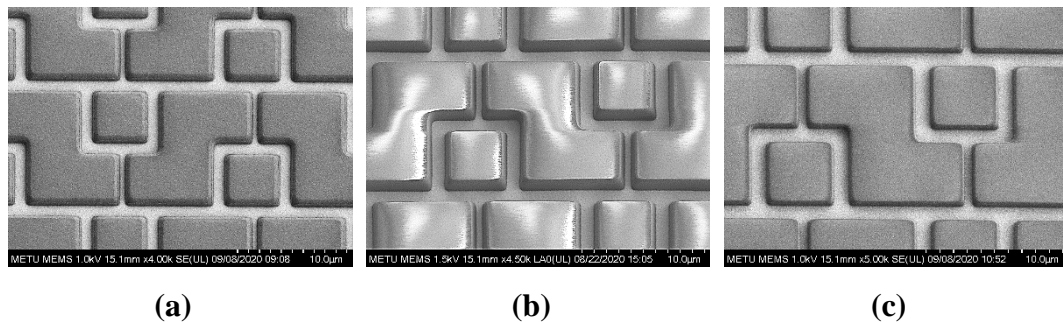
Figure 3.6: SEM images after the photoresist trials on mirror layer with best possible results (a) s1805, (b) s1813, and (c) u-i photoresist

As shown in **Figure 3.5.(b)**, the lithography step in the mirror layer is critical. Different resists with different parameters were tried to achieve the best possible results shown in **Figure 3.9**. The anchor should be separated/isolated from each other. Because it is more controllable between its coating thickness, exposure energy, and resist wall profile, u-i positive photoresist was used in the mirror layer

lithography step. Otherwise, it will be electrical short, and trusted measurement cannot be achieved. This situation is exemplified in **Figure 3.7**.
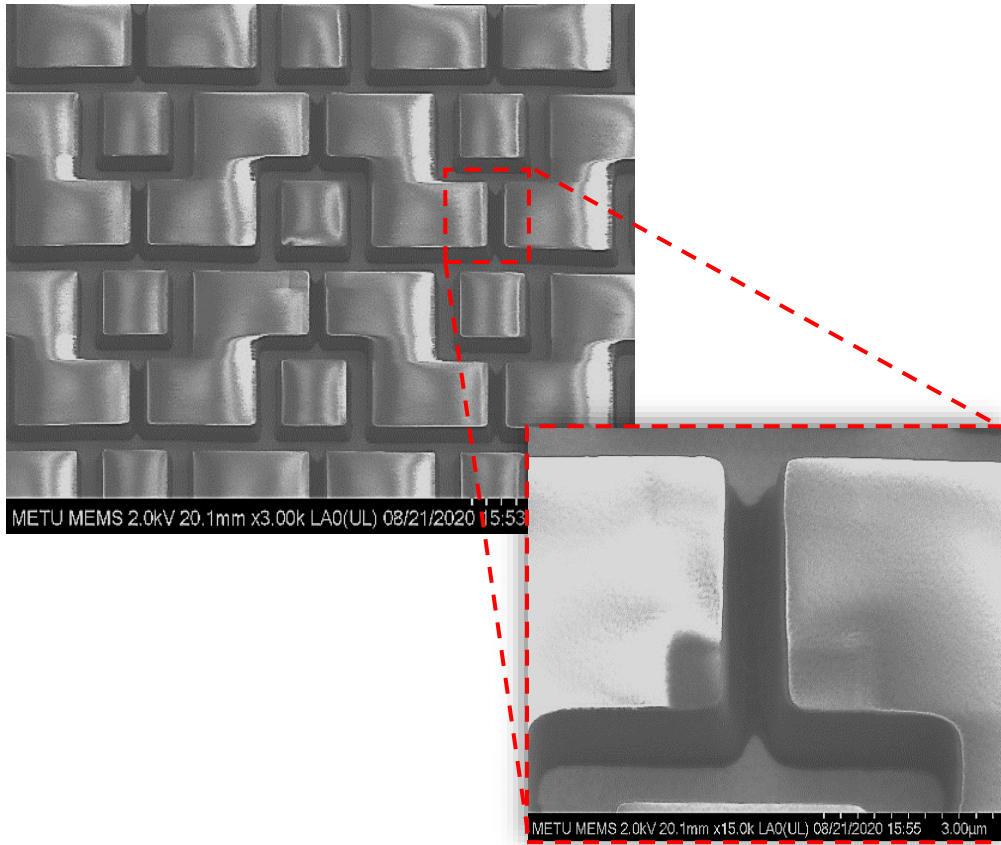
Figure 3.7: SEM images after photoresist optimization with s1813 photoresist.

Etching of the mirror layer is performed with diluted Aqua-Regia solution. The solution is a 2:1 mixture of $HCl:HNO_3$ diluted with different amounts of water [60]. Because etch rate of the solution is too high, the water amount can be increased to lower the rate. Also, it is concerned that the solution etches rate will degrade over time, and etch profile will also be affected. **Figure 3.8** shows the successfully patterned TiW/Au mirror layer of the pixel array and test pixels routings.
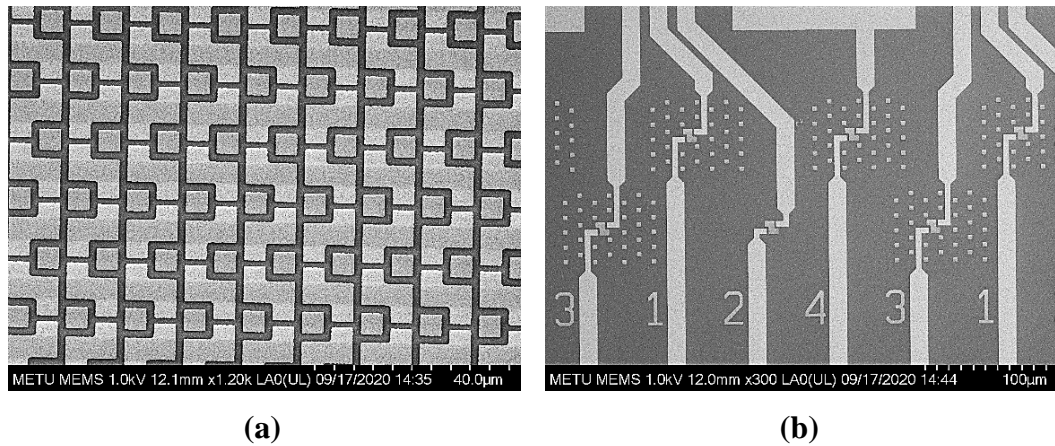
Figure 3.8: SEM images after mirror layer (a) pixel array and (b) test pixels with their routings.

3.2.3 Sacrificial Layer

The sacrificial layer's choice is one of the main concerns because of the compatibility of the fabrication of the pixel. This layer should not be affected by regular fabrication processes, and it should be removed easily, which will be removed after the pixel structure is completed. Polyimide was previously studied as a sacrificial layer at METU MEMS CENTER [35], [53]. This material can be easily removed under O_2 plasma without creating any defect on the pixels. Because removing this layer with wet releasing will cause pixel collapse onto the substrate under the effect of capillary force. **Figure 3.9** shows the sacrificial layer formation.

The other concern is the thickness control of this layer. The determined thickness of the sacrificial layer from absorption simulation should be achieved. The previously studied polyimide can be coated with a spin-coating method. For the single-layer microbolometer design, approximately 2.2 µm sacrificial layer should be coated. As a polyimide, PI2610 is spin-coated at ~2400rpm for desired thickness, taken as a reference point from the material datasheet. After coating, in order to cure the layer, the wafer heated and cooled at ~300 °C, gradually.
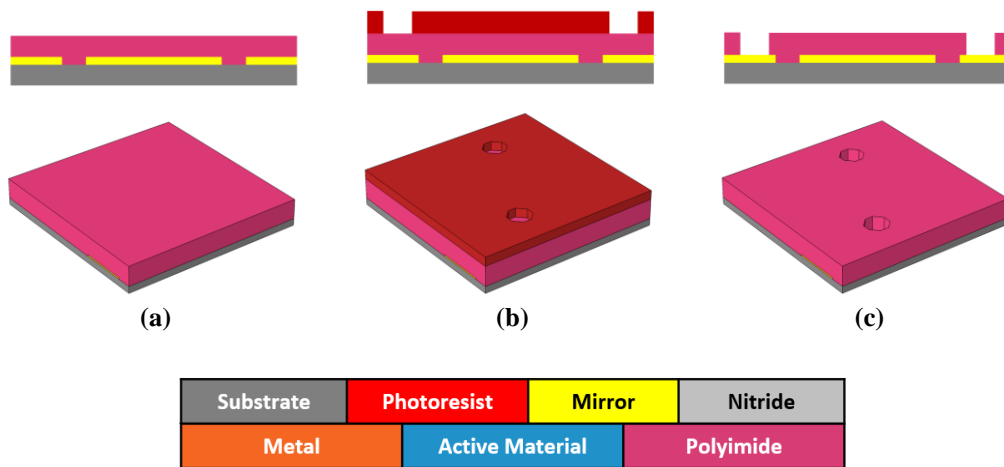
Figure 3.9: 2-D and 3-D perspective of sacrificial layer formation after (a) spin-coating, (b) lithography, and (c) etch.
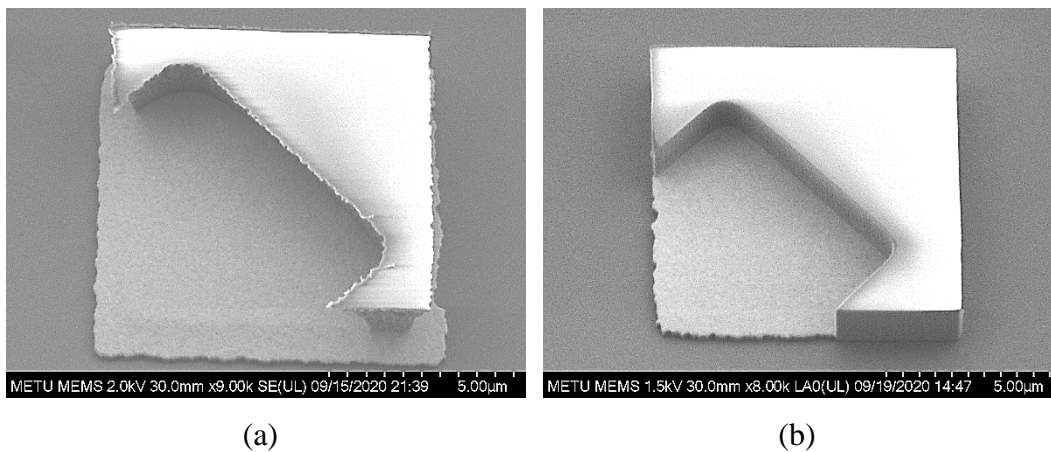
Figure 3.10: SEM images after sacrificial layer etch with (a) over-etch walls and (b) straight walls.

The anchor walls should have relatively low angles to create high aspect ratio trenches as an anchor point of the pixels. PI2610 should be coated uniformly to meet this condition, and etching should not create angles through the wafer. If these conditions are not met, the following interconnect metal coating would be split with bottom metal. The etching method is chosen as dry etching with an RIE device for

directional etching by using O2 plasma. **Figure 3.10.(a)** shows polyimide etching performed with a silicon nitride hard mask and the walls over-etched. Otherwise, **Figure 3.10.(b)** shows that polyimide walls can be created, and this etching is performed with a photoresist. The second difference with these etching profiles is plasma creation in the RIE [61], [62]. The platen and coil RF plasma are used for over-etched wall profiles, but the desired etch profiles are achieved with only platen RF plasma. Using platen RF plasma while etching the polyimide helps achieve the desired anchor etching profile and dimensions of anchor openings, which can be seen in **Figure 3.11**.

METU MEMS 1.5kV 30.0mm x30.0k LA0(UL) 09/18/2020 21:59   1.00μm
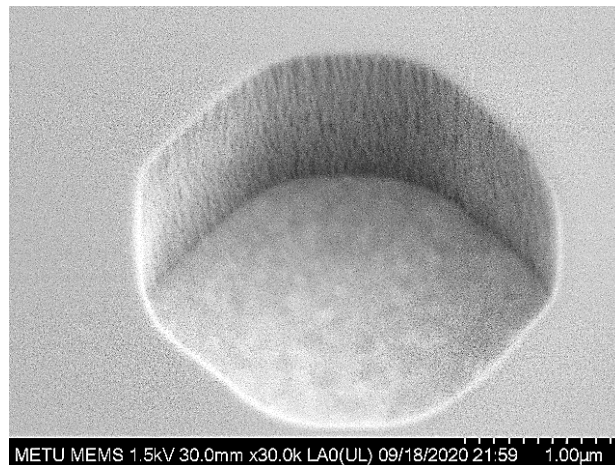
Figure 3.11: SEM image of the anchor point after PI2610 etching with plasma etch.

3.2.4   Structural Layer and Anchor Contact Opening

The following of the opening polyimide sacrificial layer, pixel structural layer are formed as silicon nitride (Si_3N_4). Because of its low thermal conductivity and the creation of stress-free films at METU MEMS CENTER, it is an excellent option to form pixel body and arms structure with silicon nitride. Having stress on the structural layer creates a buckling in the pixels. This buckling effect may cause a thermal short between arms or pixels body contact with the substrate.
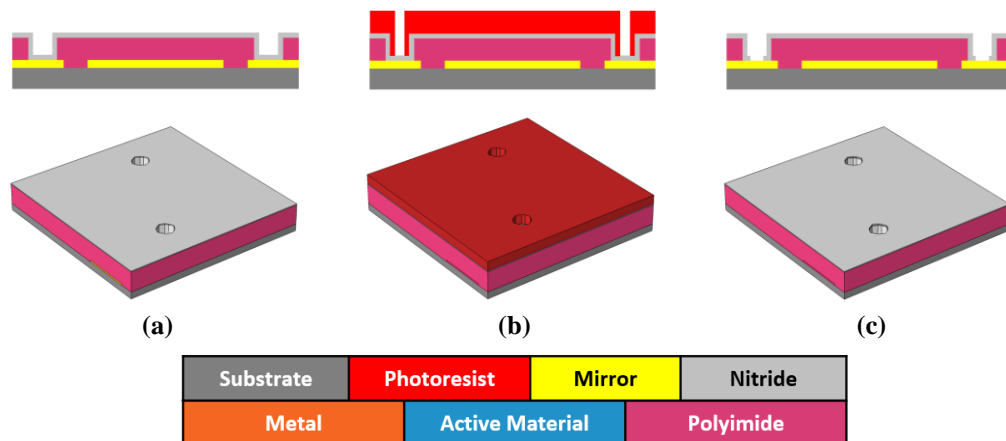
Figure 3.12: 2-D and 3-D perspective of the structural layer with opening after (a) deposition, (b) lithography, and (c) etch.

Figure 3.12 shows the anchor opening steps with deposition of the structure layer. After stress-free structural layer deposition, which covers anchor metal, the anchor points need to be opened for electrical contact between anchor metals and interconnect metals. Unsuccessful or deformed lithography inside the anchor may cause etching of the sidewalls of the anchors that will affect the next steps. On the other hand, as shown in **Figure 3.13**, the open/close area ratio is enough to obtain the structural integrity of the anchor walls.

(a)   (b)
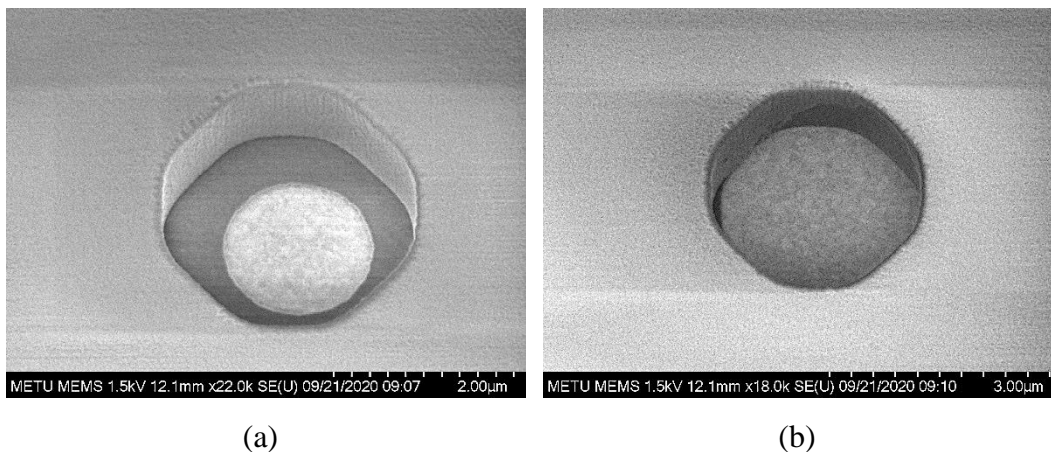
Figure 3.13: SEM image of the anchor point after etching (a) successful and (b) un-successful/deformed anchor openings.

58

3.2.5 Interconnect Metal and Electrode

Thermal conductance is a critical parameter while considering the highly responsive and low NETD of the microbolometer fabrication. Like structural layers, interconnect metal should have low thermal conductance. Also, it should have high electrical conductivity. With these specs, pixels can be isolated from the substrate very well, which helps hold the body's heat. **Figure 3.14.(c)** shows that longer support arms containing structural layers and interconnect metal with low thermal conductance create better isolation of the pixels. Apart from this design in the figure, different support arm lengths, widths, electrode structures are also designed and fabricated.

(a)	(b)	(c)

Substrate	Photoresist	Mirror	Nitride
Metal	Active Material		Polyimide
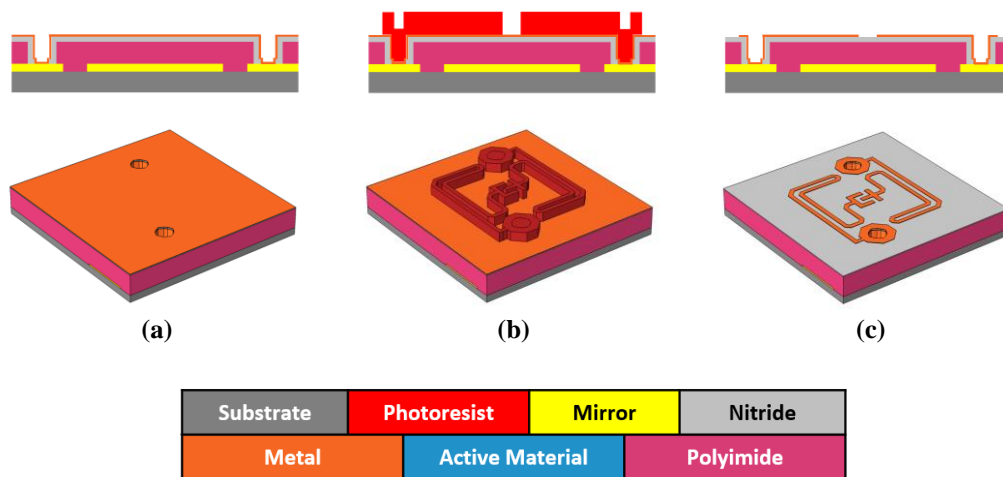
Figure 3.14: 2-D and 3-D perspective of the metal layer formation after (a) deposition, (b) lithography, and (c) etch.

Some metals and metal alloys can be used as an interconnect metal layer like Au, Al, Cr, Ti, NiCr. As seen in **Table 3.1**, NiCr and Ti are the best options among these metals. Also, this was previously studied at METU MEMS CENTER[49]. NiCr deposited with PVD sputtering method is selected as an arm/electrode metal by taking these studies and its low thermal conductivity and relatively good electrical resistivity.

Table 3.1: Thermal Conductivity and Electrical Conductivity of some metals and alloys that are compatible with microfabrication [49], [55], [56].

	Au	*Pt*	*Al*	*Ti*	*NiCr*
Thermal Conductivity (W/m.K)	320	71.6	237	21.9	11.3
Electrical Conductivity (S/m)	45.6×10^6	8.9×10^6	35.5×10^6	2.6×10^6	0.8×10^6

Many pixel designs pixels' geometries are given in **Table 2.4** in the ongoing fabrication that have different arm widths, lengths, and electrode structures. The minimum feature size that capable of the METU MEMS FACILITY is also be considered. These designs are assigned into different pad structures, which are shown in **Figure 3.2**. Because multiple geometrical differences locate on the dies, each should be considered differently. Arm widths vary after lithography among the periodic/dense arm structures, as seen in **Figure 3.15**. These differences act directly on the thermal conductance of the pixels and finally affects the NETD values.

(a)   (b)

(c)   **(d)**
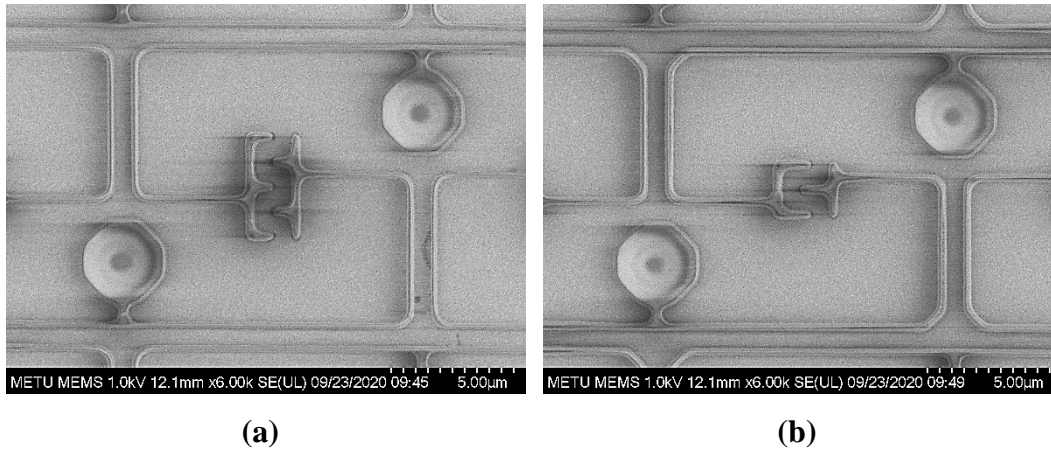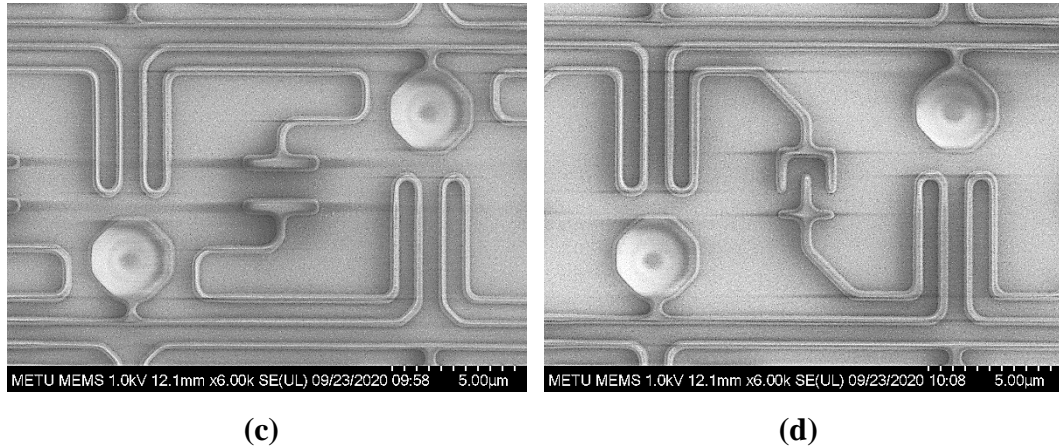
Figure 3.15: SEM pictures after lithography optimization for different arm lengths and electrode formations.

Apart from their electrical and thermal performance, compatibility of the fabrication processes is also considered and the structures lithography performance. Etching performance and methods have a significant role in the fabrication of the pixels. The etching method should be compatible with the CMOS fabrication process, and it should not affect other processed layers. Wet or dry etching methods can be applied for arm/electrode metal etching. Both have advantages and disadvantages against each other. Multiple wafer processing and etch selectivity between layers are the most significant advantages of the wet etching method. However, because of the isotropic etching profile of the wet etching technique, undercut of the metal etching is highly possible. If the etch time and etch directionality cannot be controlled, over-etching is observed, creating a breaking off on the metal layer. Raptured metal cannot conduct the electrical signal, and the pixel is considered as dead-pixel. The pixels' arm/electrode metal is thin, and they have a relatively small width. Because wet etching generally creates an undercut, and most pixel structures are unable to be used. In order to eliminate these effects, the dry etching method is used to etch the metal. Because of the anisotropic etch profile, dry etching does not create an undercut, helping to create a relatively narrow arm width. Besides etch profile, dry etching has some disadvantages. Etching can only perform one wafer at a time. High

cost and selectivity are lower than wet etching. In this thesis, the dry etching method is used because low aspect-ratio arm structures are wanted to be created. Etching performed at ICP-RIE with Cl_2 gas has a low selectivity against the photoresist because of the Ar^+ bombardment. That's why a long etching time is not suitable for covering the metal only with a photoresist. If resist does not stand during etching, the metal layer is completely etched, and electrical contact is lost, as seen in **Figure 3.16**.**(a)**. The used NiCr arm metal structure is also covered with Ti as a hard mask. At first, Ti hard mask and NiCr metal layer are etched. After successfully etching the arm/electrode metal layer that shown in **Figure 3.16**.**(b)**, Ti hard mask is stripped with a 4:1 mixture of 30% hydrogen peroxide and %28-30 ammonia solution.

(a)   (b)
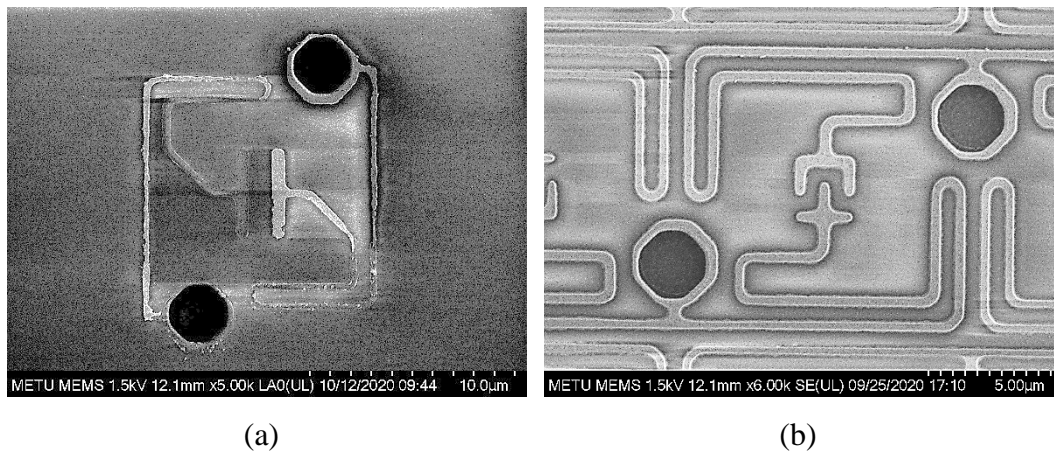
Figure 3.16: SEM images after arm metal/electrode etching (a) deformed etch profile and (b) successful etch profile.

3.2.6   Active Material

After metal layer etching also contains electrode structures, the lithography step is fallowing because coated active material will be shaped with lift-off technique.

AZ5214E photoresist is used with image reversal technique to create the photoresist structure with no resist present on the electrodes, as seen in the **Figure 3.17**. At first, the coated resist is exposed, and the wafer is baked. During the baking step for image

reversal after exposure, the exposed areas of the resist lose their ability to develop, while the unexposed areas remain photoactive. After that, the wafer is exposed to UV again that called flood exposure. Then, the developed resist is created resist walls with an angle. This angle eases the lift-off process to unwanted layer stacks removed from the surface.

Substrate	Photoresist	Mirror	Nitride
Metal	Active Material		Polyimide
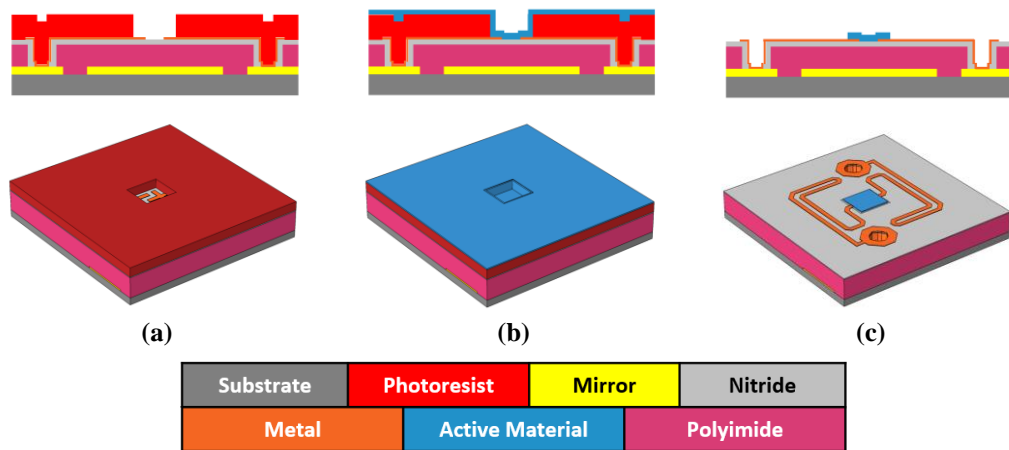
Figure 3.17: 2-D and 3-D perspective of the active material formation after (a) lithography, (b) deposition, and (c) lift-off.

After the lithography step is completed, resistive film, as active material, is coated. Tungsten-doped vanadium oxide (VWOx) film is deposited with the DC magnetron co-sputtering deposition technique as a resistive film. Targets are separated from each other, and oxygen is filled externally inside the chamber. Many materials are used as a resistive film in microbolometer fabrication like a-Si, YBCO, etc. [32], [34]. This VWO_x film changes its resistance by tuning oxygen, vanadium, and tungsten concentration. As explained in [59], all three material's concentrations also affect the TCR values. While the tungsten concentration increases by increasing the sputter target's power, the resistance value should increase. As well as resistivity change, TCR values are increased apart from the noise values. The resistance measuring from the pad structure that formed at the mirror layer structure is performed.

3.2.7 Absorber Layer and Pixel Body/Arm Structure

After coating the active material, a second structural nitride is deposited as a passivation layer. Then, very thin NiCr as an absorber layer, and third structural nitride is deposited on the surface, like seen in **Figure 3.18**. These silicon nitride passivation layers' total thickness is the same as the previously deposited nitride layer. The reason for the matching thicknesses is to eliminate layers' stress. Otherwise, mismatched stress levels might create a buckling on the arm structure. Also, direct O_2 plasma exposure (during the release process) damages the thin NiCr layer and degrades the performance.
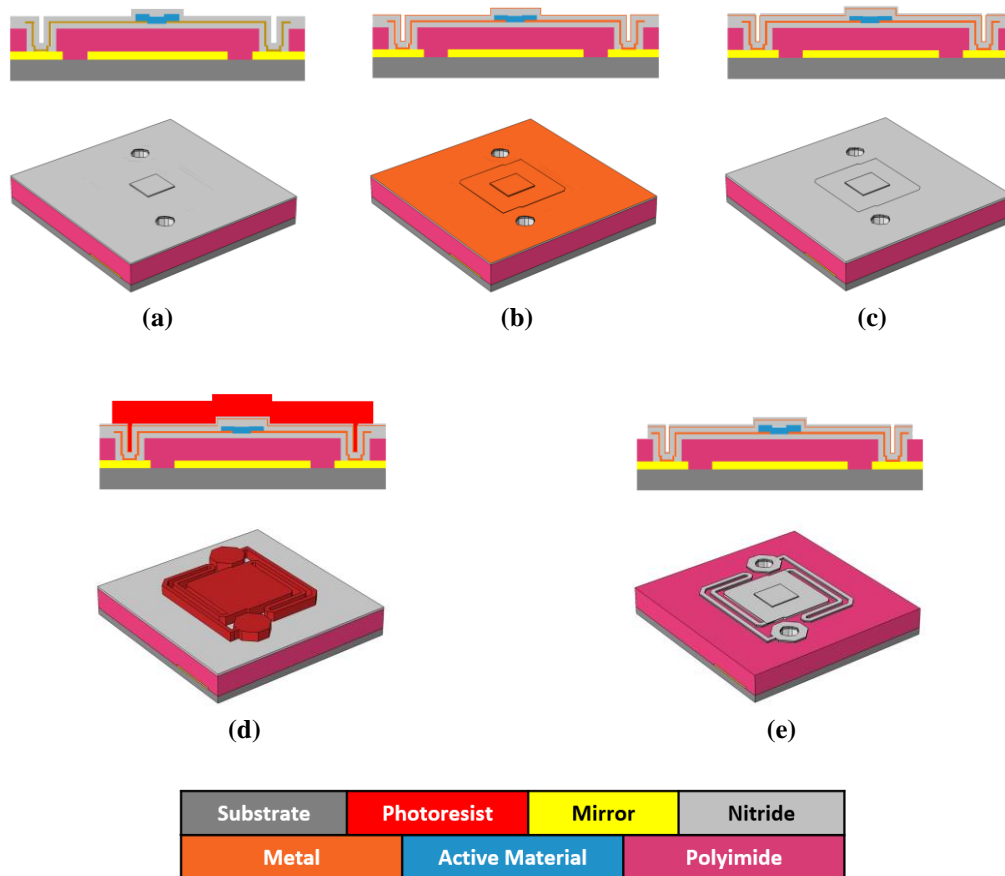
Figure 3.18: 2-D and 3-D perspective of the constructing structural layers, absorber layer, and pixel arm/body structure (a) 2nd structural layer deposition, (b) absorber layer deposition, (c) 3rd structural layer deposition, (d) lithography, and (e) etch.

NiCr thickness as an absorber layer was previously optimized at METU MEMS Center by Ramazan Çetin [53]. The maximum absorption value is reached at 377 $\Omega/\square$ sheet resistance. By the light of this simulated and fabricated data, the thickness is optimized (~5 nm) for the best possible absorption with minimum thickness [63]. Deposition of thin absorber metal is also minimizing the pixel heat capacity, which reduces the pixel thermal time constant. The other advantage of this layer, it can be etched with the pixel body.

The last step before releasing the pixel body is pixel body formation. Because the pixels' arm structures are very small feature size around 0.5 µm. The resist that covers these feature sizes should be used. In order to achieve this, u-i or Fujifilm 0IR 620 photoresist can be used. Both resists can be achieved with this feature size. However, both resists' sizes on arm width are diminished after etching. These are shrinking in the arms on top nitride can be ignored. At the same time, while etching the features, the metal layer is masking the bottom structural silicon nitride. This resulting that there is no size decrease in this nitride layer. However, the metal layer's geometrical features determine the bottom nitride geometries. The reason for this effect is using the dry etching of the arm/body nitride by using RIE method.

(a)   (b)
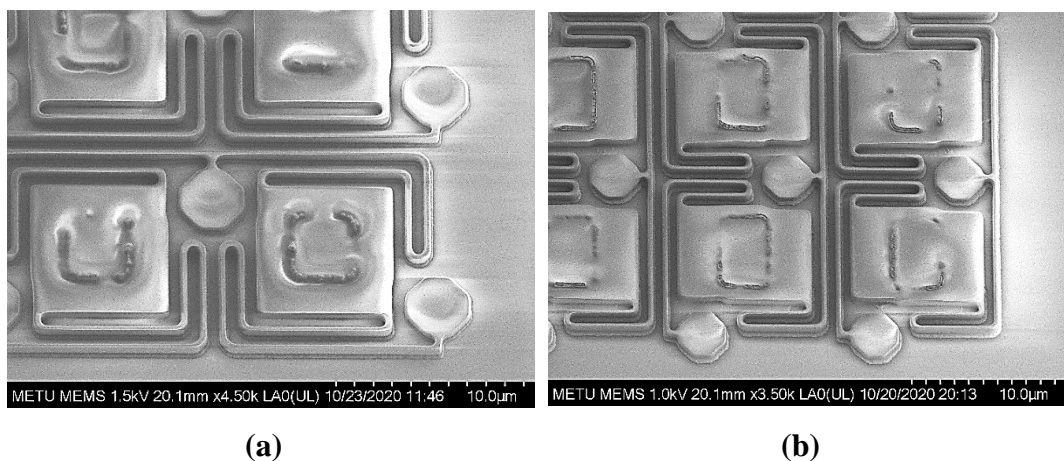
Figure 3.19: SEM images of lithography (a) Design #18 and (b) Design #27.

3.2.8 Pixel Release

The last step of the microfabrication for the microbolometer pixel is releasing the pixel geometry. The sacrificial layer is etched with O_2 plasma.

Substrate	Photoresist	Mirror	Nitride
Metal	Active Material		Polyimide
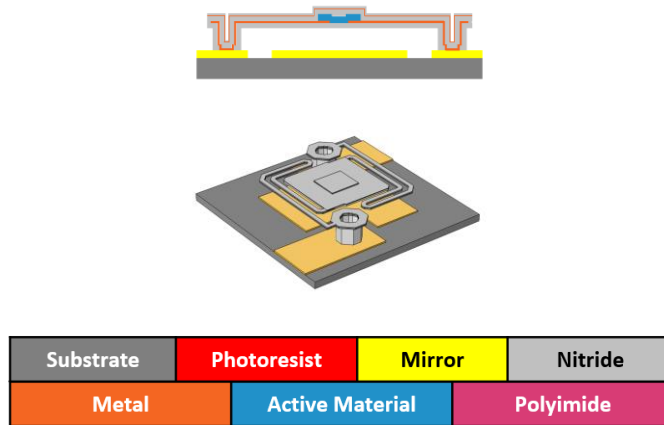
Figure 3.20: 2-D and 3-D perspective of the released pixel structure.

The major problem while releasing the pixel by removing the sacrificial layer is the buckling problem. Especially, the corners of the arms are intended to lean an over etched nitride structure. The reason is the unevenly distributed stress level on the arms, like seen in **Figure 3.21**. This effect is simulated that as seen in **Figure 2.16**.

The lift-off process causes the wall of the active materials in **Figure 3.21**. The resist walls should have less than 90° angle. Otherwise, these walls are observed, as seen in the figure. The corrected structure for the not buckled and no walls at the active materials can be seen in **Figure 3.22**. The bucking and walls around active material may affect the performance of the pixels.
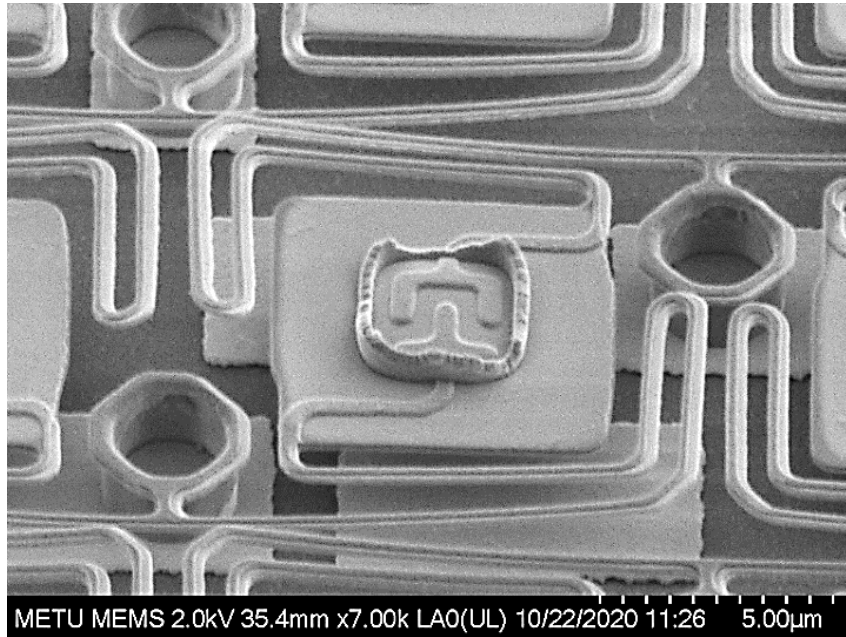
Figure 3.21: SEM image of **"Design #18"** from wafer #6 after the release process.
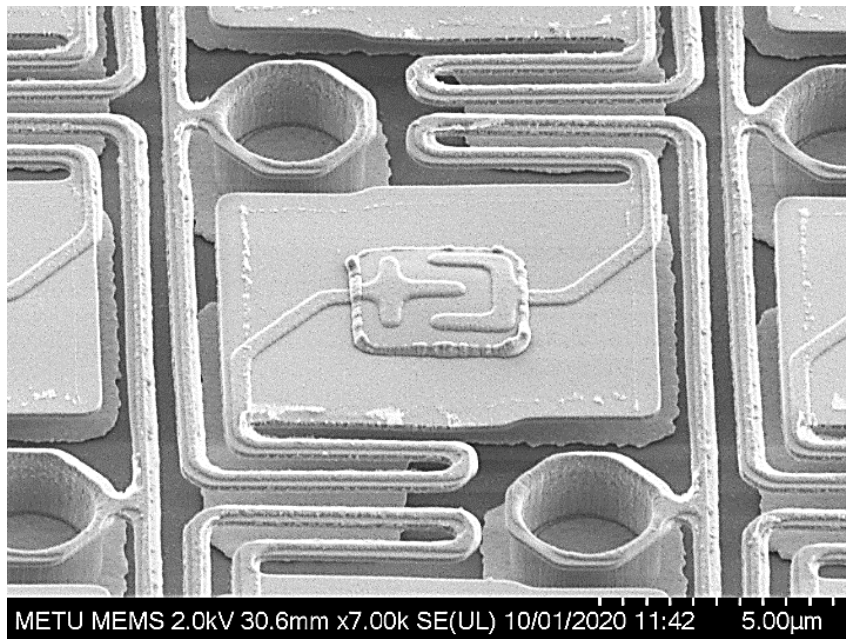
Figure 3.22: SEM images of **"Design #18"** of the wafer #5 with 12 µm pixel pitch.
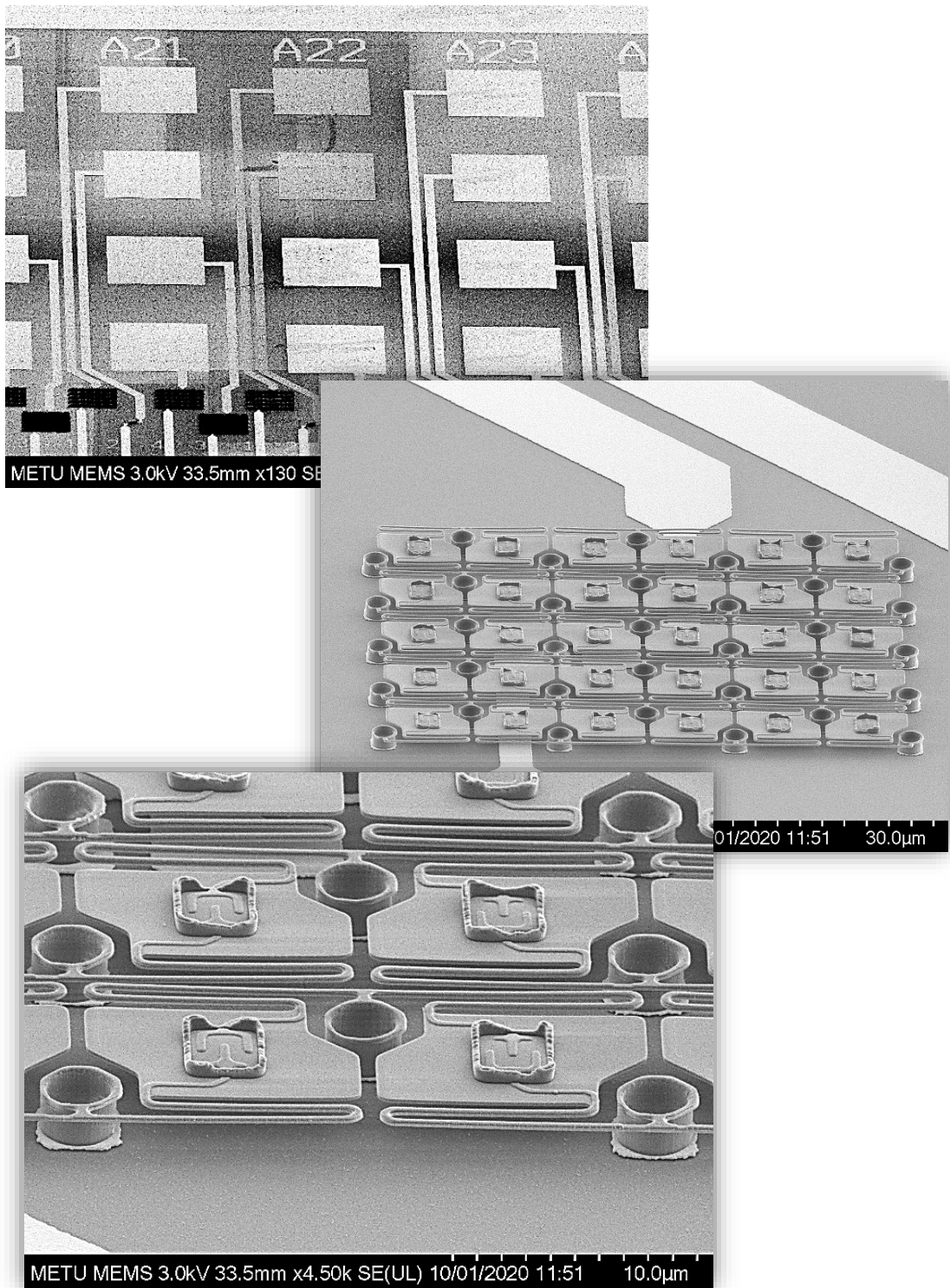
Figure 3.23: SEM images of pad structures and **"Design #22"** after successfully suspended pixel array and pixel structure inside the array from wafer #5.

3.3   Conclusion

This chapter discusses how to build the structure for the process flow for the suggested pixel structures and how to optimize each process step separately. All fabrication stages are designed as CMOS compatible, allowing the pixels to be produced on Field-Programmable-Arrays (FPAs). Construction and suspension of the structured pixels have been completed successfully. The findings of the tests performed to characterize these pixels are presented in the next chapter.

CHAPTER 4

TEST RESULTS

This chapter presents the experimental findings for the developed microbolometers and compares them to the performance characteristics anticipated by simulations. Section 4.1 summarizes the findings of TCR measurements on improved sandwich resistors. Section 4.2 summarizes the findings of the resistors' noise measurement experiments. Section 4.3 details the thermal conductance experiments performed on the microbolometer pixels and the findings obtained. The results of the responsivity measurement tests are shown in Section 4.5. The results of applying one of the designed microbolometers to an FPA are shown in Section 4.6. Finally, section 4.7 summarizes the chapter's test and measurement findings.

4.1   TCR Measurements

After fabrication of the test pixels, the pixel structures did not suspend to not affect from the temperature fluctuation over the pixels. Suspended pixels tend to keep the heat on the body, which might mislead the measurement of TCR values. Keeping the sacrificial layer under the pixel body distributes heat over the layers, and it does not create a temperature fluctuation over the pixel.

Multiple measurements are taken for the pixel resistance because there are ~30 different pixel structures. The measurements are taken from the pad structures, which are seen in **Figure 3.2** and **Figure 3.23** at the 2-probe station. The resistance distribution over the pixel structures is given in **Figure 4.1** and **Figure 4.2**.
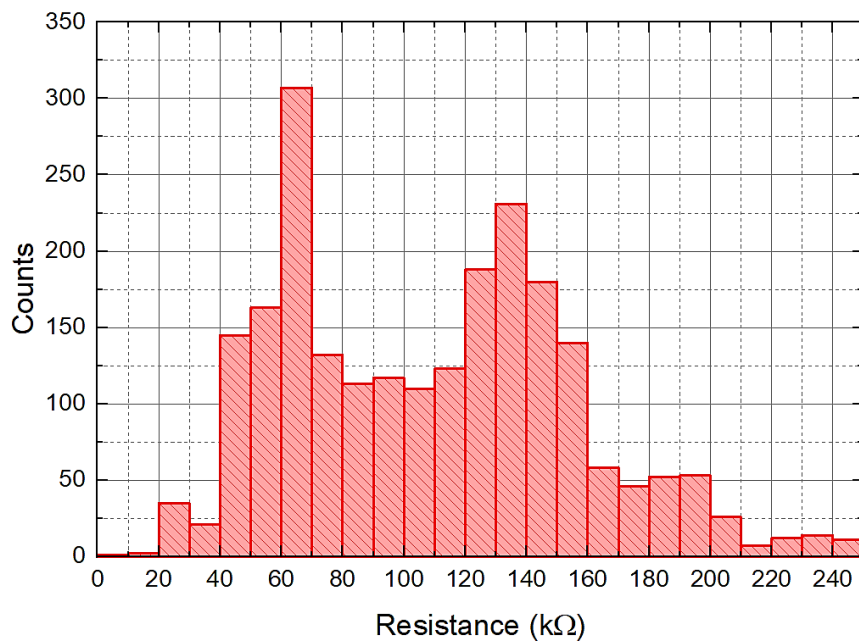
Figure 4.1: Resistance distribution all measured data from three different wafers.
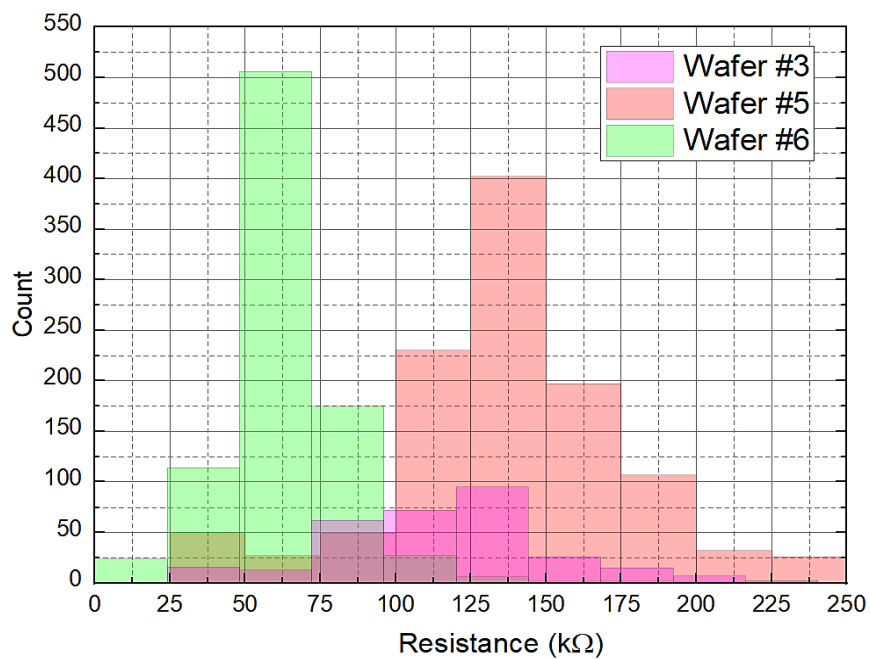
Figure 4.2: Resistance distribution for different microfabricated wafers.

72

The reason for taking multiple resistance measurements from pad structures is the pixel deformation. Some pixels have no metal interconnect that is over-etched during the fabrication process. Also, the histograms are widely spaced because of the presence of electrodes with different properties on the wafers given in the previous sections. In addition, the resistance values of wafer #6 are lower than expected. This is because the active material is coated with a different "W" doping rate than others. The coating thickness and doping concentration can be adjusted according to the electrode structure to be selected during the sensor production phase, and the sensor pixels will have the desired resistance. In order to compare the resistances connected to the electrodes, the resistance values are normalized according to the wafers' average. In this way, it can be seen how much below or above the average pixel resistances are. Electrode structures with very low or significantly above average resistance are not preferred because they require different active material thicknesses than the targeted. The resistance distributions according to the electrode structures are given in APPANDICES.B. Since some electrode structures are used in many pixel designs (for example, electrodes v1 and v8), the histograms of these structures are more crowded. Some electrodes have less frequent histograms when a small number of designs are used. However, it is considered that the graphics of these designs are sufficient to give an idea. When the histograms are examined, it is seen that the electrode designs v3, v7, and v12 give much lower resistance than the average. Therefore, pixel designs with this electrode structure are not preferred. So, that is why Design #3, 11, 28, and 29 might show bad performance.

After determining which pixel structures can be used, resistance as a function of temperature has been acquired in the 20°C to 30°C temperature range. The temperature is swept by a thermoelectric cooler (TEC). Then, it is fitted with a polynomial curve to calculate the temperature coefficient of resistance (TCR). **Figure 4.3** shows the relationship between resistance and TCR as a function of temperature.
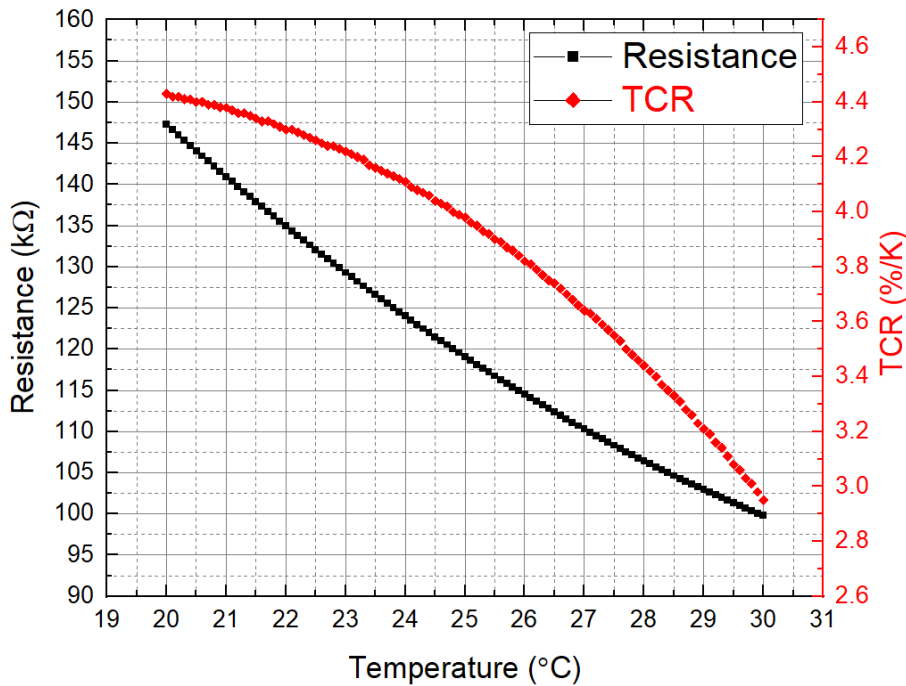
Figure 4.3: Measurement of resistance and TCR change by temperature (measurements were taken from Design #9).

The TCR value is measured -3.98 %/K at room temperature (25°C) from microfabricated wafer #3 and design #9, as shown in **Figure 4.3**. This value is achieved higher than the previously studied thesis at METU MEMS Center [59]. The higher value of the TCR, the higher response at the pixel structure is attained.

4.2   Noise Measurements

A crucial parameter in the performance of microbolometer detectors is the noise from the detector resistance. Thermal noise and 1/f noise are the dominant noises for the microbolometer pixel. The others have a low contribution to the noise apart from these two noises. As stated in Chapter 2, every resistance has a thermal noise when it is biased and a 1/f noise when it is biased. The 1/f corner frequency denotes the frequency at which these two noises become equal. This frequency should be as low as feasible to ensure minimal noise and good performance of the detector.
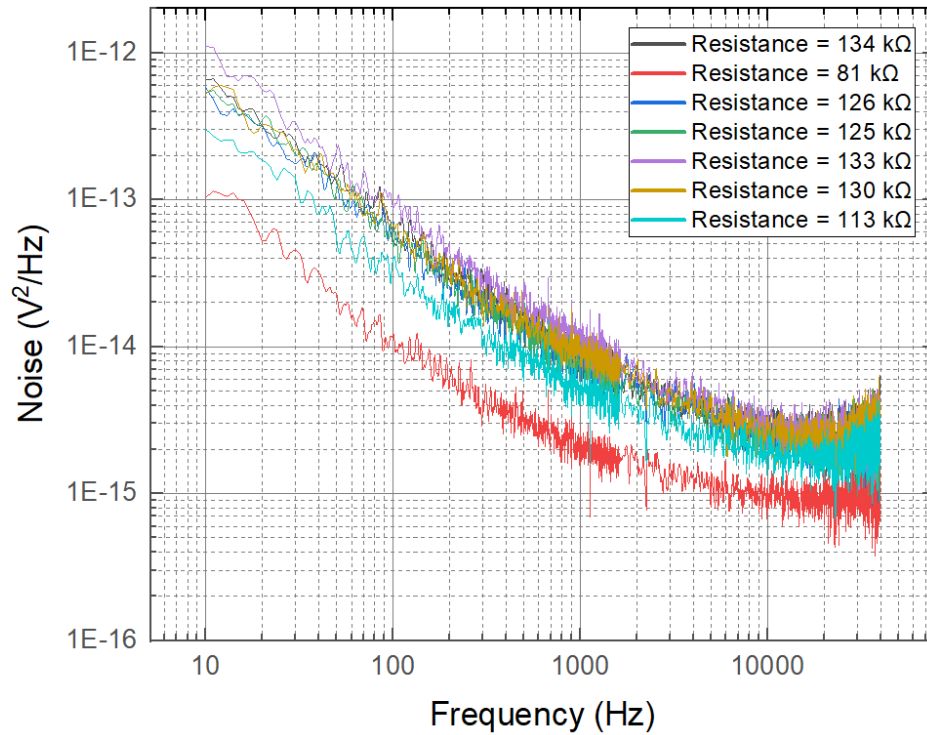
Figure 4.4: The spectral density of detectors that have different resistance values at room temperature.

The noise measurements are taken at a constant current of 10 µA. The measurements can be seen in **Figure 4.4**. The noise value changes with resistance change. In this case, while the resistance values are decreasing, measured noise is also decreased same as the corner frequency.

Table 4.1: Summary of the measurements at the different resistance values at 10 µA current bias.

Resistance (kΩ)	*81*	*113*	*134*
Theoretical Noise Floor *(Johnson Noise) [V²/Hz]*	1.05×10^{-15}	1.77×10^{-15}	4.64×10^{-15}
Corner Frequency [kHz]	0.85	1.9	3
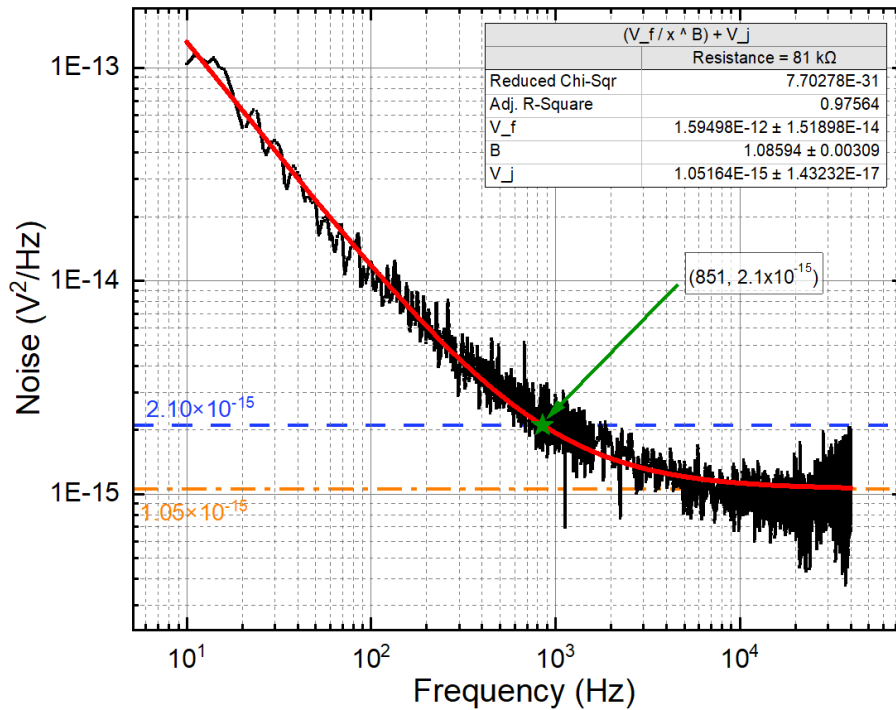
Figure 4.5: Measurement result of the noise power spectral density of a pixel with the resistance value is 81 kΩ, current bias is at 10 μA, and the corner frequency is calculated as 0.85 kHz.

4.3 Thermal Conductance Measurements

Thermal conductance is the most critical parameter that affects the microbolometers performance. The pixels should be suspended to eliminate heat dissipation to the sacrificial layer. Also, heat conduction is affected by the environment. In order to eliminate the convectional heat transfer from the air, the measurements are taken in a vacuum. The environment is taken into the vacuum until the heat transfer is only limited by conduction that transfers only from the arms.

While taking I-V measurements, the current that passes through the detector pixel is increased gradually. The voltage change is observed. At first, the linearity on the I-V graph is expected because there is no significant change in the temperature. After

the current is increased, the pixel body starts to heat. That means high current bias created excessive heat on the pixel, creating a performance drop on the pixel sensitivity. This excessive heating creates a non-linearity on the I-V curve. So, pixel resistivity is changed by this effect. This phenomenon can be seen in **Figure 4.6**.
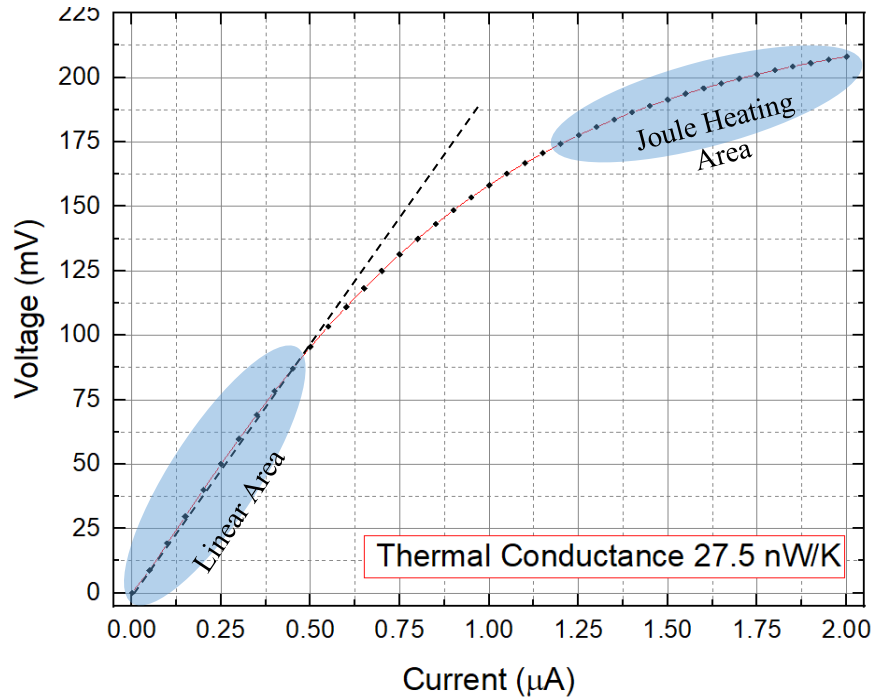
Figure 4.6: I-V curve of the biased pixel with joule heating zone from Design #18.

Using the I-V characteristic of the pixel, thermal conductance (G_{th}) can be calculated [36].

$$G_{th} = \frac{P_{elec}}{\Delta T} = \frac{I^2 R}{\ln\left(\frac{R}{R_0}\right)\frac{1}{\alpha}} = \frac{I^2 R \alpha}{\ln\left(\frac{R}{R_0}\right)} \qquad (4.1)$$

where G_{th} is the thermal conductance of the detector, P_{elec} is the applied electrical power, ΔT is the total temperature change, R is the detector resistance under vacuum,

R_0 is the detector resistance at atmospheric pressure, α is the TCR of the detector resistance, and I is the applied bias current.
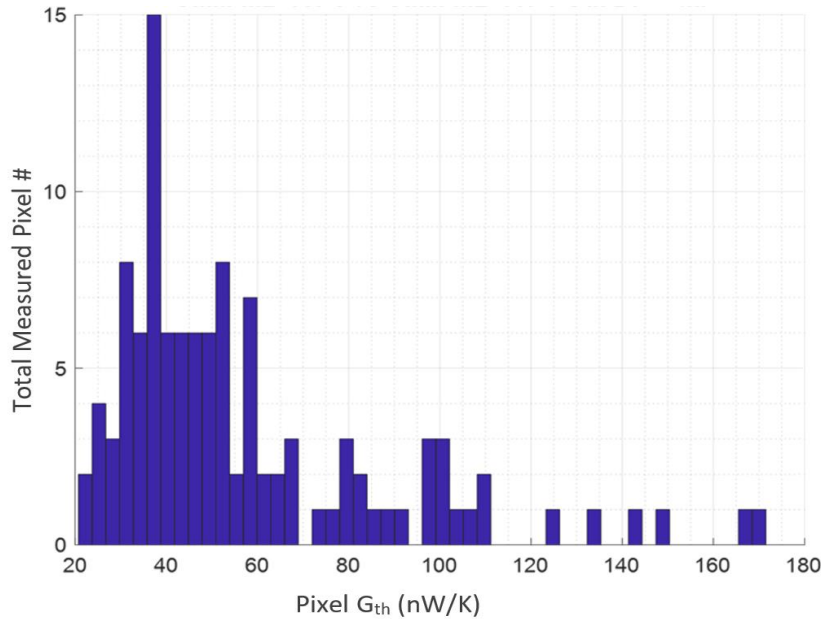
Figure 4.7: Thermal Conductance (nW/K) distribution from measured pixels.

Thermal conductance measurements on the microfabricated wafer #3 (structural thickness is 300nm) and #6 (structural thickness is 200nm) show that G_{th} mainly accumulates between 25 nW/K to 57 nW/K seen in **Figure 4.7**. Also, these wafers and designs are compared individually in **Figure 4.8** and **Figure 4.9** for wafer #3 and wafer #6, respectively.

When thermal conductance values of the pixels are compared with simulation data and measured values, they are mostly correlated. There is some deviation in the measurement, like Design #15 in **Figure 4.8**. The reason for this might be the buckling or process deformity in the pixel. However, thermal conductance measurements for both wafers matched even get better values from simulations.
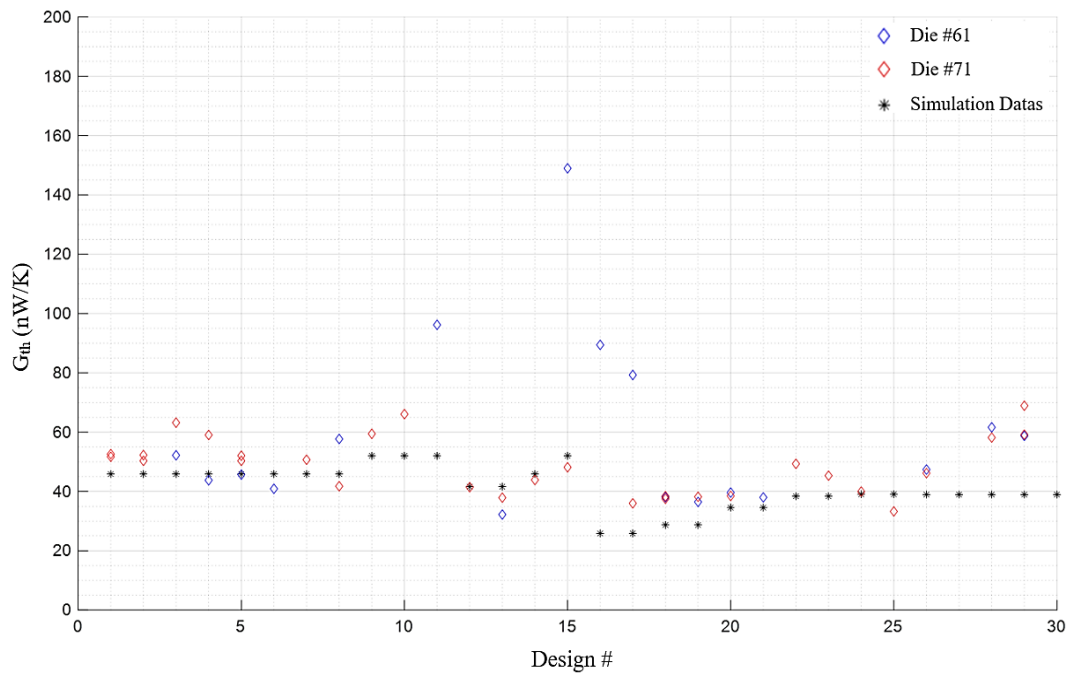
Figure 4.8: Thermal conductance distribution for Wafer #3.
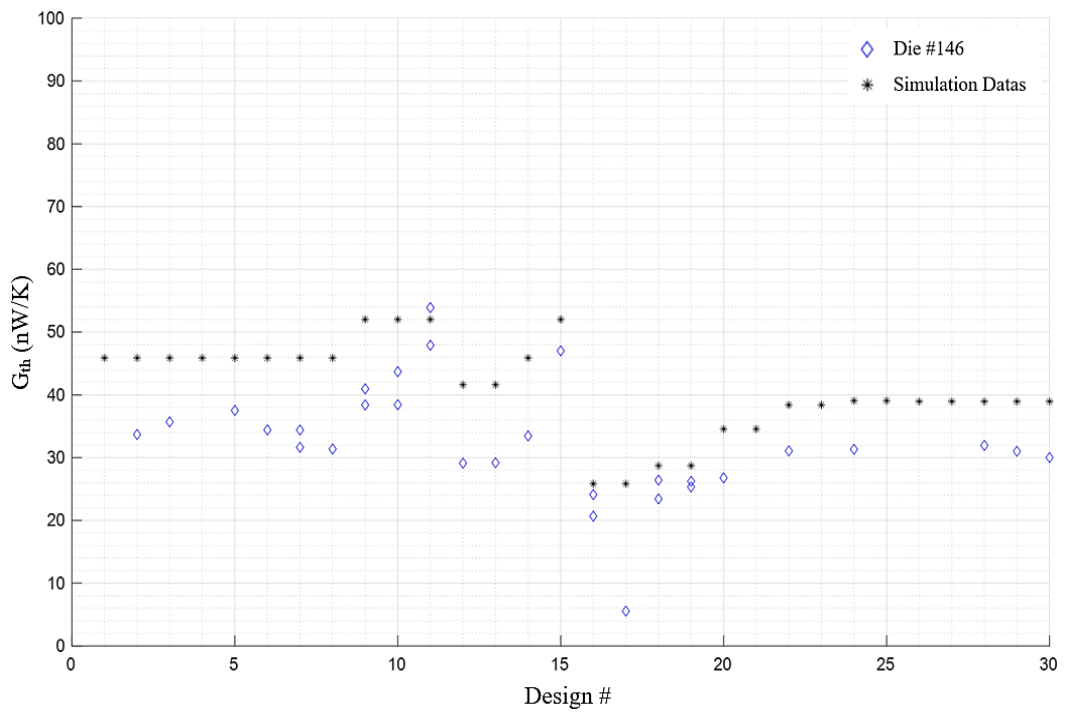
Figure 4.9: Thermal conductance distribution for Wafer #6.

4.4   Absorption Measurements

Pixels are designed for maximum absorption in 8-14 µm at the spectrum. The FTIR measurements are taken at METU MEMS Facility with BRUKER' Lumos FTIR microscope. Before taking measurements, device calibration is done with the reflective surface. The surface employed a gold plated that is only designated on a specific place on the die. The idea is to create the same reflective surface that is fabricated with the same bolometer fabrication process. After taking reference measurement from Au reflective surface, each design's reflection, transmission measurements are taken from array structures located center of each die which can be seen in **Figure 3.2**. Absorption data is extracted from these measurements. As an example, design #18's measurements are shown in **Figure 4.10**. Also, each design's absorption curves are shown in **Figure 4.11**.
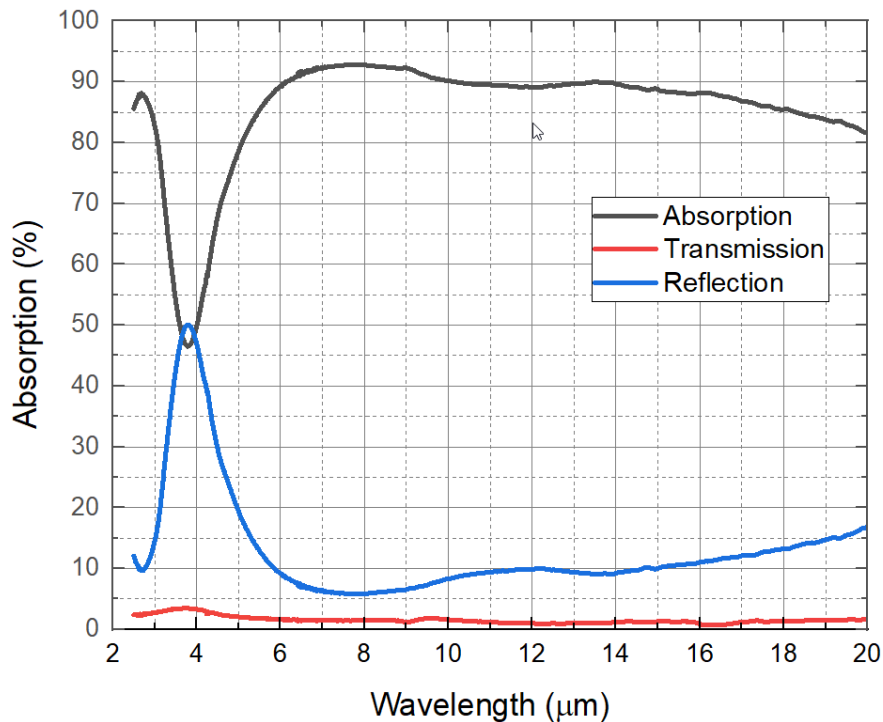
Figure 4.10: FTIR measurement for Design #18 from wafer #3.

Each design is measured like previously mentioned. The comparison of the normalized absorption for each pixel array shows a 10% margin between the best and the worst absorption characteristics of the pixels. Also, ~ 90% absorption between desired 8-14 µm at the spectrum should result in a high response. The responsivity measurements are given in the following sections.
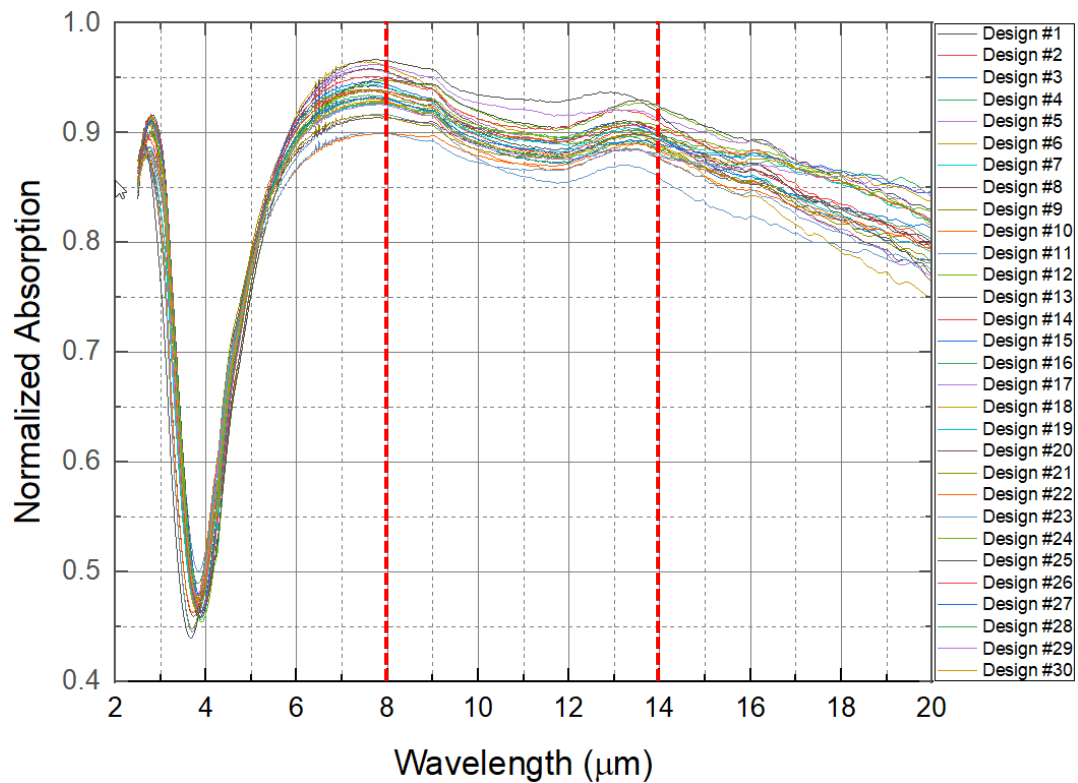
Figure 4.11: Absorption measurement for each design # at wafer #3 with desired absorption window 8-12 µm.

4.5   Responsivity and Thermal Time Constant Measurements

The responsivity is another critical parameter that determines microbolometer performance. The responsivity measurements are collected at the METU MEMS Facility. In **Figure 4.12**, the schematic view of the setup used for measuring responsivity is shown. The pixel is placed in the dewar, which is kept at low vacuum

pressure. The pixel is then exposed to infrared radiation generated by the blackbody shown in the figure, which is modulation frequency between 10 and 100 Hz.
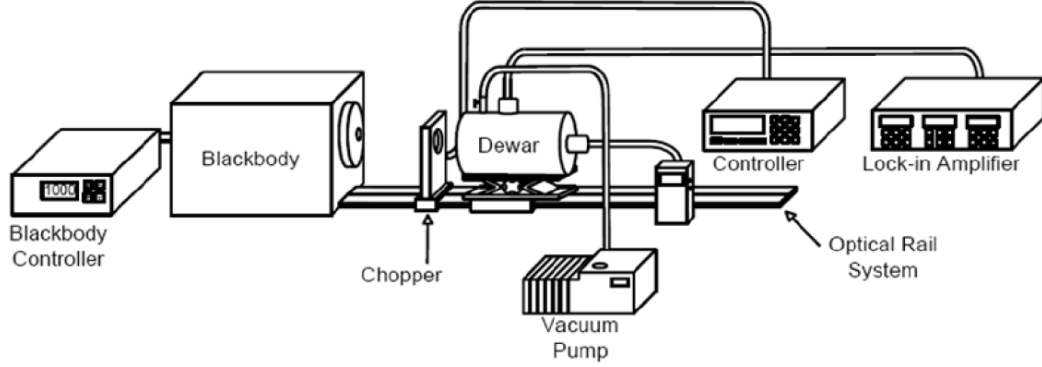
Figure 4.12: Schematic view of the responsivity measurement test setup [64].

The pixels' responsivity, $\Re$, is calculated from

$$\Re = \frac{\Re_{DC}}{\sqrt{1 + \omega\tau^2}}$$ (4.2)

where is the $\Re_{DC}$ responsivity of the pixel, ω is the modulation frequency of the incident radiation, and τ is the thermal time constant of the pixel. Same as Equation (4.2), the detector's voltage responsivity with respect to frequency is expressed in Equation (4.3).

$$V = \frac{V_{DC}}{\sqrt{1 + \omega\tau^2}}$$ (4.3)

By using these formulas, the thermal time constant can be extracted from the fitted curve. It is measured by heating the pixel using pulsed current bias. The output voltage change of the pixel is measured, and the thermal time constant is calculated using this measurement.

82
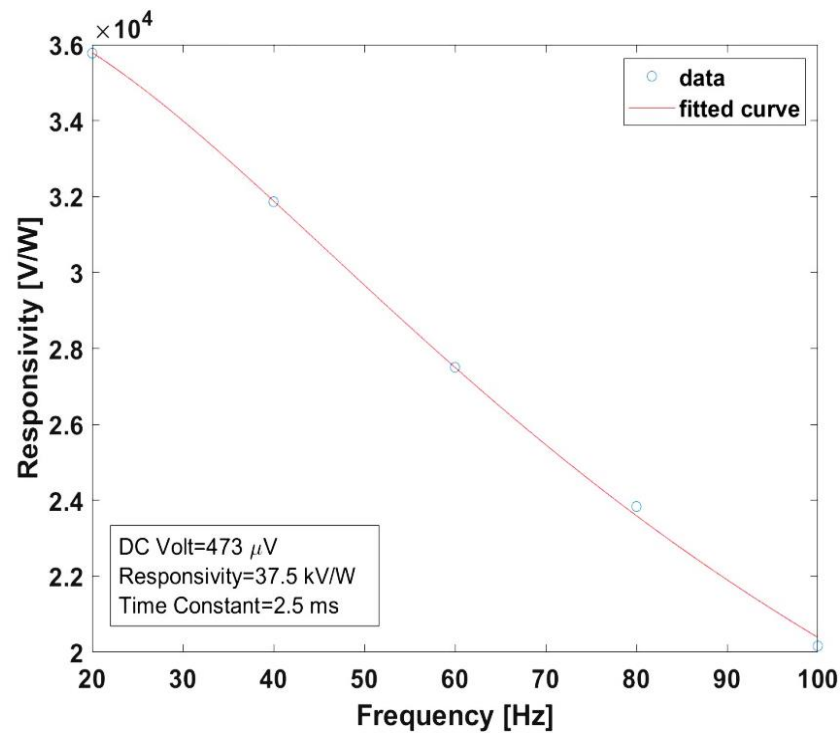
Figure 4.13: Example of measured responsivity values of design #18 from wafer #3.

Normalized responsivity for different wafers and dies are measured (in **Figure 4.14** and **Figure 4.15**). There are not many differences between designs, but some of them are very promising to further improvements. Among these designs, designs #12 and #16 from wafer #6, and designs #17 and #18 from wafer #3 give the best response apart from other designs after measurements. Even these designs are very close to others, some of them can be fabricated as an FPA. Between the wafers #3 and #6, wafer #6 has a better responsivity because thickness creates a better response resulting from improved thermal conductance value, as seen in previous measurements.
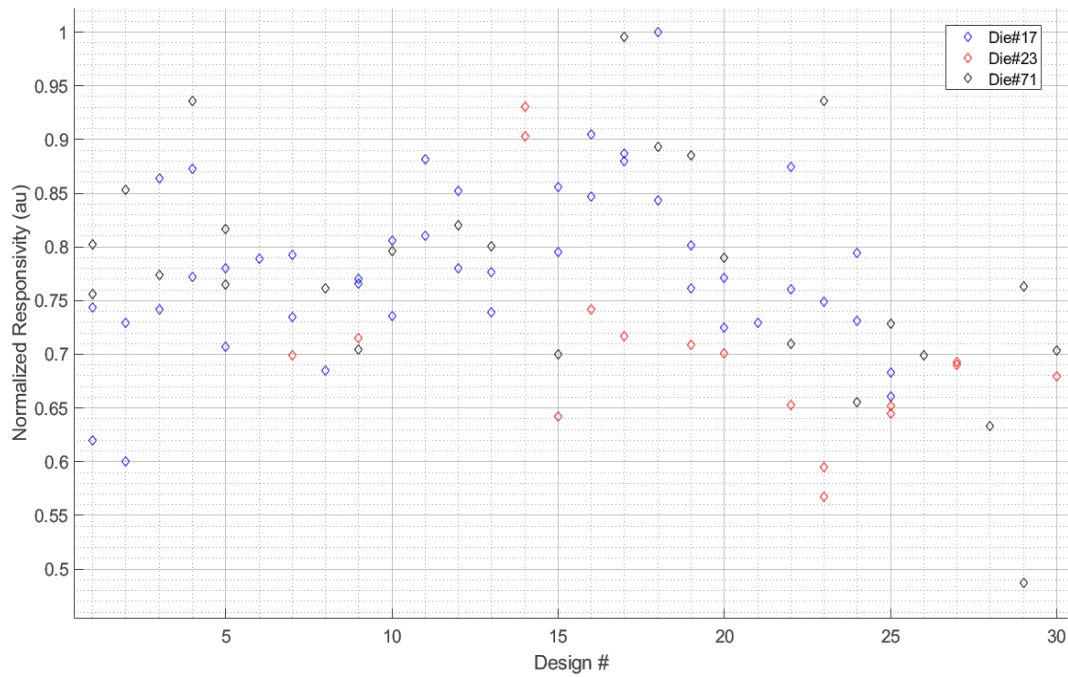
Figure 4.14: Normalized responsivity with respect to design # for wafer #3.
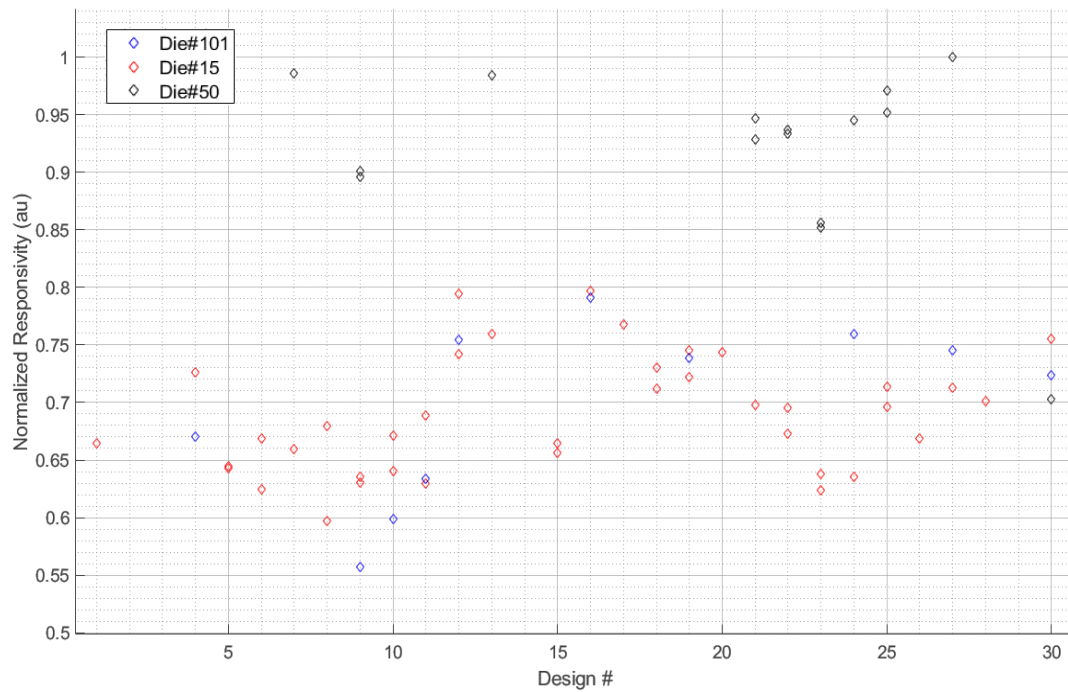
Figure 4.15: Normalized responsivity with respect to design # for wafer #6.

84

Measured thermal time constant data from wafer #3 compared with simulation data as seen in **Figure 4.16**. The measurements and simulation data are very close.
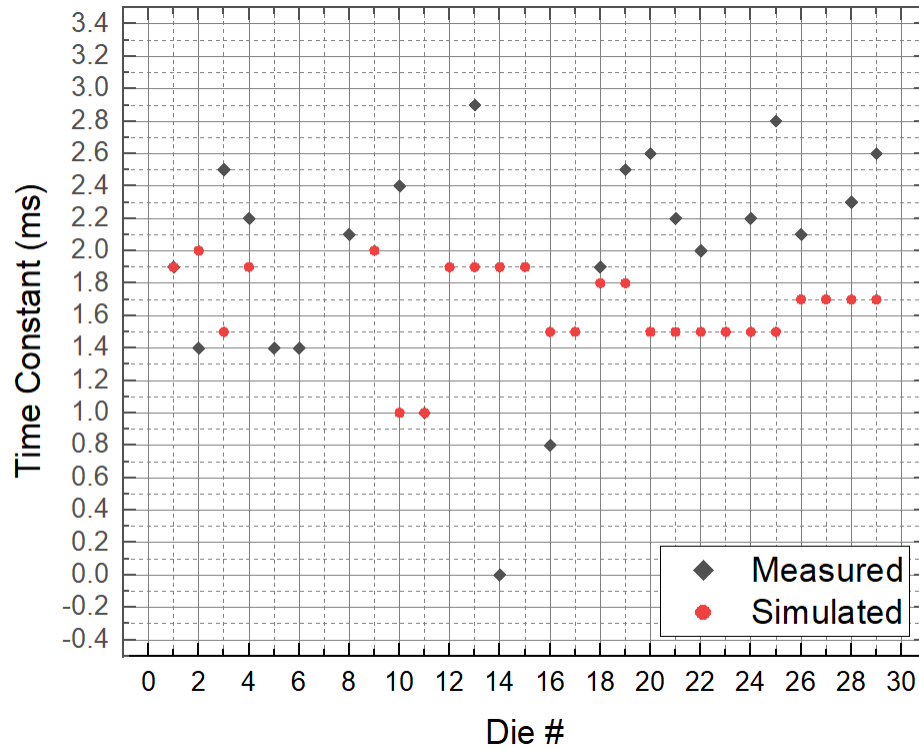
Figure 4.16: Thermal time constant distribution from Wafer #3.

4.6 Application on FPA and its Performance

Considering all measured data collected from test wafers, some of the designed 12 μm microbolometer pixels are fabricated on CMOS ROIC with 640x480 format. Designs #4, 14, 18, and 27 show the best performance among other designs. The wafer is divided into four subregions, and these four designs are fabricated on the same wafer as seen in **Figure 4.17**. With this method, all designs faced from same fabrication conditions.
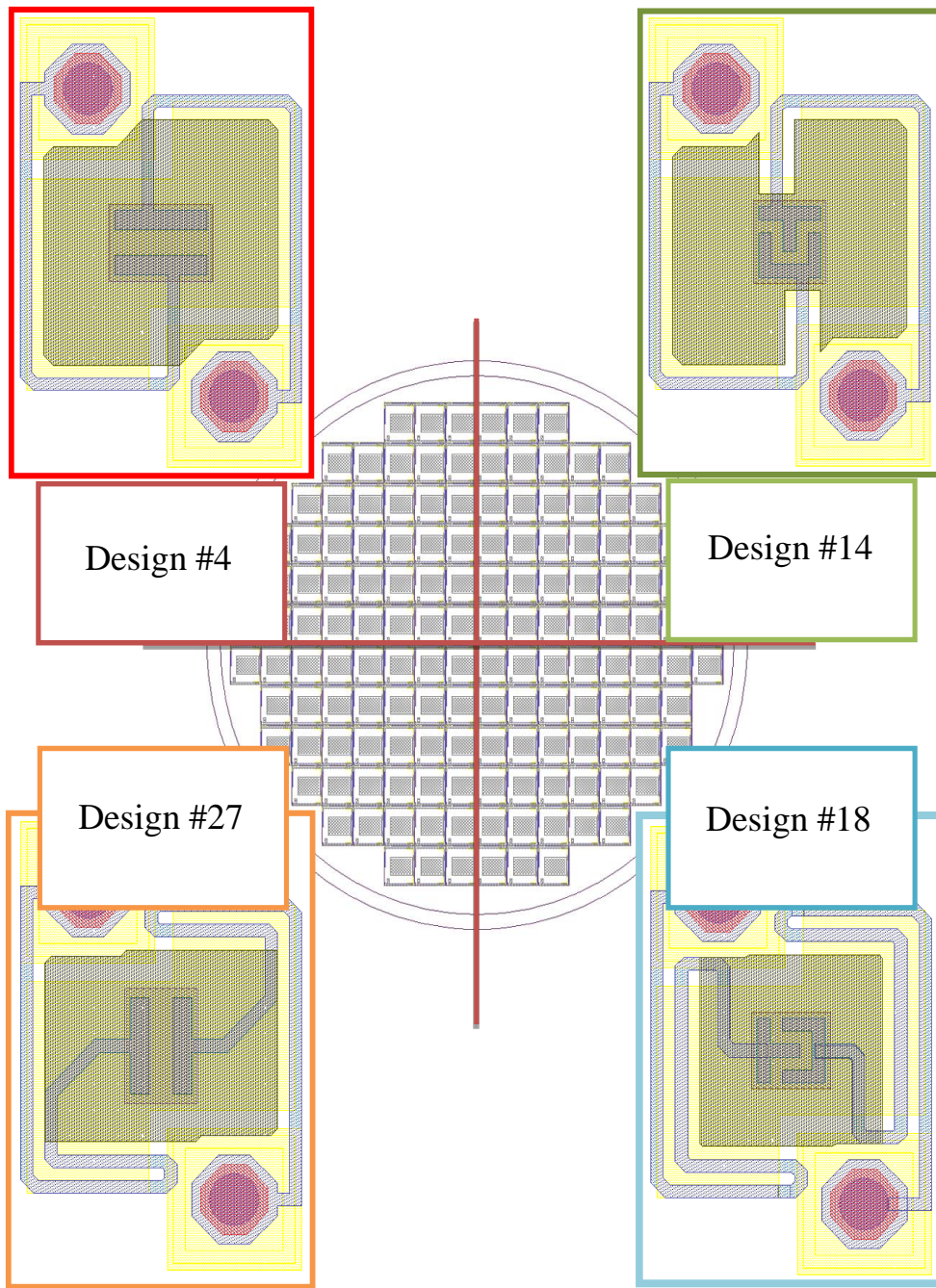
Figure 4.17: Design location on fabricated CMOS ROIC.

Table 4.2: Performance comparison of the fabricated pixels with different designs.

Design#	Noise (a.u.)	Responsivity (mV/K)	NETD (mK)		Dead Pixel Ratio (%)
			Mean	Peak	
4	5.59	4.08	383	311	5.81
14	9.01	7.76	301	261	5.98
18	7.65	9.29	222	189	4.35
27	5.23	5.66	239	214	2.98

Fabrication of the CMOS wafers was followed the same fabrication steps and the same film thicknesses with test wafers. Because these process flows are created by considering the post-CMOS process. After fabricating the FPAs, characterization is performed by METU MEMS CENTER test crew. The comparison between the designs fabricated on the same wafer is shown in **Table 4.2**.

Fabricated pixels' performance shows us that responsivity is one of the important factors. Because pixel responsivity directly affects the final pixel performance NETD. Also, thermal conductance, which is the subdivision of the responsivity of the pixel, is the key parameter for pixel performance. The structures are seen in **Figure 4.17**, the long arm affects the performance which is given in **Table 4.2**.

After determining the best pixel that shows the best NETD value, another run for fabrication is performed. The best pixel performance is taken from Design #18. The fabricated wafer contains that design. The final form of this fabricated FPA's SEM pictures after release process is given in **Figure 4.18**. The fabricated Design#18's final performance parameters for this wafer are shown in **Figure 4.19** and **Figure 4.20**. These performance measurements are taken by METU MEMS Test crew.
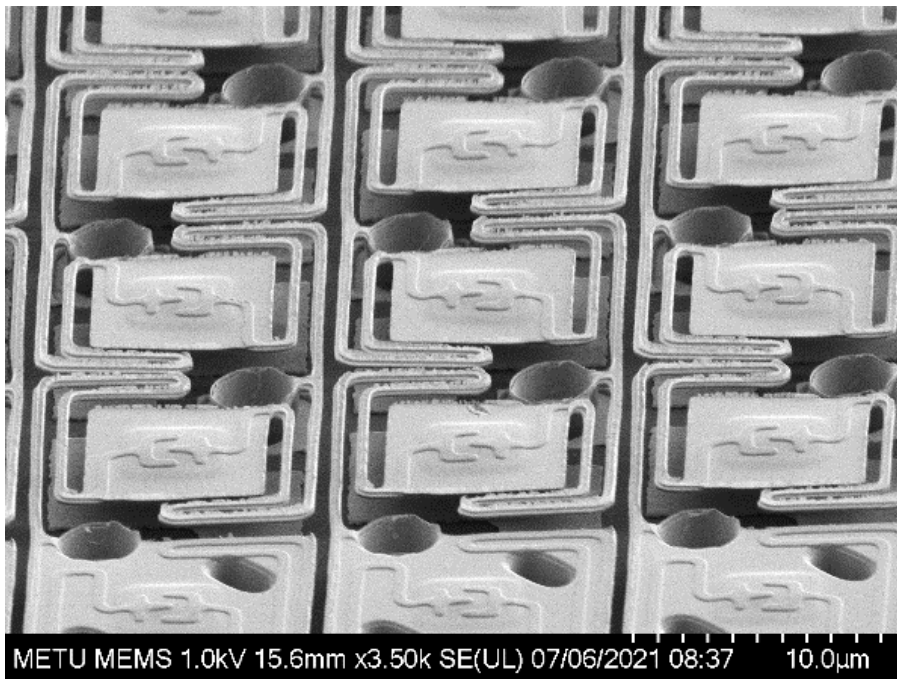
(a)
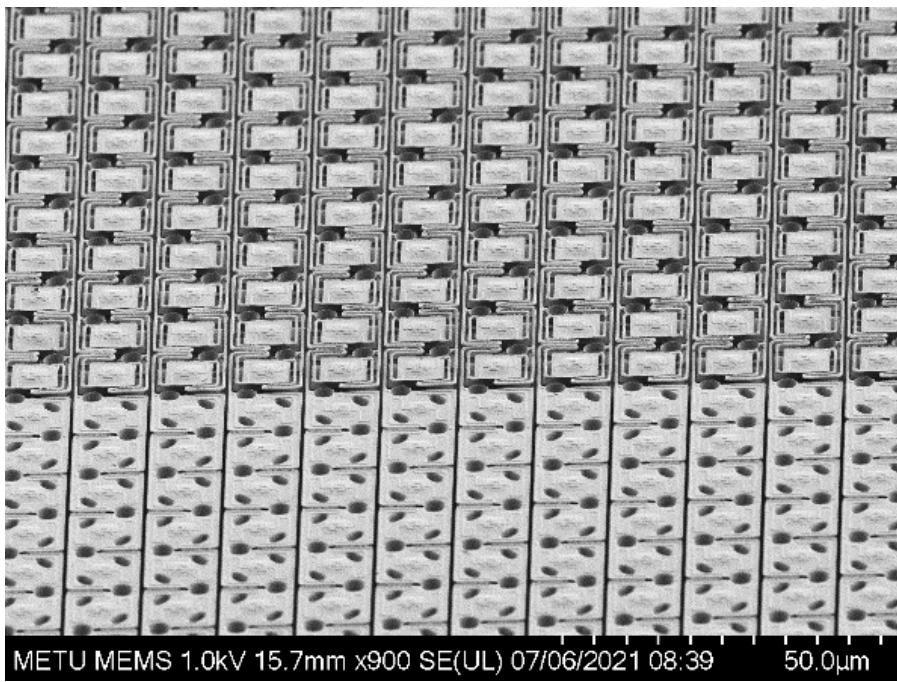
(b)

Figure 4.18: SEM images after fabrication of the pixel in FPA on CMOS wafer.
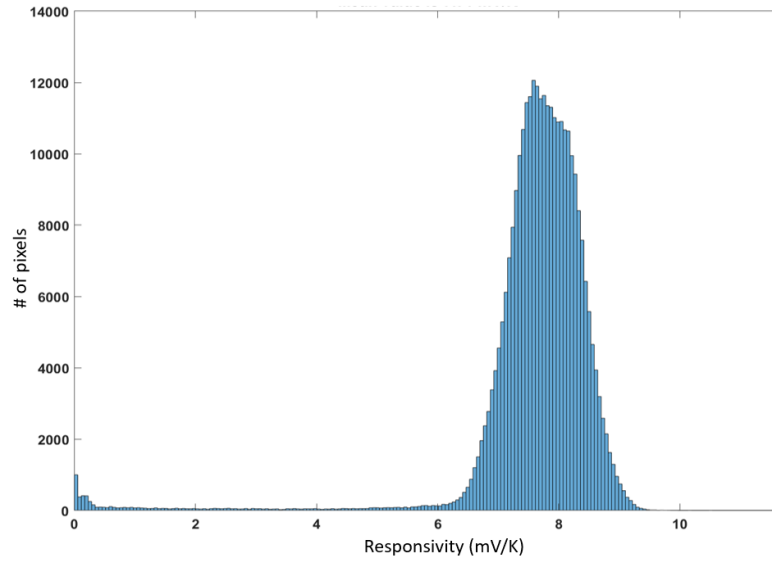
Figure 4.19: Responsivity measurement result for design #18. The mean value is measured as 7.71 mV/K.
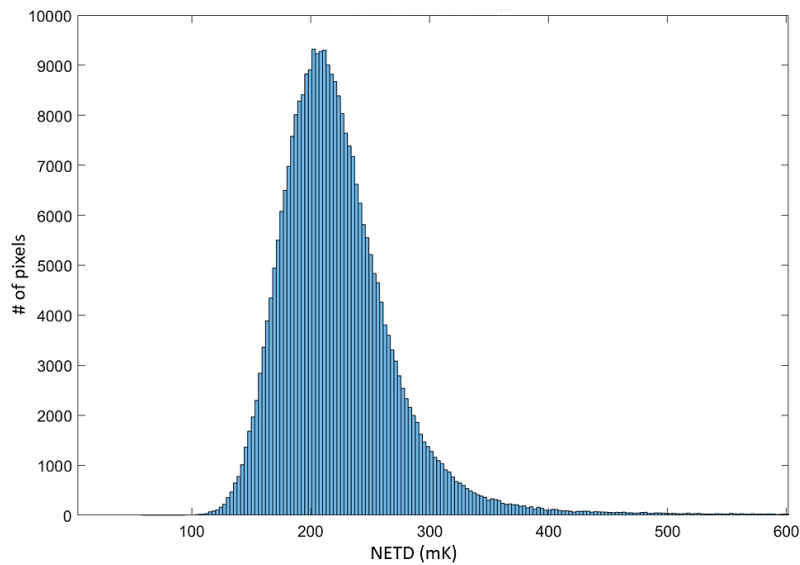
Figure 4.20: NETD measurement result for design #18. The mean value and peak value of the NETD are measured as 227 mK and 203 mK, respectively.

Figure 4.21 shows the infrared images are taken with FPAs. Even the pixel performance should be improved, and these images show that fabrication processes are successfully completed. So, fabrication flow is compatible with FPA fabrication.

(a)

(b)

Figure 4.21: Images obtained by 640x480 format FPA that contains design #18 with 12 µm pixel pitch.

4.7   Conclusion

This chapter shows the performances of the designs by using fabricated test wafers. The measured properties are resistance, TCR, noise, thermal conductance, absorption characteristics in FPA, responsivity, and time constant. The TCR of the detectors from multiple measurements is found between ~3.5 %/K and ~4.2 %/K. The thermal conductance of the pixels is correlated with simulation data, and as an example, design #18's, which shows the best performance among the designs, is measured ~27.5 nV/K from wafer #6. The pixel absorptance for all designs is above 85% that extracted from FTIR measurements from pixel arrays. Also, pixel's thermal time constants are mostly below ~3 ms, which reacts very fast in moving objects. After finding the best performed and easy fabricating designs, these are fabricated as 640x480 FPA on CMOS wafers. Their performance is compared in **Table 4.2**. Also, design #18 is compared with previous designs at METU MEMS (**Table 4.3**).

Table 4.3: Summary of the detector performance that previously studied at METU.

	50 μm Single Level Pixel at [36]	35 μm Single Level Pixel at [49]	25 μm Multi Level Pixel at [35]	This Study [Design #18]
Pixel Pitch	50 μm	35 μm	25 μm	12 μm
Fill Factor	64%	43%	92%	58%
Absorptance	60%	70%	54%	>90%
TCR	-3.4 %/K	-3.25 %/K	-2.8 %/K	-4 %/K
Resistance	150 kΩ	85 kΩ	55 kΩ	205 kΩ
Thermal Conductance	90 nW/K	25 nW/K	17.4 nW/K	27.5 nW/K
Thermal Time Constant	15.4 ms	22.6 ms	17.5 ms	~1.9 ms
Convenient Format for FPA Applications	320x240	384x288	640x480	640x480
NETD	~450 mK	~55 mK	36.0 mK (estimated)	~200 mK

CHAPTER 5

CONCLUSION and FUTURE WORK

The research objective of this study is the development of a 12 µm pitch single layer resistive type uncooled microbolometer detector pixel. The pixel's designs, fabrication, and testing are completed successfully. The results from the simulations are correlated with fabricated pixels. With getting results from the best pixel performance, this design is fabricated in large format 640x480 FPA. After successful fabrication of the FPAs, test results and images are obtained. The measured mean NETD of Design #18's FPA, which has the most extended support arm and electrode version #1, is ~200 mK. This result is promising for the first time development of the 12 µm pitch single layer VWO_x microbolometer pixel. However, this pixel performance should be improved.

The achievements and results obtained from this study can be summarized as:

1. Previously developed, VWO_x, at METU MEMS, is selected because of its considerably high TCR and low noise characteristic. By using these features, planar resistive structures are developed. The desired values for different resistive structures are tailored.

2. The pixel's absorption characteristic is investigated by using the cascaded transmission line method. The optimal thicknesses of the sacrificial and structural layers are determined in order to achieve the highest absorption coefficient. The developed pixel's overall absorption coefficient is calculated as around 90% with MATLAB software.

3. The single-layer 12 µm pitch pixels' structures are designed for the best possible performance. While trying to achieve high performance, pixels'

thermal conductance, absorption areas, resistive structures, and good mechanical stability are considered.

4. Electro-thermal and mechanical simulations are done with COMSOL Multiphysics software for various pixel structures. Thermal time constants, thermal conductance, responsivity, and mechanical deflections are calculated as best as 1 ms, ~28 nW/K, ~48 V/W, and a few nm, respectively. Also, these pixels are compared with each other to eliminate the pixels with lousy performance and find the pixels with the best performance.

5. The pixels are fabricated by using a CMOS-compatible fabrication flow. The process flow consists of seven masking layers. Each process stage is optimized for overall system performance. Following that, the pixels are constructed using these steps.

6. The test and the measurements are performed on the fabricated pixels. TCR value of -4 % /K is obtained for the active material. The noise of the fabricated pixels is also examined. The cutoff frequency of the resistive structure at 81 kΩ resistance is measured at approximately 0.85 kHz if the pixel is biased with a current of 10 μA. The thermal conductance values of pixels are measured as low as between 20 nW/K and 55 nW/K, with time constants of no more than 3 ms for wafer #6. The absorptance of all pixel designs is also measured minimum ~85 %.

7. The fabrication of a 640x480 FPA comprised of the specified pixels has been accomplished. The array's NETD is determined, and many infrared pictures are acquired using the constructed FPAs. The best measured FPA's NETD is ~200 mK, which is greater than anticipated given the present test configuration.

Although the findings of this research are encouraging for high-performance and high-resolution imaging for 12 μm pixel pitch microbolometer, more work is required to enhance performance. The following are the tasks that will need to be completed in the future:

1. The resistive structure and active material correlation should be improved. If it is vital, the resistive structure can be changed to a sandwich-type structure even it brings more fabrication processes. So, a more controllable electrode structure is necessary.

2. The minimum feature size should be more controllable. Controlled structures give more stable fabrication steps.

3. Even if optical properties are good, the absorption of the incoming IR radiation is not entirely absorbed because of the low fill factor, which is the nature of the single-layer structures. To increase absorption, a two-level system like an umbrella structure can be developed. This design brings more fabrication steps into the system, but it will help to increase absorption. With this two-level system, thermal conductance value can be diminished.

4. Multi-level structural layer stacks like silicon nitride and silicon oxide combination may increase the mechanical stability and increase the absorption of the pixel structure. With this, a thinner pixel body and arms can be achieved that resulting in better thermal conductance.

5. Planarization of the pixels is one of the critical factors during the fabrication of the FPAs. When the minimum feature size in the structure diminishes, smaller topographical differences create a deformation in the lithography stages. So, planarize surface might minimize this problem.

6. A state-of-art microbolometer structure may be considered rather than conventional geometries. Because when the structures became smaller, geometrical considerations have emerged. Elimination of these restrictions may improve the microbolometer performance.

REFERENCES

[1]   P. Aivaliotis, "New Developments in InAs / InGaAs Quantum Dot-in-a-well Infrared Photodetectors," University of Sheffield, 2007.

[2]   HORIBA, "Introduction to the detectors techniques," 2021. [Online]. Available: https://www.horiba.com/en_en/technology/measurement-and-control-techniques/spectroscopy/detectors/. [Accessed: 21-Aug-2021].

[3]   G. Finger, "Detectors in Astronomy." European Southern Observatory.

[4]   M. D. Shaw, "Superconducting nanowire single photon detectors for optical communication and astronomy," in *X-Ray, Optical, and Infrared Detectors for Astronomy IX*, 2020.

[5]   V. C. Coffey, "Seeing in the Dark: Defense Applications of IR imaging," 2011. .

[6]   "Thermal sensors: A market with many applications," 2009. [Online]. Available: https://www.lynred.com/blog/thermal-sensors-market-many-applications. [Accessed: 22-Aug-2021].

[7]   "Thermography Application Areas." [Online]. Available: https://www.infratec.eu/thermography/industries-applications/. [Accessed: 21-Aug-2021].

[8]   Yole Développement, "Thermal detectors market size scenario based on COVID-19 impact worldwide from 2019 to 2020, by application(in million U.S. dollars)," 2020. [Online]. Available: https://www.statista.com/statistics/1222277/global-thermal-detectors-application-market-size/.

[9]   J.-X. Fu, "Coherent Near Infrared Photodetection With Indium Gallium Arsenide Based Optoelectronic Devices," Stanford University, 2005.

[10]   "Infrared Radiation: Sensor division knowledge." [Online]. Available: https://www.infratec-infrared.com/sensor-division/service-support/glossary/infrared-radiation/. [Accessed: 21-Aug-2021].

[11]   "Blackbody Radiation: Wien's Displacement Law." .

[12]   J. Mikołajczyk *et al.*, "Analysis of free-space optics development," *Metrol. Meas. Syst.*, vol. 24, no. 4, pp. 653–674, 2017.

[13]   H. Budzier and G. Gerlach, *Thermal Infrared Sensors: Theory, Optimisation and Practice*. Wiley, 2011.

[14]   A. W. van Herwaarden and P. M. Sarro, "Thermal Sensors Based on Seeback Effect," *Sensors (Peterborough, NH)*, vol. 10, no. 1986, pp. 321–346, 1986.

[15] T. Akın, "CMOS-based Thermal Sensors," in *Advanced Micro and Nanosystems*, vol. 2, Wiley-VCH, 2005, pp. 479–512.

[16] "Applied Physics:Thermoelectric effect." [Online]. Available: https://dducollegedu.ac.in/Datafiles/cms/ecourse content/Applied Physics_Thermoelectric effect.pdf. [Accessed: 22-Aug-2021].

[17] P. Muralt, "Micromachined infrared detectors based on pyroelectric thin films," 2001.

[18] K. Domke and A. Odon, "Thermo-electric model of a pyroelectric detector," in *Advanced Computational Methods and Experiments in Heat Transfer XII*, 2012, pp. 261–269.

[19] S. Eminoglu, M. Y. Tanrikulu, and T. Akin, "A low-cost 64x64 uncooled infrared detector array in standard CMOS," in *TRANSDUCERS 2003 - 12th International Conference on Solid-State Sensors, Actuators and Microsystems, Digest of Technical Papers*, 2003, pp. 316–319.

[20] S. Eminoglu, M. Y. Tanrikulu, D. S. Tezcan, and T. Akin, "Low-cost small-pixel uncooled infrared detector for large focal plane arrays using a standard CMOS process," in *Infrared Detectors and Focal Plane Arrays VII*, 2002.

[21] N. Shen, J. Yu, and Z. Tang, "An uncooled infrared microbolometer array for low-cost applications," *IEEE Photonics Technol. Lett.*, vol. 27, no. 12, pp. 1247–1249, 2015.

[22] Y. Kosasayama *et al.*, "Pixel scaling for SOI-diode uncooled infrared focal plane arrays," in *Infrared Technology and Applications XXX*, 2004, p. 504.

[23] M. A. Gülden, "A Low-Cost Uncooled Infrared Imaging Sensor Using MEMS and a Modified Standars CMOS Process," Middle East Technical University, 2013.

[24] M. Ueno *et al.*, "640 x 480 pixel uncooled infrared FPA with SOI diode detectors," in *Infrared Technology and Applications XXXI*, 2005.

[25] P. W. Kruse, *Uncooled Thermal Imaging Arrays, Systems, and Applications*. Bellingham, Washington USA: SPIE Press, 2001.

[26] BAE Systems, "BAE Systems Athena1920 Microbolometer Thermal Camera Core." [Online]. Available: https://www.baesystems.com/en-media/uploadFile/20210407065838/1434628459234.pdf.

[27] A. Rogalski, P. Martyniuk, and M. Kopytko, "Challenges of small-pixel infrared detectors: A review," 2016.

[28] "Leonardo Tenum® 640 _ Commercial Thermal Infrared Camera Core." [Online]. Available: https://www.leonardodrs.com/commercial-infrared/products/uncooled-camera-modules/tenum-640/. [Accessed: 23-Aug-2021].

[29] M. William A. Radford, Richard Wyles, Jessica Wyles, John B. Varesi, F. C. Ray, Daniel F. Murphy, Adam Kennedy, A. Finch, Edgar A. Moody, and S. T. B. R. Coda, "Microbolometer uncooled infrared camera with 20-mK NETD," in *SPIE's International Symposium on Optical Science, Engineering, and Instrumentation*, 1998.

[30] S. THERMAL, "Seek Thermal Infrared Camera & Raytheon IR Microbolometer - Reverse Costing Analysis," 2015.

[31] J.-J. Yon, E. Mottin, and J.-L. Tissot, "Latest amorphous silicon microbolometer developments at LETI-LIR," in *Infrared Technology and Applications XXXIV*, 2008, p. 6940 69401W.

[32] T. Schimert *et al.*, "Advances in small-pixel, large-format α-Si bolometer arrays," in *Infrared Technology and Applications XXXV*, 2009, p. 7298 72980T.

[33] R. Sobolewski, D. P. Butler, and Z. Celik-Butler, "Cooled and uncooled infrared detectors based on yttrium barium copper oxide," in *Smart Optical Inorganic Structures and Devices*, 2001, pp. 204–214.

[34] P. Mérel, P. Laou, F. Wong, and D. Valcartier, "YBCO microbolometers for Infrared Detection Enhancement of performance with regionally thinned microbridges.pdf," 2009.

[35] Ş. E. Küçük, "Development of High Fill Factor and High Performance Uncooled Infrared Detector Pixels," Middle East Technical University, 2011.

[36] M. Y. Tanrıkulu, "An Uncooled Infrared Microbolometer Detector Array Using Surface Micromachined MEMS Technology," Middle East Technical University, 2007.

[37] M. Moreno, R. Jiménez, A. Torres, and R. Ambrosio, "Microbolometers Based on Amorphous Silicon-Germanium Films With Embedded Nanocrystals," *IEEE Trans. Electron Devices*, vol. 62, no. 7, pp. 2120–2127, 2015.

[38] A. Abdullah *et al.*, "Micromachined Uncooled SixGeyO1-x-y Microbolometer Integrated Metasurface for Uncooled Infrared Detection," in *2019 20th International Conference on Solid-State Sensors, Actuators and Microsystems and Eurosensors XXXIII, TRANSDUCERS 2019 and EUROSENSORS XXXIII*, 2019, pp. 641–644.

[39] R. Jimenez *et al.*, "Fabrication of microbolometer arrays based on polymorphous silicon–germanium," *Sensors (Switzerland)*, vol. 20, no. 9, 2020.

[40] "LeonardoDRS tenum-640_datasheet." .

[41] LYNRED, "LYNRED_ATTO1280 Datasheet_12um Pixel.pdf." [Online].

Available: https://www.lynred.com/sites/default/files/2021-07/ATTO1280 Datasheet.pdf.

[42] P. Wang *et al.*, "High Sensitivity 17um Pixel Pitch 640x512 Uncooled Infrared Focal Plane Arrays Based on Amorphous Vanadium Oxide Thin Films," *IEEE Electron Device Lett.*, vol. 36, no. 9, pp. 923–925, 2015.

[43] M. Kohin and N. R. Butler, "Performance limits of uncooled VO x microbolometer focal plane arrays," in *Infrared Technology and Applications XXX*, 2004.

[44] S. Muneer *et al.*, "Activation energy of metastable amorphous Ge2Sb2Te5 from room temperature to melt," *AIP Adv.*, vol. 8, no. 6, 2018.

[45] Y. Lv, M. Hu, M. Wu, and Z. Liu, "Preparation of vanadium oxide thin films with high temperature coefficient of resistance by facing targets d.c. reactive sputtering and annealing process," *Surf. Coatings Technol.*, vol. 201, no. 9-11 SPEC. ISS., pp. 4969–4972, 2007.

[46] D. T. Nguyen, "Design , modeling , and characterization of innovative terahertz detectors," University of Granoble, 2013.

[47] A. Shafique, "Modeling and Characterization of High TCR, Low Noise Si/SiGe Multi-Quantum Well Detector for Uncooled Microbolometers," Sabancı University, 2018.

[48] O. Celik and M. Duman, "High temperature coefficient of resistance and low noise tungsten oxide doped amorphous vanadium oxide thin films for microbolometer applications," *Thin Solid Films*, vol. 691, 2019.

[49] Ş. U. Şenveli, "Development of High Thermal Performance Uncooled Infrared Detector Pixels with Enhanced Resistor Structures," Middle East Technical University, 2010.

[50] S. E. Kucuk, M. Yusuf Tanrikulu, and T. Akin, "A detailed analysis for the absorption coefficient of multilevel uncooled infrared detectors," in *Infrared Technology and Applications XXXVII*, 2011.

[51] S. Eminoğlu, "Uncooled Infrared Focal Plane Arrays With Integrated," Middle East Technical University, 2003.

[52] R. Cetin, O. Erturk, and T. Akin, "Design, Analysis and Implementation of Quarter-wave Absorber Structure for Uncooled Infrared Detectors with High Fill Factor," in *International Conference on Infrared, Millimeter, and Terahertz Waves, IRMMW-THz*, 2018.

[53] R. Çetin, "Design and Implementation of Perforation on High Fill Factor Structures for Uncooled Infrared Sensors," Middle East Technical University, 2016.

[54] D. X. Zhou, E. P. J. Parrott, D. J. Paul, and J. A. Zeitler, "Determination of

complex refractive index of thin metal films from terahertz time-domain spectroscopy," *J. Appl. Phys.*, 2008.

[55]   "Comsol Material Database." .

[56]   E. Dawit, "Electro-Thermal Mechanical Modeling of Microbolometer for Reliability Analysis," University of Waterloo, 2010.

[57]   Y. Z. Deng, S. F. Tang, H. Y. Zeng, Z. Y. Wu, and D. K. Tung, "Experiments on temperature changes of microbolometer under blackbody radiation and predictions using thermal modeling by COMSOL multiphysics simulator," *Sensors (Switzerland)*, vol. 18, no. 8, 2018.

[58]   K. Demirel, E. Yazgan, S. Demir, and T. Akin, "A New Temperature-Tolerant RF MEMS Switch Structure Design and Fabrication for Ka-Band Applications," *J. Microelectromechanical Syst.*, vol. 25, no. 1, pp. 60–68, 2016.

[59]   N. Eroğlu, "Development of High Performance Active Materials for Microbolometers," Middle East Technical University.

[60]   K. R. Williams, K. Gupta, and M. Wasilik, "Etch rates for micromachining processing - Part II," *J. Microelectromechanical Syst.*, vol. 12, no. 6, 2003.

[61]   U. Buder, J. P. von Klitzing, and E. Obermeier, "Reactive ion etching for bulk structuring of polyimide," *Sensors Actuators, A Phys.*, 2006.

[62]   Y. Chen *et al.*, "Fabrication of polyimide sacrificial layers with inclined sidewalls based on reactive ion etching," *AIP Adv.*, 2014.

[63]   R. Cetın and O. Erturk, "Subwavelength perforated absorbers for infrared detectors," *Opt. Express*, vol. 28, no. 22/26, 2020.

[64]   E. Alpman, "Development of Low-Cost Uncooled Infrared Detector Arrays in Standard CMOS and SOI-CMOS Process," Middle East Technical Unicersity, 2005.

APPENDICES

A. PIXEL STRUCTURES
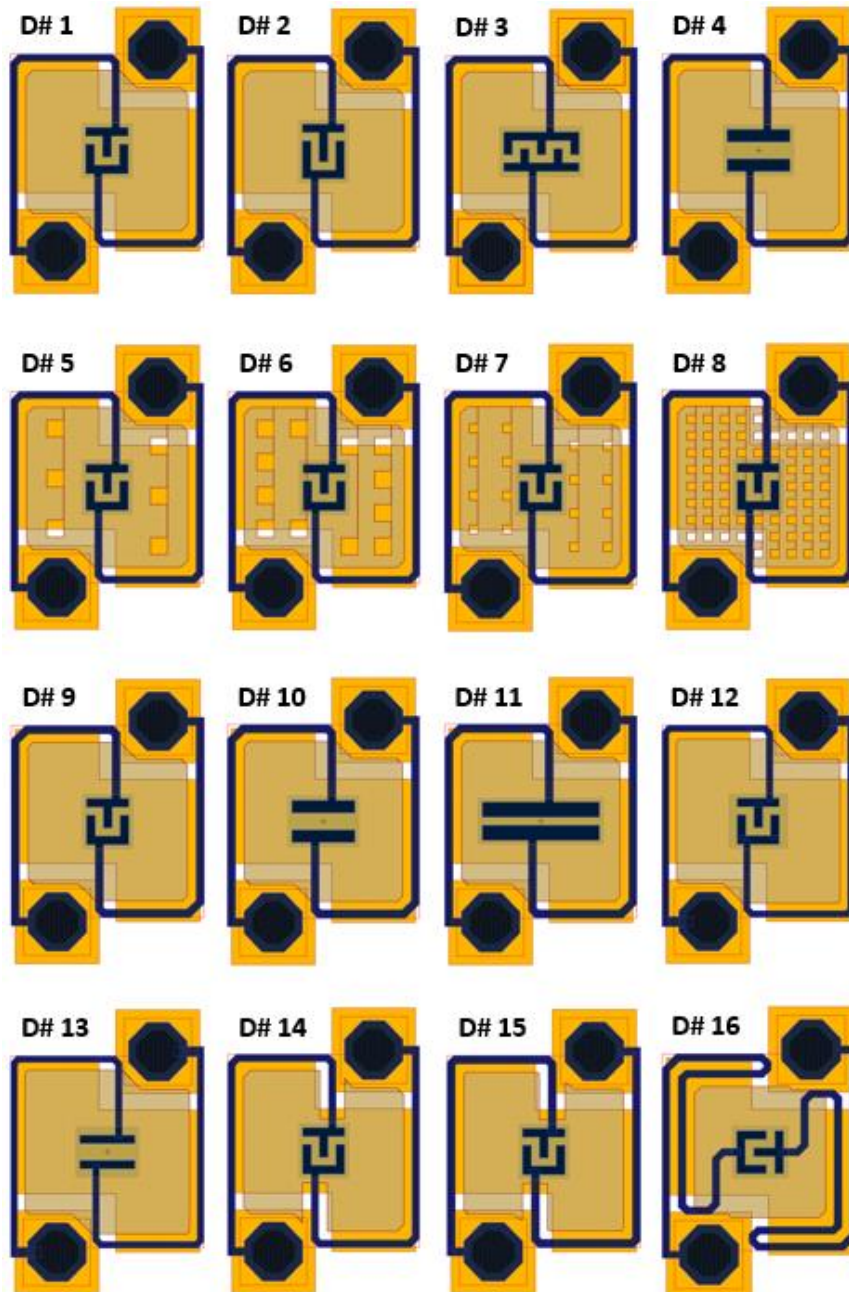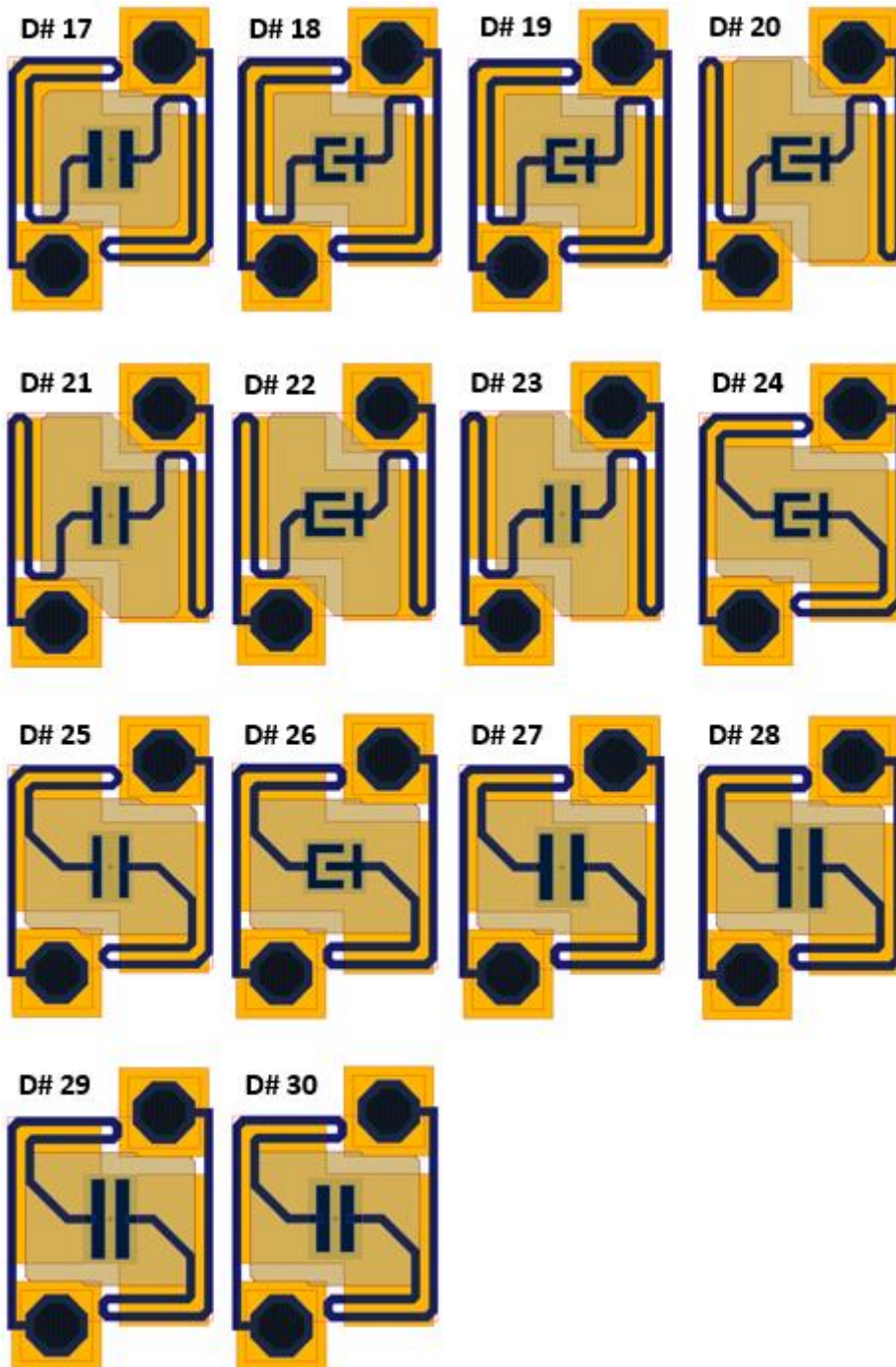
Simulated and microfabricated microbolometer pixel structures L-edit drawings. The pixels are shown from Design #1 to Design #30.

B. ELECTRODE DIFFERENCES COMPARISON

Resistance comparisons with different electrode structures that given geometries in **Table 2.4**.

Electrode v7 for test wafer #3 and #6

Electrode v8 for test wafer #3 and #6

Electrode v9 for test wafer #3 and #6

Electrode v10 for test wafer #3 and #6

Electrode v11 for test wafer #3 and #6

Electrode v12 for test wafer #3 and #6

Electrode v13 for test wafer #3 and #6